Analysis of an Energy Efficient Permanent Magnet Brushless Universal Motor

by
Mitchell Wing

Thesis Presented for the Degree of
DOCTOR OF PHILOSOPHY
in the Department of Electrical Engineering
University of Cape Town
February 1996

Declaration

This thesis is being submitted for the degree of Doctor of Philosophy in the Department of Electrical Engineering at the University of Cape Town. It has not been submitted before for any degree or examination at this or any other university. The author confirms that it is his own original work. Portions of the work have been published in condensed form in international journals and conference proceedings. The author confirms that in accordance with the University of Cape Town rule GP7(3) that he was the primary researcher in all instances where work described in this thesis was published under joint authorship.

Signed by candidate

M. Wing

12 February 1996.

Acknowledgments

My sincere thanks go to my supervisor, Prof. Jacek F. Gieras, for his advice and guidance throughout my research, and without whom this work would certainly not have been completed.

Many thanks to the Foundation of Research and Development (FRD) and Eskom Tertiary Education Support Program for their financial assistance to the project.

Abstract

The vast improvements made in the development of rare earth magnets, power electronics and micro-electronics over the last two decades can claim to be the major driving forces behind the rapid growth of permanent magnet (PM) brushless motor drives. The state of the art in PM motor technology is the PM universal motor, i.e. a combination of a PM synchronous and a PM brushless direct current (DC) motor. The PM universal motor has the capability to operate as a variable speed DC shunt motor with high torque at low speeds, and also as a synchronous motor at constant speed with high efficiency. The literature on synchronous and PM brushless motors is very extensive, although no studies have dealt with the concept of a PM brushless universal motor in any detail [87].

The objective of this thesis is to develop an energy efficient, high performance, reliable and inexpensive electrical motor to replace induction motors, in the 21^{st} century. Initial research of different AC motors highlighted the importance of correctly designing electrical motors. The different PM synchronous motors used in this study revealed that a sound knowledge of the motor's performance characteristics, at the design stage, is crucial to the successful and optimal design of any PM motor.

Since the dominant mode of operation of any universal motor is the constant speed region, the universal motor is designed around a PM synchronous motor. The accuracy of calculating the performance of PM synchronous motors depends on the accuracy of calculating the induced EMF and synchronous reactances. The analytical approach and finite element methods (FEMs) of calculating these parameters are well established in literature. It has, however, been found that the different methods have not been compared against each other. An extensive comparison of the different methods has been done and the results compared against experimental measurements. It was found that the flux linkage and loading methods of calculating the synchronous reactances and magnetising reactances, respectively, were sensitive to the magnitude of the armature current, and improvements were made to these methods. Improvements were also made to the method of doing experimental measurements using a curve fitting scheme. The study revealed that the analytical approach was not as reliable as the FEMs for all PM brushless motor designs. The flux linkage method coupled with the loading method proved to be the most appropriate method of calculating the synchronous parameters. The energy perturbation method was found to be more computationally intensive

than the flux linkage method and generally underestimated the results.

The use of the flux linkage and loading methods to calculate the leakage reactance has not been considered in any detail and has generally been overlooked. It was found that the direct axis and quadrature axis leakage reactances vary differently with increased load current. It is considered a more accurate estimate of the leakage reactances than the analytical approach since it includes the effects of saturation more accurately.

The universal motor was designed to be as reliable and robust as possible. The mode switching topology was thus designed to be very simple. The DC operating mode was designed around the monolithic brushless DC motor controller integrated circuit MC33035 from Motorola. It was found that this chip was an excellent solution to all the DC mode functions, including start-up and current limiting. The universal motor was built using a buried PM rotor.

The optimisation of any PM synchronous motor is extremely important due to the relatively high cost of PMs and the poor performance usually associated with a badly designed motor, where the rotor has not been designed to match the rest of the drive system. A survey of existing optimisation methods showed that there was a wide variation in methods for optimisation of PM electrical motors. Most of these methods were specific to a particular optimisation problem, used the FEM and were thus all computationally intensive. It was thus found that there is considerable scope for using a more general optimisation method which is reliable for all type of problems and there is scope for improving the computational effect of this optimisation routine. This study showed that the recently developed population based incremental learning (PBIL) optimisation algorithm was the most suitable and flexible optimisation routine. The study also showed that response surface methodology (RSM) can be successfully integrated into the PBIL for optimisation of PM synchronous motors. The use of RSM with the PBIL had not previously been explored and goes some way in indicating the possible future direction of optimisation in electrical machines.

This research has proved that the use of PM brushless universal motors is in fact a viable replacement for induction motors, in the near future.

Contents

List of Figures

List of Tables

List of Symbols and Abbreviations

Symbols	Units	
a		Number of current path pairs on the armature
$\vec{A}$	Wb/m	Magnetic vector potential
b_p	m	Pole shoe width
$\vec{B}$	T	Magnetic flux density
B_{ad}	T	Maximum value of the flux density of the d-axis reaction field
B_{ad1}	T	Amplitude of the fundamental harmonic of the d-axis reaction magnetic field
B_{aq}	T	Maximum value of the flux density of the q-axis reaction field
B_{aq1}	T	Amplitude of the fundamental harmonic of the q-axis reaction magnetic field
B_m	T	Magnetic flux density of the permanent magnet
B_{mg}	T	Maximum value of main magnetic flux density
B_{mg1}	T	Amplitude of first harmonic of main flux density
B_r	T	Remanent magnetic flux density of permanent magnet
B_u	T	Useful magnetic flux density in airgap
c_1		Number of coils per phase belt
D_{2out}	m	Outer diameter of rotor
D_{2in}	m	Inner diameter of rotor
D_{1out}	m	Outer diameter of stator yoke
D_{1in}	m	Inner diameter of stator
$\vec{E}$	V/m	Electric field intensity
e_o	V	Instantaneous induced electromotive force
E_o	V	Induced electromotive force of excitation field
E_i	V	Induced voltage in armature windings
f	Hz	Armature supply frequency
F_a	At	Armature magnetizing force
F_{aq}	At	Cross armature reaction magnetizing force
F_{ad}	At	Direct-axis armature reaction
F_{admax}	At	Maximum armature magnetizing force
F_{ak}	At	Commutation armature reaction
F_m	At	Total armature magnetizing force of magnet
F_p	At	Total armature magnetizing force per pole

Symbols	Units	
g	m	Airgap mechanical clearance between rotor and stator in d-axis
g_i		Non-linear inequality constraint
g_q	m	Airgap mechanical clearance between rotor and stator in q-axis
h_i		Equality constraint
h_m	m	Height of permanent magnet
h_s	m	Thickness of mild steel pole shoe
$\vec{H}$	A/m	Magnetic field intensity
H_a	A/m	Magnetic field intensity of armature reaction
H_{admax}	A/m	Maximum magnetic field intensity of armature reaction
H_c	A/m	Coercive force of permanent magnet
H_m	A/m	Magnetic field intensity of permanent magnet
i	A	Instantaneous armature current
I_1	A	Armature current
$I_2^{'}$	A	Rotor current referred to stator
I_d	A	d-axis armature current
I_q	A	q-axis armautre current
I_m	A	Magnitude of current
J	$kg\ m^2$	Moment of inertia of rotor and load inertia
$\vec{J}$	A/m^2	Current density
k_c		Carter's coefficient
k_f		Form factor of the excitation field
k_{fd}		d-axis form factor
k_{fq}		q-axis form factor
k_{sat}		Magnetic saturation factor
k_{w1}		Winding factor
l	m	Axial length of rotor
l_{end}	m	Length of end connection winding
l_i	m	Effective length of stator armature core
L	Ω	Inductance of the armature windings
L_d	Ω	Dynamic leakage inductance
L_e	Ω	Static leakage inductance
L_s	Ω	Slot leakage inductance
L_{sd}	Ω	d-axis inductance of the armature windings
L_{sq}	Ω	q-axis inductance of the armature windings
m_1		Number of phases
m_f		Frequency modulation ratio
$\vec{M}$	A/m^2	Magnetisation density
n_s	rev/s	Synchronous speed
N_1		Number of armature turns per phase
N_c		Number of conductors per slot
p		Number of pole pairs
P_{com}	W	Brush drop losses

Symbols	Units	
P_{cu}	W	Copper losses
P_1	W	Stator winding losses
P_2	W	Rotor winding losses
P_e	W	Electromagnetic power
P_{ext}	Wb/At	External leakage permeance of magnet
P_{fe}	W	Armature core losses
P_{fe2}	W	Rotor core losses
P_g	Wb/At	Permeance of airgap
P_{in}	W	Total input power
P_{lm}	Wb/At	Leakage permeance of magnet
P_m	Wb/At	Total permeance of magnet
P_{m0}	Wb/At	Internal permeance of magnet
P_{out}	W	Total output mechanical power
P_{rot}	W	Rotational losses
P_{str}	W	Stray losses
q_1		Number of slots per pole phase
R_1	Ω	Armature winding resistance
$R_2^{'}$	Ω	Rotor winding resistance referred to stator
R_g	At/Wb	Airgap reluctance
R_{lm}	At/Wb	Leakage reluctance of magnet
s		Split ratio in induction motor
s_1		Total number of armature slots
S_m	m^2	Cross sectional area of magnet
$\vec{T}$	Nm	Torque
$\vec{T}_e$	Nm	Electromagnetic torque
V	V	Terminal voltage
V_g	V	Magnetic voltage drop across airgap
V_m	m^3	Volume of permanent magnet
V_m	V	Magnetic voltage drop across magnet
V_{ry}	V	Magnetic voltage drop across rotor yoke
V_{st}	V	Magnetic voltage drop across stator teeth
V_{sy}	V	Magnetic voltage drop across stator yoke
w_m	m	Width of permanent magnet
w_μ	J	Energy of a magnetic field
W	J	Total stored magnetic energy
X_1	Ω	Stator winding reactance
$X_2^{'}$	Ω	Rotor winding reactance referred to stator
X_{ec}	Ω	End connection leakage reactance
X_l	Ω	Stator leakage reactance
X_{ls}	Ω	Slot leakage reactance
X_{ld}	Ω	Differential leakage reactance
X_{md}	Ω	d-axis magnetizing reactance

Symbols	Units	
X_{mq}	Ω	q-axis magnetizing reactance
X_{sd}	Ω	d-axis synchronous reactance
X_{sq}	Ω	q-axis synchronous reactance
X_{tt}	Ω	Tooth-top leakage reactance
α		Ratio of pole shoe width to pole pitch
α	rad	Mechnical radiants between the d-axis and a-phase
α_{sl}	rad	Slot pitch
δ	rad	Load angle
δ_i	rad	Inner torque angle
δb		Bias error
δl		Learning rate in PBIL
$\delta\epsilon$		Random error
ϵ	F/m	Electric permittivity
η		Efficiency
θ	rad	Internal power factor of armature current
λ_{ls}	H	Specific permeance of slot leakage
λ_{ld}	H	Specific permeance of differential leakage
λ_{tt}	H	Specific permeance of tooth-top leakage
μ	H/m	Magnetic permeability
μ_r		Relative magnetic permeability
σ	$1/(\Omega\ m)$	Conductivity
σ_l		Leakage factor
τ		Pole pitch
τ_1		Heyland's coefficient
τ_d	Wb	Differential leakage factor
ϕ	Wb	Magnitude of flux linkages
ϕ_m	Wb	Total flux linkage
Φ_g	Wb	Airgap magnetic flux per pole
Φ_l	Wb	Leakage magnetic flux per pole
Φ_{lm}	Wb	Leakage magnetic flux of permanent magnet
Φ_m	Wb	Fundamental harmonic rotor magnetic flux
Φ_r	Wb	Remanent magnetic flux of permanent magnet
Φ_t	Wb	Total magnetic flux per pole
χ		Magnetic susceptibility
ψ	rad	Power factor angle
ω_r	rad/s	Rotor rotational speed

Abbreviations

AC	Alternating current
DC	Direct current
EMF	Electromotive force
EPROM	Erasable programmable read-only memory
FE	Finite element
FEM	Finite element method
IGBT	Insulated gate bipolar transistor
MMF	Magnetomotive force
MVD	Magnetic voltage drop
PBA	Population based algorithm
PBIL	Population based incremental learning
PM	Permanent magnet
PVC	Polyvinyl chloride
RSM	Response surface methodology
SUB	Sealed universal block loadcell
TR	Torque per ampere ratio

Chapter 1

Introduction

1.1 Background

The use of permanent magnets (PM) for excitation of brushless motors has become an attractive option over the last two decades due to the vast improvements made in the development of rare earth permanent magnets that not only improve the motors' performance but also the motors' reliability. The price of these rare earth magnets is also dropping, notably Neodymium-iron boron (NdFeB), which is making these motors even more popular. The improvements made in power electronics and micro-electronics have meant that the control of brushless motors has become easier and more efficient, with the possibility of operating these motors over a large range of speeds and still maintaining a good efficiency.

Induction motors have been the most popular electric motor in the 20^{th} century. The main advantages of induction motors are their relatively low maintenance since they have no commutator or slip rings, low price, moderate reliability and that they are self-starting. The disadvantages are their small airgap which affects their reliability, lower efficiency than synchronous motors, cracking cage bars during reversals (large motors), and the impossibility of controlling their power factor without power electronic converters. These disadvantages coupled with the developments in brushless PM motor drives suggest the replacement of induction motors, in certain power ranges, with PM motors, such as PM synchronous or PM brushless direct current (DC) motors.

The universal motor is a combination of a PM synchronous (sinewave) and PM brushless DC (square-wave) motor. The universal motor combines the advantages of the brushless DC motor and synchronous motor into one motor drive. It has the capability to run as a variable speed DC motor with high torque at low speeds, and also operate as a synchronous motor at constant speed with high efficiency.

The present trend in the design of PM synchronous and PM brushless DC motors is towards the integration of the electronics with the motor. The future of the PM universal motor will follow the same trends towards an integrated motor, also called a smart motor. This

has particular relevance to Southern Africa where there is an definite need for highly reliable, robust and efficient motors that can be easily installed in rural areas. The universal motor can also operate off either single-phase or three-phase supply. Since many rural communities only have a single-phase supply the integrated design becomes an even more attractive option. The high efficiency of the universal motor is also important in the context of primitive reticulation systems.

PM motors, commutator and brushless types, are not manufactured in South Africa at all. The range of applications for these motors is increasing steadily and thus the demand for these motors is high. Since all PM motors are imported, the price of a small brushless permanent magnet motors is substantially more expensive than an equivalent induction motor of the same power rating. There is thus an increased need for a locally manufactured PM motor which can fill the gap in the South African market. These motors should be cheap to manufacture, use locally available equipment and have power ratings up to 30 kW. To achieve these goals it is necessary to develop the design tools to produce robust and reliable motors cheaply.

1.2 Objectives

The key objective of this thesis is to develop an energy efficient, high performance, reliable and inexpensive electrical motor to replace induction motors, in the 21^{st} century. The question of whether or not a PM universal motor can be economically manufactured has thus to be answered.

Further objectives include:

- Extensively comparing the analytical method and the finite element method (FEM) of calculating induced EMF and synchronous reactances with experimental measurements, to Identify the most appropriate method for use in the optimum design of PM synchronous motors.

- Improving the accuracy of the flux linkage method and loading method of calculating the synchronous reactance and magnetising reactance, respectively. These methods have been shown to be sensitive to the magnitude of the d-axis and q-axis armature current components.

- Developing a novel optimisation routine of PM synchronous motor design that is computationally fast and reliable, using a population based algorithm.

- Designing a working prototype universal motor that is cheap, robust and reliable. This universal motor should apply the general principle of switching automatically from synchronous to DC operating mode and vice versa.

1.3 Research context

After performing a series of tests on different AC motors, including an induction motor and a reluctance motor, it has been shown that the PM synchronous motors have the highest output power-to-mass ratio, the highest efficiency and the best dynamic performance. The switched reluctance motor used to be considered the motor with the highest power-to-mass ratio, but recent studies have shown the PM synchronous motor to have a higher ratio [24]. The performance comparison has also emphasised the importance of correctly designing PM synchronous motors. In Chapter 2 this series of performance tests on a number of small three-phase motors has been described.

The relatively high costs of rare earth PMs have limited the popularity of small and medium power brushless PM motors. It is thus imperative that the motor's performance can be modelled successfully so that the optimum design can be built. In the design of an universal motor the synchronous mode of operation is considered the dominant mode. The motor drive is thus designed for optimum performance in its synchronous mode.

The accuracy of calculating the steady-state performance of PM synchronous motors depends on the accuracy of calculating the induced EMF and synchronous reactances. A reliable method of calculating the induced EMF and synchronous reactances is thus needed. Chapter 4 considers this topic at great length. The methods generally used are the analytical approach and the FEM. The analytical approach uses circuital theory which is computationally fast whereas the FEM is very computationally intensive making it much slower. The method chosen to be used in the design of an optimum motor should be accurate for a large number of PM synchronous motor designs. The most accurate and reliable method has to be found by comparing the results with experimental measurements.

Owing to the difficulties in calculating the induced EMF and synchronous reactances using classical theory, form factors of the armature reaction have to be included. A set of equations describing the form factors for a number of different rotor shapes has been developed. These form factors are used to model the induced EMF and synchronous reactances for most PM synchronous rotor shapes.

The induced EMF and synchronous reactances have also been calculated using a two dimensional FEM. The methods of calculating the synchronous reactances, using the FEM, are the flux linkage and energy perturbation methods. No comparison between these two methods has been found in literature and thus an extensive comparison has been done including experimental results.

The flux linkage method of calculating the synchronous reactance and the loading method of calculating the magnetising reactance are both sensitive to the magnitude of the d-axis and q-axis components of the armature current. Both methods have been modified to remove these errors and improve their accuracy over the full operating range of the motor.

Experimental measurements have been used to determine the accuracy of the machine

parameter calculations. A method of determining the induced EMF and synchronous reactance, from experimental tests, using a curve fit scheme is proposed. This method is accurate and easy to use. An in-depth analysis of the methods of calculating the induced EMF and synchronous reactances is covered in Chapter 4.

A universal motor has been built using a buried PM rotor. The motor has position and speed feedback control for the DC operating mode. The position feedback loop control is also used in the synchronous mode to ensure that the motor changes to DC mode if the load torque becomes too large. The speed of the motor would then be reduced to cope with the increase in load torque in DC mode. If the load is reduced the motor increases speed and switches back into synchronous mode when synchronous speed is reached. The motor also starts up in DC mode and switches to synchronous mode, for constant speed operation, when synchronous speed is reached. Chapter 5 considers the practical aspects of designing a PM universal motor.

The optimisation of any PM synchronous motor is extremely important due to the high cost of PMs and the poor performance associated with a badly designed motor. The optimisation routine should be reliable and robust in finding the optimum design for a number of different rotor designs in the shortest possible time. This routine should also incorporate the best method of calculating the performance of synchronous machines. The optimisation routine uses a population based algorithm (PBA). Very little work in PM electric motor optimisation has been done using PBAs. This routine also incorporates a response surface technique to speed up the optimisation. The optimisation of the rotors of a surface PM rotor, surface PM rotor with mild steel pole shoes and a buried PM rotor using this population based algorithm are described in Chapter 6.

1.4 Literature review

Synchronous and PM brushless DC motors have been identified by many authors as motors that will play an important role in high specific output power and high efficiency applications of the future [14, 53]. The synchronous and PM brushless DC motors are often referred to as sinusoidal and trapezoidal machines, respectively [51]. This is due to the shape of the induced back EMFs created by these two motors. The terms synchronous and brushless DC will be used in this thesis since the same physical motor will be used for both motor types and only the shape of the input voltage to the stator windings will change.

PM synchronous motors are generally preferred over brushless DC motors due to their smoother torque production and higher efficiency. The larger amount of harmonic current in brushless DC motors not only results in higher losses but more noise and torque pulsations [37, 51]. The use of PM synchronous motors in variable speed applications requires the continuous measurement of the rotor's absolute angular position for self-synchronisation. This

type of control is identified as being complex and requires an extremely accurate rotor angular position sensor [51]. The PM brushless DC motors, however, have relatively simple control requirements for variable speed applications. The inverter topology used for both of these motors is identical, with the only difference being in the gate switching topology. This has lead to the decision to combine the advantages of both these motors into one universal motor. While the literature on synchronous and brushless PM motors is very rich, no publications to the knowledge of the author has dealt with research into PM brushless universal motors, although the idea is shown in [87].

The integration of the electronic controls, power electronics and motor into one unit has been considered an important development in the design of synchronous and PM brushless DC motors [51, 53, 71]. These integrated motor designs are generally called smart motors and the development of a smart universal motor is thus to be considered.

Synchronous machine models, for steady state performance analysis, are usually formulated using the well known two-axis theory developed at the beginning of the century by Blondel and others [34]. This theory transforms the (a,b,c) stator variables into direct (d) axis and quadrature (q) axis components for performance analysis of the synchronous motor.

Analytical methods of calculating the d-axis and q-axis synchronous reactances for cylindrical and salient pole synchronous machines are well known [101]. These methods are well established for wound-field excitation synchronous machines and have well defined form factors, for the field and armature reaction, used in modelling the non-sinusoidal induced fields in these models [58]. There has however been very little work done in establishing new form factors for PM rotors with complex geometries. The development of form factors for a set of different PM rotor shapes is thus needed to improve the accuracy of the analytical method.

The FEM has been used in the calculation of synchronous parameters, using the flux linkage method, since as early as 1971 [3, 26, 32, 43]. However, this initial work only included the saturation effects on the synchronous parameters to some degree. None of this work dealt with the mutual influence between the d-axis and q-axis magnetic fields on the operating performance and the saturated synchronous parameters, since the d-axis and q-axis reactances were calculated using separate FEMs. The magnetic field solution at one rotor position was also only considered and in some work the armature phase windings were modelled using sinusoidal current sheets [88]. The flux linkage method needs improving to take into account the effects of saturation at different load conditions, to account for the influence between the d-axis and q-axis and the variation in synchronous reactances with a change in rotor position.

The energy perturbation method is widely used in the calculation of self and mutual winding inductances [81]. These inductances can be transformed into the d-axis and q-axis reactances required for synchronous machine performance analysis. This method of calculating the synchronous reactances needs investigating and comparing against the flux linkage method for steady state performance analysis, as there are no comparisons of this nature

found in the literature to-date.

The calculation of the magnetising reactances has received a lot of attention in recent years with the development of the loading method [92]. In this method the variation of the induced EMF due to load changes is taken into account, as well as the mutual influence between the d-axis and q-axis magnetic fields. The accuracy of this method has, however, been shown to be dependent on the selection of the disturbance quantity in the armature current. A solution to this problem has recently been shown using a curve fitting scheme [93]. The disadvantage of this approach is that it is not convenient in problems where the motor is driven from a voltage source, since the d-axis and q-axis armature current components for a particular load angle cannot be easily calculated. The accuracy of the flux linkage method, when including the mutual influence between the d-axis and q-axis magnetic fields, is also sensitive to the disturbance in the armature current. The flux linkage and loading methods need developing to remove the dependence on this disturbance quantity.

Although the flux linkage, energy perturbation and loading methods are fairly well developed methods, the loading method has never been fully integrated into the flux linkage and energy perturbation methods for the full machine performance and the calculation of leakage reactances. A comparison of the flux linkage and energy perturbation methods is thus needed. There is also a need to compare these results against experimental measurements.

Classical experimental methods of determining the equivalent circuit parameters of wound-rotor synchronous machines [101] are not appropriate for PM synchronous machines, since the rotor magnetic field cannot be varied. The methods used for measuring the synchronous reactance parameters are the load test [85] and the static inductance tests, such as the standstill frequency response test [5, 29] and the DC decay test [70, 73, 112]. Over the last decade there has been a great deal of literature written about the static locked rotor inductance tests. This is mainly due to the problems associated with performing load tests on synchronous motors already installed in factories and on large synchronous machines. The same cannot be said about small PM synchronous motors. The simplifications made in the standstill frequency response test were made for analysing large synchronous machines and are therefore not appropriate for small synchronous machines. The DC decay test was also designed for large synchronous machines with the assumption that any error in matching the exterior resistance to the winding resistance is negligible. This is not true for small synchronous motors since the winding resistance is comparable with the leakage reactance. Other disadvantages of the DC decay method is that hysteresis effects, due to the pulsating current, produce a certain amount of scatter in the results and the method is sensitive to the thermal stability of the resistance balancing bridge [73]. A more direct method of experimentally measuring the synchronous reactances is thus required.

The problem with the load test method is that there is a lack of uniqueness in specifying induced EMF E_o and d-axis synchronous reactance X_{sd} [73], since the separation depends on

superposition in a non-linear model. The analysis of the load conditions of the motor cannot adopt the value of the open-circuit voltage since for different loads the armature reaction will change the saturation level of the magnetic flux and thus change the induced voltage E_o. A modified load test method has thus been used which relies on the assumption that E_o and X_{sd} are constant for a small disturbance in the armature current, thus linearising the problem in the neighbourhood of the particular operating point.

In the dynamic performance analysis of PM synchronous motors and PM brushless DC motors the two-axis method is not generally used. The methods are usually based on the *abc* frame of reference. The analysis of the complete motor drive transients is done. These models couple the electrical machine, power electronics and electronic control into one system. The field and circuit equations are also coupled to the mechanical motion through the electromagnetic torque [15, 30, 31]. The finite element (FE) models include rotor rotation, done using techniques such as the sliding surface method [111], the moving band method and the move advanced band interpolating technique [31]. This type of analysis is also used in steady state performance models where harmonics are being analysed [60] or for the analysis of brushless DC motors with square-wave commutation [15]. These models use state space time stepping and are extremely computationally intensive. It is thus not considered feasible to use time-stepping models in the analysis and optimisation of PM universal motors, where the dominant mode of operation is the steady state AC synchronous mode.

The optimisation of the PM universal motor design is crucial to the success and viability of the whole motor drive. Numerical field calculations for optimisation have become extremely popular over the last decade. Numerical field calculations require a relatively large amount of computational time. Further, the objective functions contain discretization errors and the derivatives of the objective functions can only be approximated by difference schemes [47].

Non-linear programming methods have been proposed that convert the constrained problem into an unconstrained vector-optimisation problem. These methods convert the problem using different variations of the penalty function and the augmented Lagrangian multiplier [64, 98, 99]. These methods are generally problem specific, but are relatively computationally efficient.

The use of artificial neural networks in non-iterative optimisation schemes have been successfully used by many authors [94]. These methods only work well if the data set of the performance pairs for training the network is close to the optimal solution.

The literature on stochastic methods of optimisation is very rich. This is due to the high probability of these methods finding global optimal [22] and their simplicity. Methods such as simulated annealing [107], genetic algorithm [113] and the evolution strategies [55] have been used in electrical motor design successfully. There is also literature on combined stochastic methods, such as the combined simulating annealing and genetic algorithm [96]. These stochastic methods generally require a large amount of computational time and have

optimisation control parameters which are problem specific. A recently proposed stochastic method, called the population based incremental learning (PBIL), abstracts away the control parameters used in other stochastic methods [6]. The PBIL is however still inherently a computationally intensive method, and thus the introduction of response surface methodology (RSM) into this method has helped relieve this problem.

Chapter 2

Comparative Analysis of Small Three-phase Sinewave Motors

A performance analysis of different three-phase AC sinewave motors was deemed necessary to determine the strengths of permanent magnet (PM) motors. Sinewave motors refer to electrical motors that operate directly from a AC sinewave supply whereas square-wave motors operate from a controlled DC 120^o square-wave input voltage. The PM motors are tested in synchronous operation. The small AC motors tested and compared are: (1) a cage induction, (2) a solid rotor induction, (3) a reluctance, (4) a synchronous with inset SmCo PMs on the rotor (5) a synchronous with surface mounted SmCo PMs on the rotor (6) a synchronous with surface mounted SmCo PMs on the rotor with mild steel pole shoes and (7) a synchronous with buried NdFeB PMs in the rotor.

As described in Chapter 1, cage induction motors are the most popular motors in power electronics and in this computer control era. Cage induction motors have lower efficiency than synchronous motors for low to medium power ratings. At present time, energy saving is very important and high-efficiency is crucial for electric motors used in large numbers. The energy conversion of the solid rotor induction motor is even worse than the cage induction motor. The starting currents are however reduced, and the rotor construction is simplified and thus cheaper. Other advantages include: (a) possibility of obtaining stable and linear torque-speed characteristics throughout the entire speed range; (b) high reliability; (c) high mechanical integrity, rigidity and durability; (d) low level of noise and vibrations (no slots). On the other hand, a solid-rotor induction motor has lower output power, efficiency and power factor, and higher no-load slip than a cage induction motor of the same size. The high impedance of the solid rotor is the main reason for these disadvantages.

Another option is a salient pole solid rotor without any excitation system, i.e. an AC reluctance motor. Certain reluctance motors can be manufactured cheaper than induction motors but, on the other hand it is very difficult to retain similar performance. Some researchers, e.g. [86] say that this motor can develop only half of the torque of an induction

motor of the same size. Of course, there are also different opinions in favour of reluctance motors, e.g. [63].

From the energy saving, performance and reliability point of view synchronous motors seem to be the best. There are opinions that they will be more popular than induction motors in the 21st century. The use of rare earth PMs in construction of electrical machines not only improves the efficiency, developed torque, and dynamic performance, but also the output power–to–mass ratio, motor construction, and reliability.

In an attempt to make the investigation as fair as possible to all the tested motors, a single commercial stator of an induction motor has been used with only the rotor construction changing.

2.1 Torque equations for AC motors

All the AC motors selected for analysis are typical, i.e. they have a laminated stator with a three-phase winding distributed in semi-open slots, the ratio stator core effective length–to–inner diameter is > 1, there are no sliding contacts on the rotor, and they are internal self-ventilated machines.

2.1.1 Cage induction motor

The input (stator) current of an induction motor as determined from the T-type equivalent circuit is:

$$I_1 = \frac{V - E_o}{R_1 + jX_1} \tag{2.1}$$

where V is the input voltage, E_o is the EMF induced in the stator winding, and $R_1 + jX_1$ is the stator winding impedance. The input voltage V is balanced by the stator EMF E_o which more or less fluctuates with the load.

Consequently, the electromagnetic torque developed is proportional to the input voltage squared, i.e.

$$T_e = \frac{P_e}{2\pi n_s} = \frac{m_1 E_o I_2' \cos\theta}{2\pi n_s}$$

$$T_e = \frac{m_1}{2\pi n_s} \frac{V^2 (R_2'/s)}{[R_1 + (R_2'/s)(1+\tau_1)]^2 + [X_1 + X_2'(1+\tau_1)]^2} \tag{2.2}$$

where m_1 is the number of stator phases, n_s is the synchronous speed, $R_2'/s + jX_2'$ is the rotor winding impedance referred to the stator system, s is the slip for the fundamental harmonic, $\tau_1 \approx X_1/X_g$ is Heyland's coefficient for the stator, X_g is the airgap (mutual) reactance, I_2' is the rotor current referred to the stator, and θ is the phase angle between E_o and I_2'.

An induction motor is a self-starting, speed-controllable motor. The full-load efficiency can be roughly estimated as $\eta \approx n/n_s$ (except for small machines). The losses in induction motors consists of the stator winding losses P_1, rotor winding losses P_2, stator core losses P_{fe}, rotor core losses P_{fe2} (significant only in inverter-fed motors), rotational losses P_{rot}, and stray losses P_{str}. The stray losses according to IEC standards are estimated as 0.5 % of the output power P_{out}.

2.1.2 Solid-rotor induction motors

Using the T-type equivalent circuit, the electromagnetic torque developed by an induction motor with a solid smooth homogeneous rotor can be found by replacing the rotor branch resistance R'_2/s referred to the stator by

$$\frac{R'_2(s)}{s} = a_R k_{tr} k_Z \frac{l_i}{\tau} \sqrt{\frac{\pi f \mu_o \mu_r}{\sigma}} \frac{1}{\sqrt{s}} \tag{2.3}$$

and by replacing the rotor leakage reactance X'_2 referred to the stator by

$$\frac{X'_2(s)}{s} = a_X k_{tr} k_Z \frac{l_i}{\tau} \sqrt{\frac{\pi f \mu_o \mu_r}{\sigma}} \frac{1}{\sqrt{s}} \tag{2.4}$$

where $a_R \approx 1.45$, $a_X \approx 0.85$ [45], $k_{tr} = 2m_1(N_1 k_{w1})^2/p$, N_1 is the number of stator turns per phase, k_{w1} is the stator winding factor for fundamental harmonic, p is the number of pole pairs, $k_Z \approx 1 + 0.5\tau/L_i$ is the transverse edge-effect coefficient ($k_Z > 1$), l_i is the effective length of stator stack, τ is the pole pitch, f is the motor input frequency, μ_o is the magnetic permeability of free space, μ_r is the relative magnetic permeability of the rotor, and σ is the electric conductivity of the solid rotor.

The stray losses P_{str} in a solid-rotor induction motor are higher than 0.5 % P_{out}. This is due to the rotor surface having a higher conductivity for eddy currents induced by the higher harmonic stator fields.

2.1.3 Synchronous motor

On the basis of the phasor diagram (Fig 3.1) and equivalent circuit, the armature current for a salient pole synchronous motor is:

$$I_1 = \sqrt{I_d^2 + I_q^2} \tag{2.5}$$

$$I_d = \frac{V(X_{sq}\cos\delta - R_1 \sin\delta) - E_o X_{sq}}{X_{sd}X_{sq} + R_1^2} \tag{2.6}$$

$$I_q = \frac{V(R_1\cos\delta + X_{sd}\sin\delta) - E_o R_1}{X_{sd}X_{sq} + R_1^2} \tag{2.7}$$

where V is the phase terminal voltage, E_o is the EMF per phase induced in the armature winding by the rotor excitation system (without armature reaction), δ is the power angle between V and E_o, R_1 is the armature winding resistance, X_{sd} is the d-axis synchronous reactance, and X_{sq} is the q-axis synchronous reactance.

The electromagnetic torque developed by a salient pole synchronous motor can be written in terms of the mutual reactance, as shown in Chapter 3, or in terms of the total synchronous reactances as:

$$\begin{aligned} T_e &= \frac{m_1}{2\pi n_s}\frac{1}{(X_{sd}X_{sq}+R_1^2)^2}[VE_o(R_1\cos\delta + X_{sd}\sin\delta)[(X_{sd}X_{sq}+R_1^2) \\ &\quad -X_{sq}(X_{sd}-X_{sq})] - VE_oR_1(X_{sq}\cos\delta - R_1\sin\delta)(X_{sd}-X_{sq}) \\ &\quad +V^2(R_1\cos\delta + X_{sd}\sin\delta)(X_{sq}\cos\delta - R_1\sin\delta)(X_{sd}-X_{sq}) \\ &\quad -E_o^2R_1[(X_{sd}X_{sq}+R_1^2) - X_{sq}(X_{sd}-X_{sq})]] \end{aligned} \tag{2.8}$$

Small synchronous motors have a rather high stator winding resistance R_1 that is commensurable with X_{sd} and X_{sq} which makes it necessary to retain R_1 in the torque equation.

The torque-angle characteristics is found by assigning arbitrary values to the power angle δ in the range of operation. The angle δ in eqn (2.8) is a measure of the load, as the slip s is in eqn (2.2) for induction motors.

2.1.4 Synchronous reluctance motor

The synchronous reluctance motor runs with an unexcited rotor having unequal reluctance in d and q axes. Since the rotor has no excitation system, the EMF $E_o = 0$ in eqns (2.6, 2.7, 2.8) and the developed torque is:

$$\begin{aligned} T_e &= \frac{m_1}{4\pi n_s}\frac{V^2(X_{sd}-X_{sq})}{(X_{sd}X_{sq}+R_1^2)^2}[(X_{sd}X_{sq}-R_1^2)\sin 2\delta \\ &\quad +R_1(X_{sd}+X_{sq})\cos 2\delta - R_1(X_{sd}-X_{sq})] \end{aligned} \tag{2.9}$$

The input current of a reluctance motor is higher than that of a synchronous and induction motor since the EMF induced in the stator winding is zero — eqns (2.6) and (2.7). Correspondingly, it affects the efficiency due to the high power loss dissipated in the stator winding. The developed torque of a reluctance motor can be increased by magnifying the synchronous reactances in d and q axes, i.e. the ratio X_{sd}/X_{sq} should be as high as possible. However, this in turn involves a heavier magnetising current resulting in a further increase in the input current due to a higher reluctance of the magnetic circuit in q-axis. A reluctance motor has, similarly to a PM synchronous motor, a good heat exchange since most of its losses are produced in the stator. The only losses in the rotor are core and stray losses.

Table 2.1: Design data of stator

Inner diameter of stator	0.08254 m
Outer diameter of stator	0.1365 m
Number of stator slots	36
Number of turns per coil	40
Number of parallel paths	1
Number of parallel wires	2
Cross section of stator conductor	0.5 mm
Coil span	full pitch
Number of winding layers	1
Number of pole pairs	2
Voltage rating (line-to-line)	380 V
Effective length of armature stack	0.103 m
b11	0.004768 m
b12	0.00305 m
b14 SLOT	0.00225 m
h11 DIMENSIONS	0.009895 m
h12 (Fig 2.1)	0
h13	0.000185 m
h14	0.00069 m

2.2 Construction of tested motors

The stator of a small 1.5-kW, 4-pole, 1410-rpm, 380-V, three-phase, Y-connected, cage induction motor manufactured by GEC (South Africa) has been selected for these tests.

The stator consists of a laminated core made of cold-rolled electrotechnical sheet-steel and a three-phase single-layer winding (Table 2.1). There are 36 semi-open slots, the number of turns per phase is $N_1 = 240$ and the coil span is equal to the coil pitch. The stator inner diameter is 82.54 mm and the effective length of the armature stack is 103 mm. According to the manufacturer, the full load torque for a commercial cage rotor is 10.2 Nm, the full load input current is 3.9 A, the full load efficiency is 75 %, and the full load power factor is 0.78. The same stator was used in testing the cage induction rotor, the solid induction rotor, the salient-pole solid rotor and the four PM rotors (Table 2.2).

A simple rotor design has been constructed using surface PMs. In the four-pole construction, three parallel 10 mm wide, 4 mm thick and 100 mm long SmCo PMs per pole magnetised radially, have been used. The first synchronous motor's rotor (PM1) has surface PMs embedded in slots (inset), the second rotor (PM2) has surface PMs without slots, and

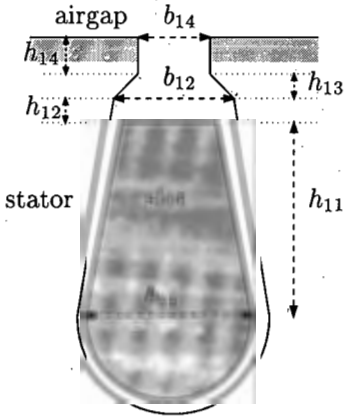

Figure 2.1: General shape of stator slot for small motors

Table 2.2: Rotors of tested motors

Quantity	Cage	Solid steel	Salient-pole solid steel (reluctance)	PM solid steel			
				PMs in slots (PM1)	Surface PMs (PM2)	Surface PMs with pole-shoes (PM3)	Buried PMs (PM4)
	1	**2**	**3**	**4**	**5**	**6**	**7**
Number of teeth (poles)	28	—	4	4	4	4	4
Diameter in d axis, mm	81.94	81.94	81.94	79.94	79.94	81.94	81.44
Diameter in q axis, mm	81.94	81.94	73.74	79.94	71.74	71.74	78.17
Width of pole, mm	—	—	26.5	37.7	39.6	39.96	55.76
Pole width to pole pitch	1.00	1.00	0.411	0.60	0.63	0.63	0.87

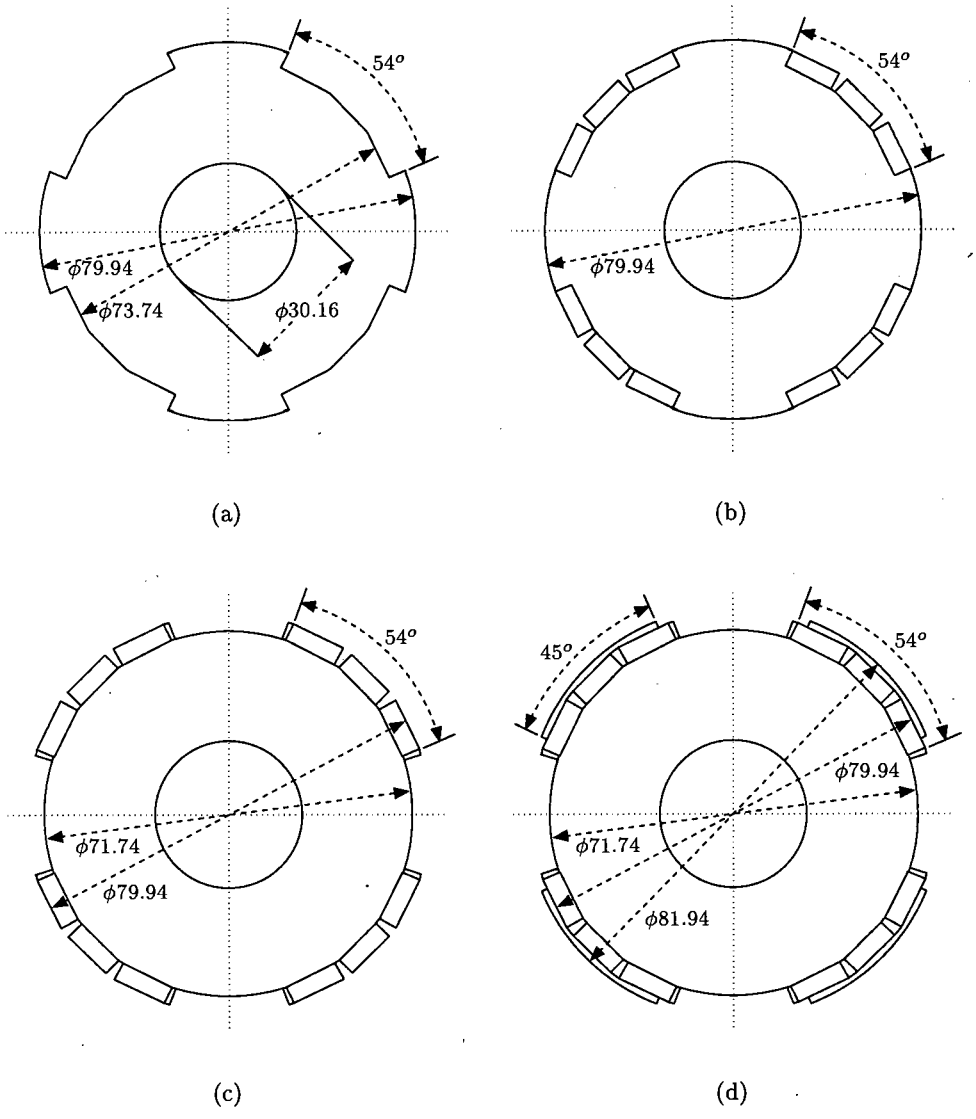

Figure 2.2: Synchronous motor rotors with: (a) solid salient poles (reluctance motor), (b) PMs embedded in slots (design PM1), (c) surface PMs (design PM2) and (d) surface PMs with pole shoes (design PM3).

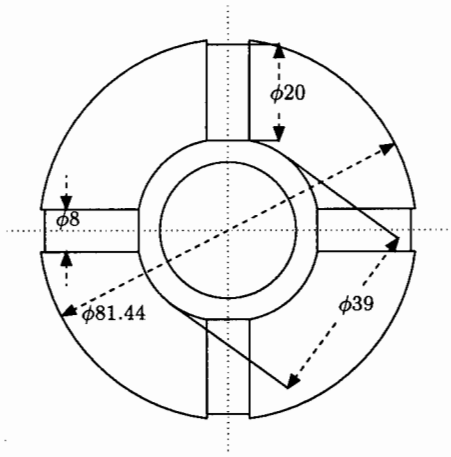

Figure 2.3: Synchronous motor rotor with buried PMs (design PM4)

the third rotor (PM3) has surface PMs with mild steel pole shoes covering 83% of the width of PMs, as shown in Fig 2.2.

A more complex rotor design, using buried PMs, has also been built. In this four pole construction, one 20 mm wide, 8 mm thick and 100 mm long NdFeB PM per pole magnetised tangentially, has been used. The rotor shown in Fig 2.3, has a brass sleeve which reduces leakage flux through the steel rotor shaft. The magnets are held in place with Loctite adhesive and the mild steel pole shoes are bolted onto the rotor shaft.

Photos of the cage rotor, reluctance rotor, surface PM rotor with mild steel pole shoes (PM3) and the buried PM rotor (PM4) are shown in Figs 2.4, 2.5, 2.6 and 2.7, respectively.

2.3 Experimental tests

Using a PC-based data acquisition system the steady-state characteristics of the designed motors have been tested under sinusoidal input voltage. All measurements have been done using the same test equipment. The test rig consists of the motor being tested coupled to an induction motor, used as an eddy current brake, mounted on rocker bearings. The test data is logged on a storage oscilloscope. The input voltage is measured using a high voltage probe, current using a hall effect device, speed using a disc and optical frequency counter and torque is measured using a torque transducer mounted on a lever arm from the induction motor casing.

The load tests require extremely high stator winding currents, which are well above the rated stator winding current density. The stator is rated for continuous operation as a PM synchronous motor at a maximum winding current density of 11 A/mm^2, while a winding current density up to 30 A/mm^2 was required in these load tests. The motor was thus only

Figure 2.4: Standard cage induction rotor supplied with motor

Figure 2.5: Reluctance rotor made from solid mild steel

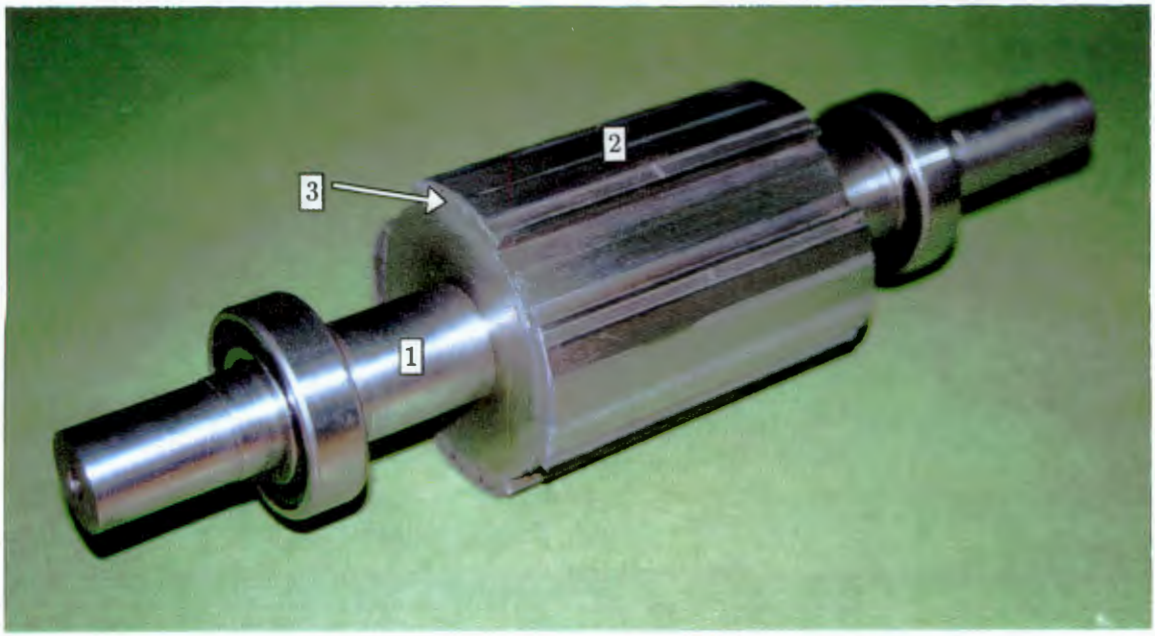

KEY:
1 – Solid steel shaft 3 – SmCo PMs
2 – Mild steel pole shoe

Figure 2.6: Surface PM rotor with mild steel pole shoes and shaft made from mild steel

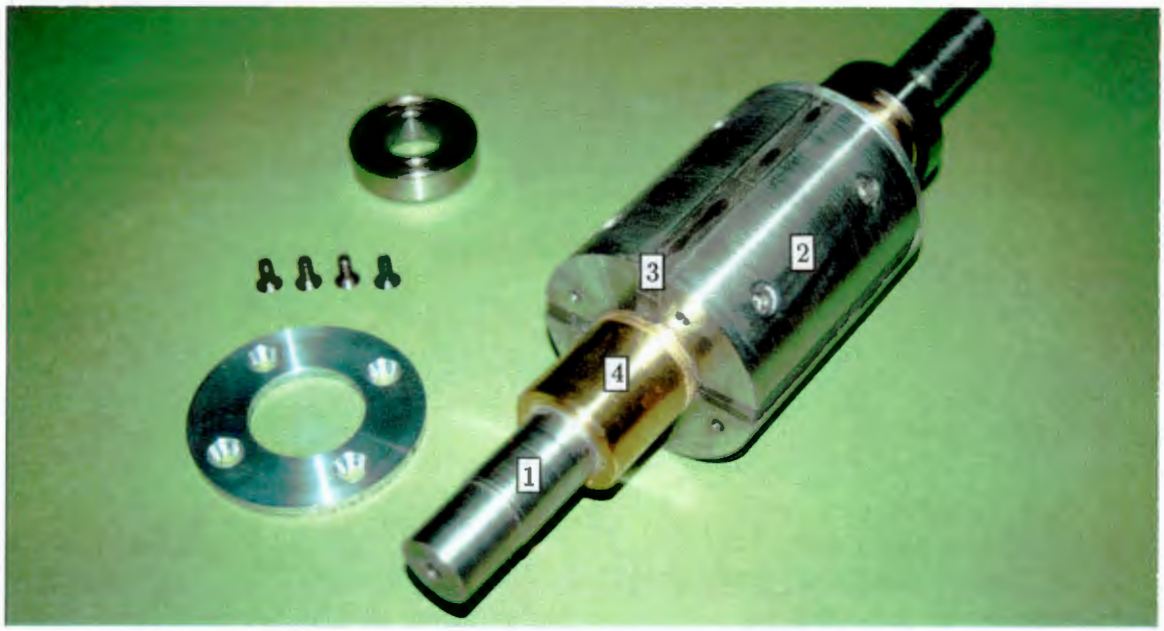

KEY:
1 – Solid steel shaft 3 – NdFeB PMs
2 – Mild steel pole 4 – Brass sleeve

Figure 2.7: Buried PM rotor partly disassembled to show PMs and brass sleeve

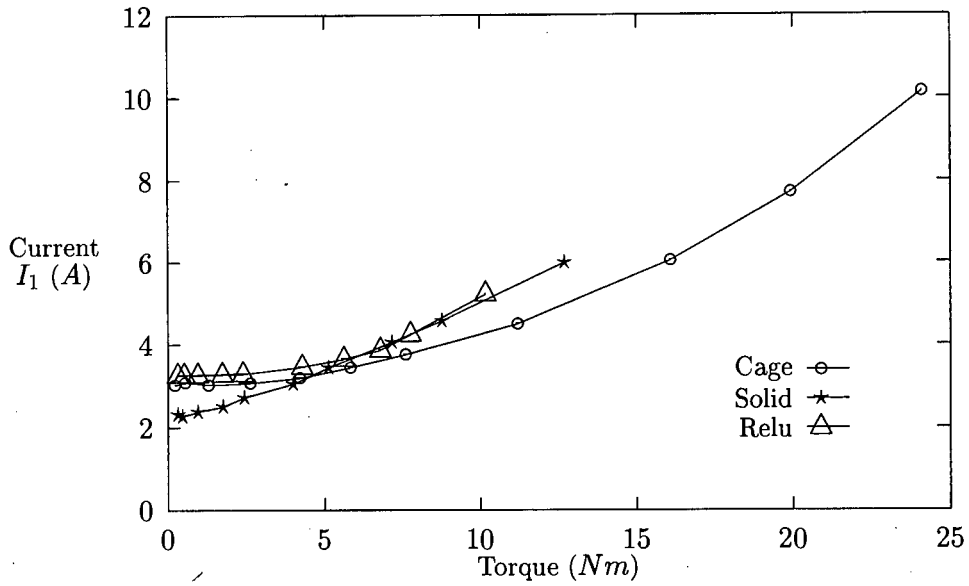

Figure 2.8: Comparison of the input currents for $f = 50$ Hz, $V_1 = 220$ V (phase), and sinusoidal input voltage.

operated at these high current levels for short periods of time, a few seconds, while the measurements were logged.

The input current, efficiency, power consumption and output shaft power versus shaft torque for all five motors are compared in Figs 2.8, 2.9, 2.10, 2.11, 2.12, 2.13, 2.14 and 2.14. The same value of sinusoidal input voltage $V_1 = 220$ V (phase) and constant frequency $f = 50$ Hz have been kept for all five motors. The reluctance motor has the lowest efficiency but draws lower current than the surface PM synchronous motors at $V_1 = 220$ V. Its current is only slightly higher than that of the cage induction motor. The buried PM motor PM4 draws the lowest current and shows the best efficiency.

The surface PM rotor PM1 has inset PMs and thus a high saliency. The high q-axis reactance, in comparison to PM2 and PM3, is the reason why this motor has the best efficiency of the three surface PM rotors. The high no-load current, in PM1, is due to the large airgap ($g = 1.3$ mm) which means a low induced EMF. The rotor PM2 has the same size airgap as PM1, thus a similar no-load current value. Rotor PM2 is, however, a surface PM rotor with almost no saliency and this relates to it having the worse efficiency of the three surface PM motors. The PM3 rotor has a decreased airgap ($g = 0.3$ mm) due to the mild steel pole shoe. This helps reduce the no-load current, but its maximum efficiency is still not as high as PM1 due to its lower saliency ratio.

The buried PM rotor PM4 has an airgap of $g = 0.55$ mm, but due to its flux concentrating design it has the lowest no-load current of all the PM motors. It also has a high saliency ratio

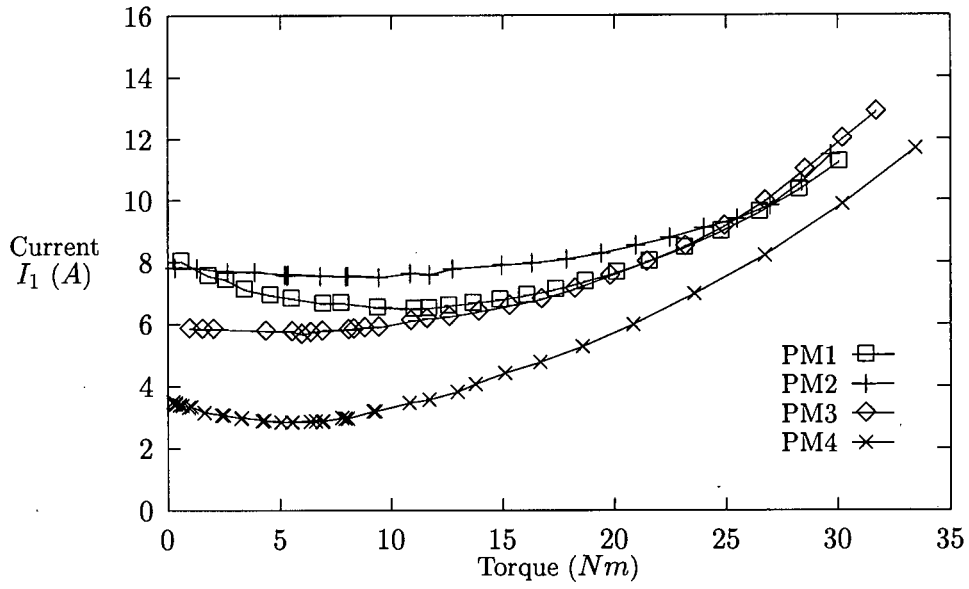

Figure 2.9: Comparison of the input currents for $f = 50$ Hz, $V_1 = 220$ V (phase), and sinusoidal input voltage.

Table 2.3: Open circuit EMF E_o for the synchronous motors (designs PM1, PM2, PM3 and PM4) running at 50 Hz.

	PM1	PM2	PM3	PM4
E_o (V)	109.7	120.0	147.1	162.5

making it the best of the PM rotor designs.

The performance of the PM synchronous motors improves with a decrease in the input voltage (a decrease in the input current and stator winding loss) as shown in Figs 2.16 and 2.17. There is an optimal voltage at which the motor achieves the best efficiency for a given load [103]. This is based on the open circuit EMF E_o. If E_o is too low in relation to the terminal voltage V_1 then a large no-load current is expected and thus low efficiency. Table 2.3 shows the value of E_o for the four different permanent magnet synchronous motors, at 50 Hz. At $V_1 = 180$ V (phase), the maximum efficiency of the PM synchronous motor PM2 is about 80% ($T = 9$ Nm), PM3 is about 88% ($T = 7$ Nm) and PM4 is about 90% ($T = 6$ Nm) as compared with 68% ($T = 22$Nm), 70% ($T = 18$Nm) and 89% ($T = 14$ Nm), respectively, at 220 V. The maximum efficiency of the cage induction motor, according to tests, was 73% at 220 V. This confirms that either the stator winding does not match the PM synchronous motors or the permanent magnet rotors needed designing specifically for this stator, stator windings and voltage rating.

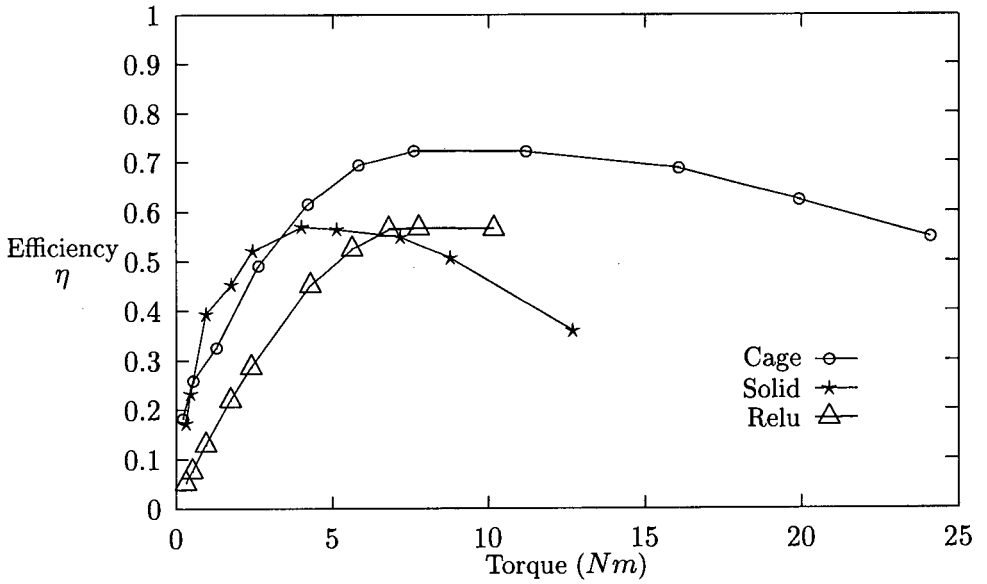

Figure 2.10: Comparison of efficiencies for $f = 50$ Hz, $V_1 = 220$ V (phase), and sinusoidal input voltage.

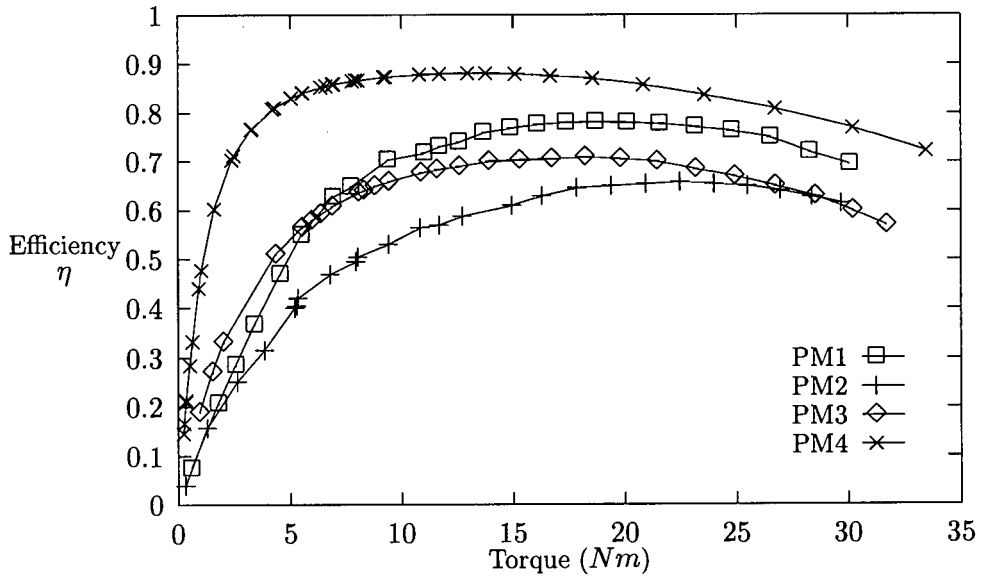

Figure 2.11: Comparison of efficiencies for $f = 50$ Hz, $V_1 = 220$ V (phase), and sinusoidal input voltage.

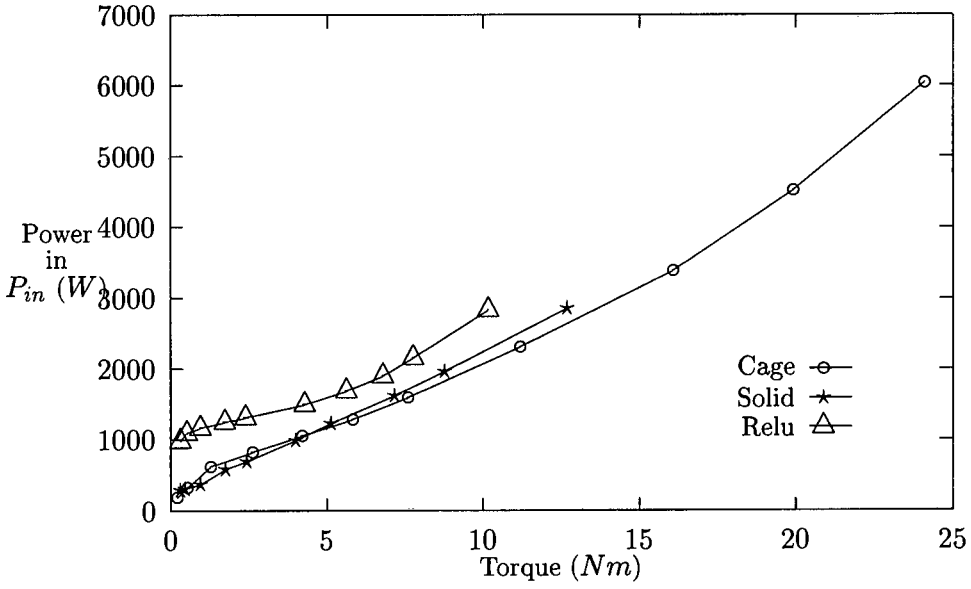

Figure 2.12: Comparison of energy consumption for $f = 50$ Hz, $V_1 = 220$ V (phase), and sinusoidal input voltage.

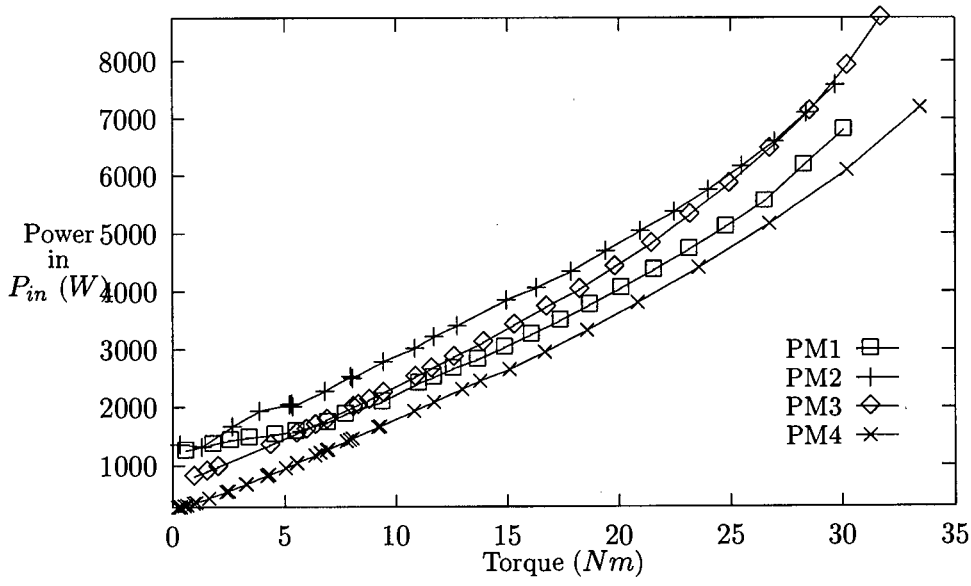

Figure 2.13: Comparison of energy consumption for $f = 50$ Hz, $V_1 = 220$ V (phase), and sinusoidal input voltage.

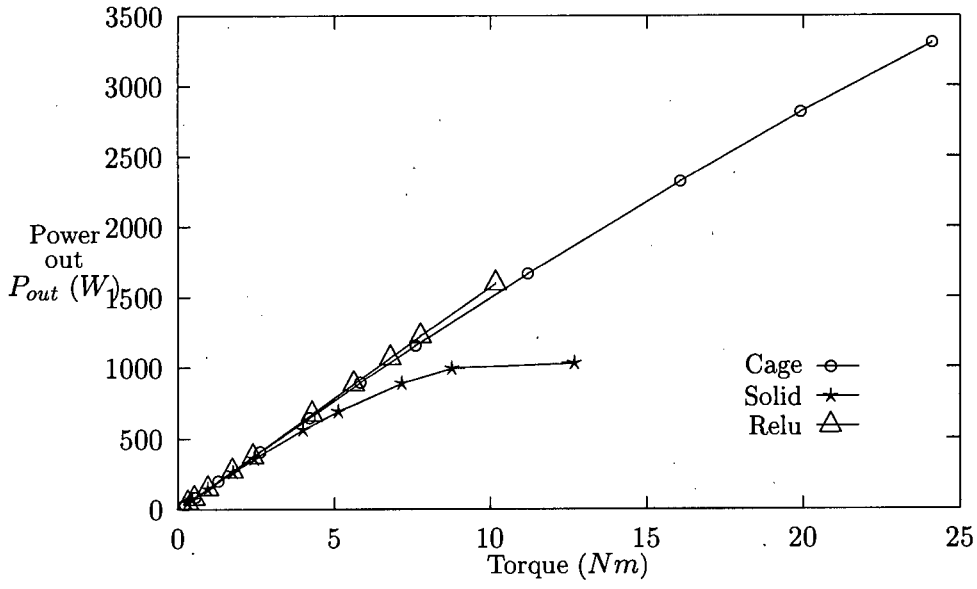

Figure 2.14: Comparison of output (shaft) power for $f = 50$ Hz, $V_1 = 220$ V (phase), and sinusoidal input voltage.

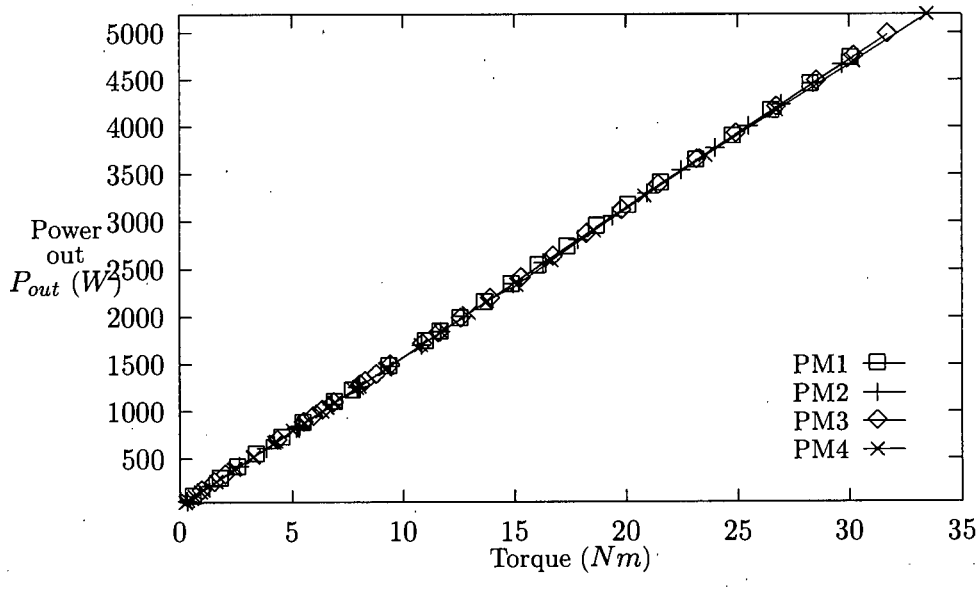

Figure 2.15: Comparison of output (shaft) power for $f = 50$ Hz, $V_1 = 220$ V (phase), and sinusoidal input voltage.

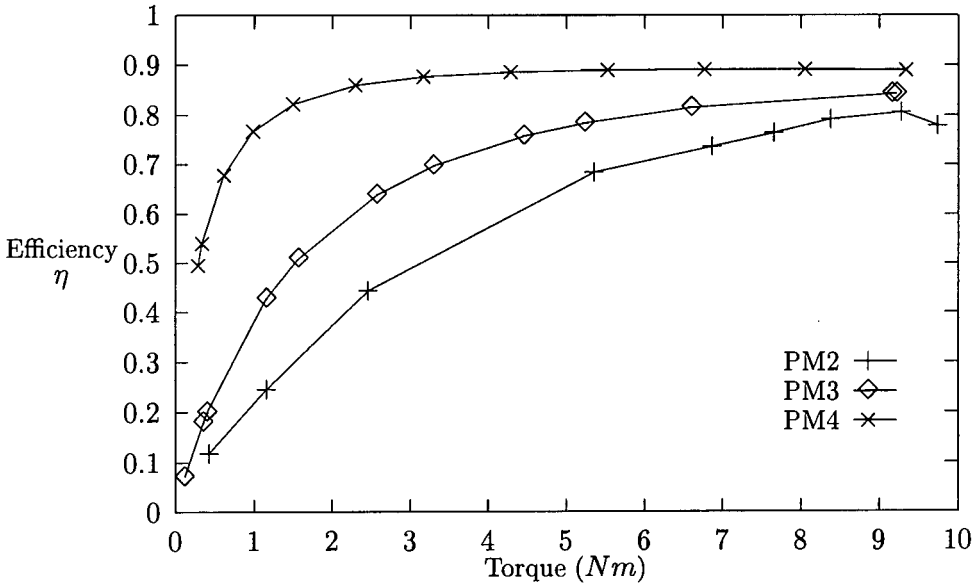

Figure 2.16: Efficiency at 50 Hz and $V_1 = 180$ V (phase) for the synchronous motors with surface PMs (design PM2 and PM3) and buried PMs (PM4).

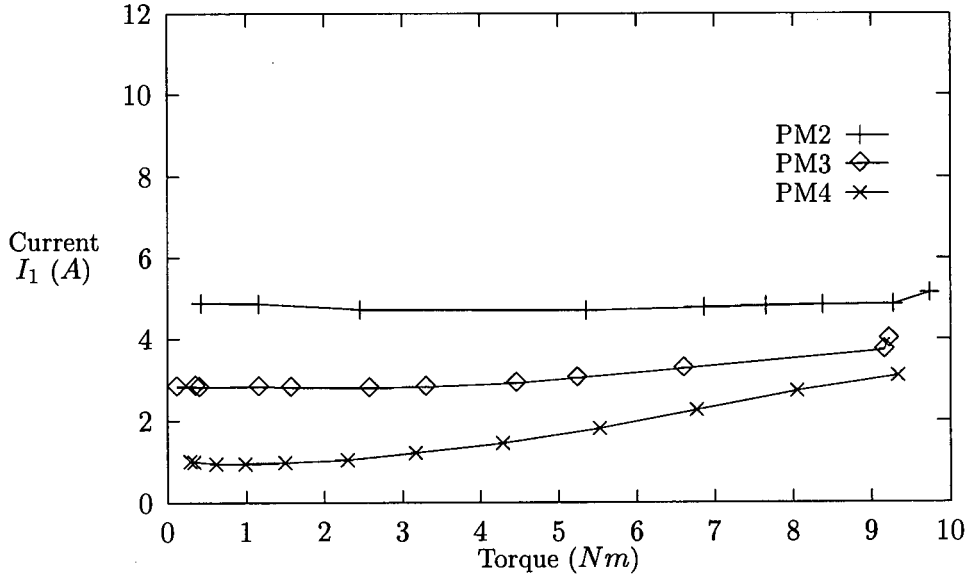

Figure 2.17: Input current at 50 Hz and $V_1 = 180$ V (phase) for the synchronous motors with surface PMs (design PM2 and PM3) and buried PMs (PM4).

Chapter 3

Fundamentals of Permanent Magnet Synchronous Motor Theory

The classical and FE theory of PM synchronous motors are well known. This brief summary of fundamental theory is necessary for the understanding of later Chapters.

3.1 Analytical Approach

PM synchronous motors, also called *sinewave brushless PM motors*, have multi-phase stator windings with distributed parameters which produce sinusoidal or quasi-sinusoidal distribution of the MMF. PM synchronous motors operate on the principle of a rotating magnetic field.

For a sinusoidal distribution of the airgap magnetic flux density the first harmonic of the excitation flux can be found as:

$$\Phi_{m1} = l_i \int_0^{\tau} B_{mg1} \sin \frac{\pi}{\tau} x dx = \frac{2}{\pi} l_i \tau B_{mg1} = \alpha B_{mg1} l_i \tau \tag{3.1}$$

where l_i is the effective length of the armature core, B_{mg1} is the peak value of the first harmonic of the magnetic flux density and $\alpha = 2/\pi$. The field excitation magnetic flux calculated on the basis of the maximum airgap magnetic flux density B_{mg} is then

$$\Phi_m = \Phi_{m1} = \alpha l_i \tau k_f B_{mg} \tag{3.2}$$

where k_f is the form factor of the excitation field [58]. B_{mg} is obtained using the magnetic circuit of the motor and the operating point on the demagnetisation curve of the permanent magnets [13, 46, 65, 74, 80]. The induced EMF is then:

$$E_o = \pi \sqrt{2} N_1 k_{w1} f \Phi_m \tag{3.3}$$

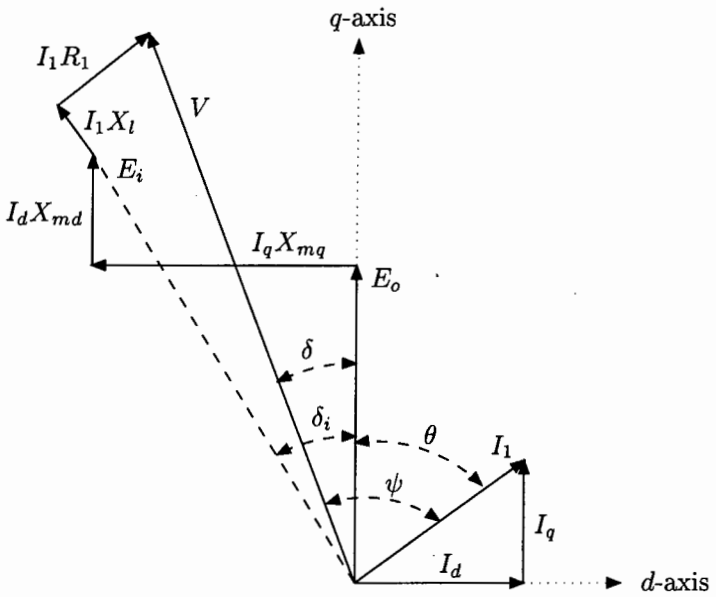

Figure 3.1: Phasor Diagram for underexcited salient pole PM synchronous motor

where k_{w1} is the winding factor.

The load angle or power angle δ of a synchronous machine is usually defined as the angle between the input phase voltage V and the EMF E_o induced in a single stator (armature) winding by the rotor magnetic excitation flux Φ_m. The phasor diagram shown in Fig 3.1 has been drawn using a consumer arrow system and it corresponds to the following Kirchhoff's voltage equation in phasor terms:

$$\vec{V} = \vec{E}_o + R_1\vec{I}_1 + j\omega L_{sd}\vec{I}_d + j\omega L_q\vec{I}_q \tag{3.4}$$

where $\vec{V}$ is the input voltage, $\vec{I}_1$ is the armature (stator) current, $\vec{I}_d$ is the d-axis armature current, $\vec{I}_q$ is the q-axis armature current, R_1 is the armature winding resistance per phase, $X_{sd} = j\omega L_{sd}$ is the d-axis synchronous reactance, and $X_{sq} = j\omega L_{sq}$ is the q-axis synchronous reactance.

The synchronous reactances X_{sd} and X_{sq} can be broken-up into:

$$X_{sd} = X_{md} + X_l \tag{3.5}$$

and

$$X_{sq} = X_{mq} + X_l \tag{3.6}$$

where X_{md} and X_{mq} are the d-axis and q-axis magnetising reactances respectively and X_l is the leakage reactance.

From the phasor diagram shown in Fig 3.1 the electrical power developed in the airgap is:

$$\begin{aligned} P_e &= m_1 E_i I_1 \cos(\delta_i) \\ &= m_1[I_q E_o + I_d I_q (X_{md} - X_{mq})] \end{aligned} \tag{3.7}$$

where m_1 is the number of stator phases and δ_i is the interior load angle. The electromagnetic torque developed by the motor is then:

$$\begin{aligned} T_e &= \frac{pP_e}{2\pi f} \\ &= \frac{pm_1}{2\pi f}[I_q E_o + I_d I_q (X_{md} - X_{mq})] \end{aligned} \tag{3.8}$$

where p is the number of pole pairs.

Fig 3.2 shows the complete computation of the performance of a PM synchronous motor for a full range of load angles. Due to the non-linearity in the simulation of a particular operating point, an iterative procedure has been used that starts off by estimating the value of the useful magnetic flux density and then obtains a better estimate from the magnetic circuit analysis. The iterative loop is exited once the error in the estimation of the magnetic flux density is small enough.

The synchronous reactances and induced EMF are the most important variables used in the design of PM synchronous machines. The developed power and torque are both proportional to the difference in the d-axis and q-axis reactances, and to the induced EMF. The induced EMF is related closely to the operating point of the PM which in turn is influenced by the machine's magnetic circuit and armature reaction.

3.1.1 Synchronous Reactances

The d-axis and q-axis synchronous reactances are defined as:

$$X_{sd} = X_{md} + X_l \tag{3.9}$$

$$X_{sq} = X_{mq} + X_l \tag{3.10}$$

The d-axis and q-axis unsaturated magnetising reactances are, respectively [58]:

$$X_{md} = 2m_1 \mu_o f \frac{(N_1 k_{w1})^2 D_{2out} l}{p^2 k_c g} k_{fd} \tag{3.11}$$

$$X_{mq} = 2m_1 \mu_o f \frac{(N_1 k_{w1})^2 D_{2out} l}{p^2 k_c g} k_{fq} \tag{3.12}$$

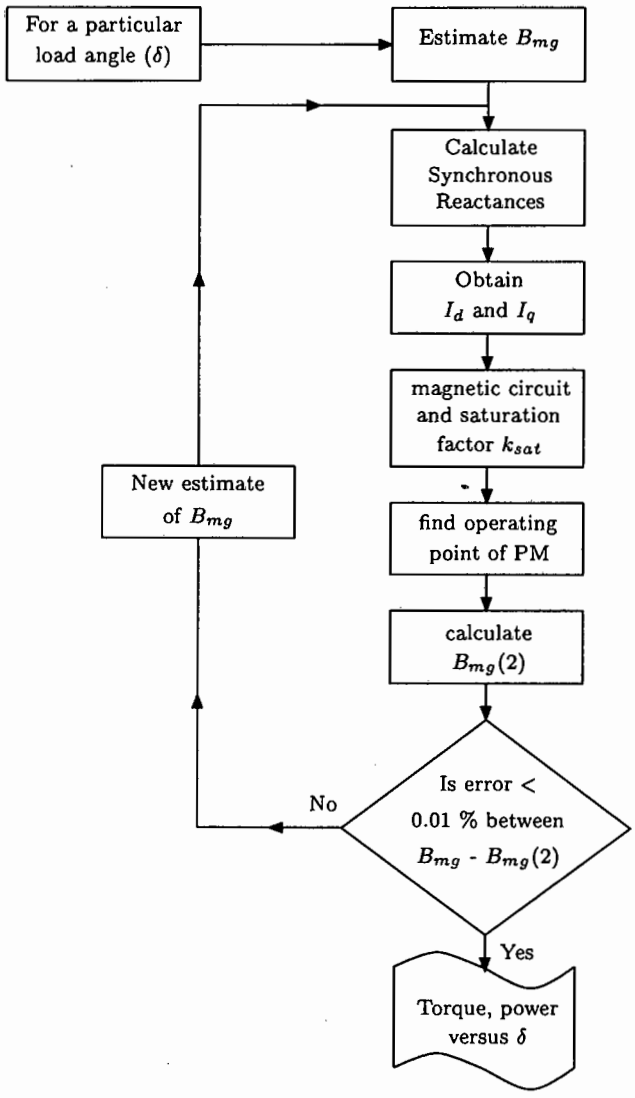

Figure 3.2: Block diagram of performance analysis of brushless permanent magnet synchronous motors using analytical approach

where m_1 is the number of phases, f is the stator input frequency, N_1 is the number of stator windings per phase, k_{w1} is the winding factor, D_{2out} is the rotor outer diameter, l is the rotor axial length, p is the number of pole pairs, k_c is Carter's coefficient, g is the airgap length, and k_{fd} and k_{fq} are the d-axis and q-axis form factors respectively. In salient-pole synchronous machines with electromagnetic excitation the d-axis magnetising reactance, eqn (3.11), depends on the saturation of the magnetic circuit. The saturation can be included using the saturation factor of the magnetic circuit k_{sat} i.e. the equivalent airgap in d-axis is $k_c k_{sat} g$. In certain PM machines the saturation of the magnetic circuit affects both X_{md} and X_{mq}.

The stator leakage reactance X_l consists of the slot leakage, differential leakage, tooth-top leakage and end connection leakage [2, 56, 58]. The different components of the leakage reactance can be calculated as :

(a) **Slot leakage inductance (X_{ls})** is usually derived by assuming the flux goes straight across the slots, thus assuming that the ferromagnetic material around the slot has infinite permeability [2]. It is also possible to derive analytical equations assuming a finite permeability of the teeth. The magnetic saturation due to the leakage fields can be taken into account using e.g. Norman's coefficients [83].

(b) **Differential leakage (X_{ld})** is a fictitious reactance which takes into account the space field harmonics greater than one [58].

(c) **Tooth-top leakage (X_{tt})** comprise the leakage that goes through the airgap from tooth-top to tooth-top. The principle of superposition can be used in calculating X_{tt} [56].

(d) **End connection leakage (X_{ec})** is calculated treating the end winding leakage as a revolving field in air. The stator ferromagnetic core is usually neglected in the derivation. The effects of adjacent coils and adjacent phases on each other are usually ignored too. Due to the great difficulty in calculating the end connection leakage, formulas are partly theoretically derived and partly from experimental tests [58]. Single-layer or double-layer winding configurations are included using empirical coefficients.

Thus the stator winding leakage reactance is:

$$X_l = X_{ls} + X_{ld} + X_{tt} + X_{ec} \tag{3.13}$$

which can be written in terms of the specific permeances as:

$$X_l = 4\mu_o \pi f \frac{N_1^2 l}{p q_1} (\lambda_{ls} + \lambda_{ld} + \lambda_{tt} + q_1 \lambda_{ec} \frac{l_{end}}{l}) \tag{3.14}$$

Table 3.1: Specific permeances for different parts of stator leakage reactance for a semi-oval slot with a single-layer winding

Slot	$\lambda_{ls} = 0.1424 + \frac{2h_{11}}{3(b_{11}+b_{12})} + \frac{h_{12}}{b_{12}} + \frac{2h_{13}}{b_{12}+b_{14}} + \frac{h_{14}}{b_{14}}$
Differential	$\lambda_{ld} = \frac{m_1 q_1 \tau k_{w1}^2}{\pi^2 k_c k_{satg}} \tau_d$ where $\tau_d = \frac{1}{k_{w1}^2} \sum_{\nu>1} \frac{k_{w1\nu}^2}{\nu^2}$
Tooth-top	$\lambda_{tt} = \frac{5\frac{g}{b_{14}}}{5+4\frac{g}{b_{14}}}$
End connection	$\lambda_{ec} = 0.47 - 0.3\frac{\tau}{l_{end}}$

where l_{end} is the length of the end connection armature winding and $q_1 = s_1/(2pm_1)$ is the number of slots per pole per phase.

The specific permeances λ_{ls}, λ_{ld}, λ_{tt} and λ_{ec} are given in Table 3.1, for a semi-closed oval slot with a single layer winding as shown in Fig 2.1. The tooth-top leakage and end-connection leakage reactances are saturation independent.

3.1.2 EMF

The fundamental harmonic EMF per phase in the stator winding induced by the rotor magnetic flux density, at no-load, is defined as:

$$E_o = \sqrt{2}\pi k_{w1} N_1 \Phi_m f \tag{3.15}$$

where Φ_m is the fundamental harmonic rotor magnetic flux, which is:

$$\Phi_m = \alpha \tau l B_{mg1} \tag{3.16}$$

where $\alpha = b_p/\tau$ is the ratio of the pole shoe width b_p to the pole pitch τ and B_{mg1} is the first harmonic airgap magnetic flux density, which can be written as:

$$B_{mg1} = k_f B_{mg} \tag{3.17}$$

where k_f is the main field (excitation field) form factor and B_{mg} is the maximum flux density of the main field produced by the PMs. B_{mg} is calculated with the uses of the demagnetisation curve of the PM, as described below. The form factor of the excitation field is used to find the peak value B_{mg1} of the first harmonic of the airgap magnetic flux density distribution.

Eqn (3.15) including eqn (3.16) can be written as:

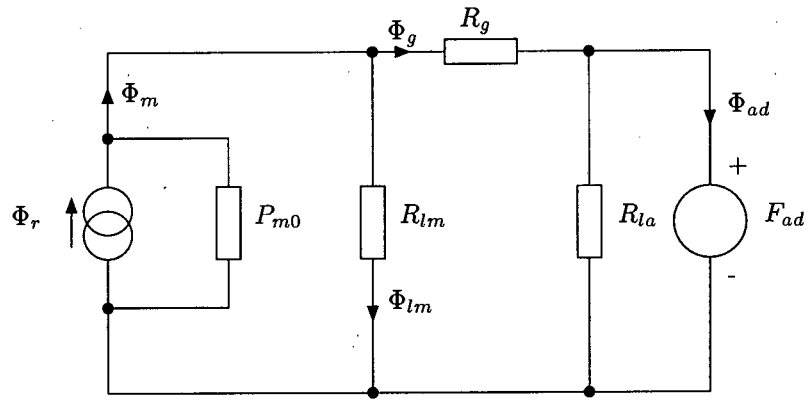

Figure 3.3: Magnetic equivalent circuit of a pole of a PM synchronous machine

$$E_o = \sqrt{2}\pi k_{w1} N_1 f \alpha \tau l B_{mg} k_f \tag{3.18}$$

The form factor, k_f, will be discussed in more detail in Chapter 4.

3.1.3 Magnetic equivalent circuit

The operating conditions of a PM are determined by the external magnetic circuit of the machine, and its performance is determined by this circuit and whether the PM was magnetised before or after installation.

A simplified equivalent magnetic circuit of one pole of a PM synchronous machine is shown in Fig 3.3. The PM is modelled as a flux source Φ_r with an internal permeance P_{m0}. The leakage flux has a reluctance R_{lm} in parallel with the PM flux source. The airgap reluctance R_g is in series with the d-axis armature MMF F_{ad}.

The reluctances of the stator teeth, stator yoke and rotor yoke are assumed to be zero i.e. infinite permeance. The airgap reluctance R_g has a saturation factor introduced to compensate for the reluctances of these ferromagnetic materials. The calculation of this saturation factor will be calculated using a non-linear magnetic circuit and will be discussed in the section on non-linear circuits.

The following relationships can be defined from the magnetic equivalent circuit:

$$\Phi_m = B_m S_m = \Phi_{lm} + \Phi_g \tag{3.19}$$

$$\Phi_m = \Phi_r + P_{m0} F_m \tag{3.20}$$

$$P_m = P_{lm} + P_g \tag{3.21}$$

$$F_c = H_c h_m \tag{3.22}$$

$$F_m = H_m h_m = F_c + \frac{\Phi_m}{P_{m0}} \tag{3.23}$$

$$F_m = H_m h_m = -\frac{\Phi_{lm}}{P_{lm}} \tag{3.24}$$

$$F_m = H_m h_m = -\frac{\Phi_g}{P_g} + F_{ad} \tag{3.25}$$

where h_m is the height of the PM, S_m is the cross sectional area of the PM, B_m and H_m are the magnetic flux density and magnetic field intensity of the PM, Φ_m is the total flux of the PM, F_m is the total MMF of the PM, P_m is the total permeance of PM, P_g is the airgap permeance, F_c is the MMF corresponding to H_c and P_{lm} is the leakage permeance of PM.

The total magnetic flux density can then be written, using the above equations, as:

$$B_m = \frac{\Phi_m}{S_m} = -P_m \frac{h_m}{S_m}(H_m - \frac{H_{ad}}{\sigma_l}) \tag{3.26}$$

which represents a line with slope

$$\tan \alpha_t = P_m \frac{h_m}{S_m} \tag{3.27}$$

and where $H_{ad} = F_{ad}/h_m$ and σ_l is the leakage factor

$$\sigma_l = \frac{P_m}{P_g} = 1 + \frac{P_{lm}}{P_g} \tag{3.28}$$

Similarly, the useful magnetic flux density can be written as:

$$B_u = \frac{\Phi_g}{S_m} = -P_g \frac{h_m}{S_m}(H_m - H_{ad}) \tag{3.29}$$

where

$$\tan \alpha = P_g \frac{h_m}{S_m} \tag{3.30}$$

3.1.4 Operating point of PMs

The demagnetisation curve of hard ferromagnetic materials can be modelled using the equation of hyperbola as [46]:

$$B = \frac{B_r(H_c - H)}{H_c - aH} \tag{3.31}$$

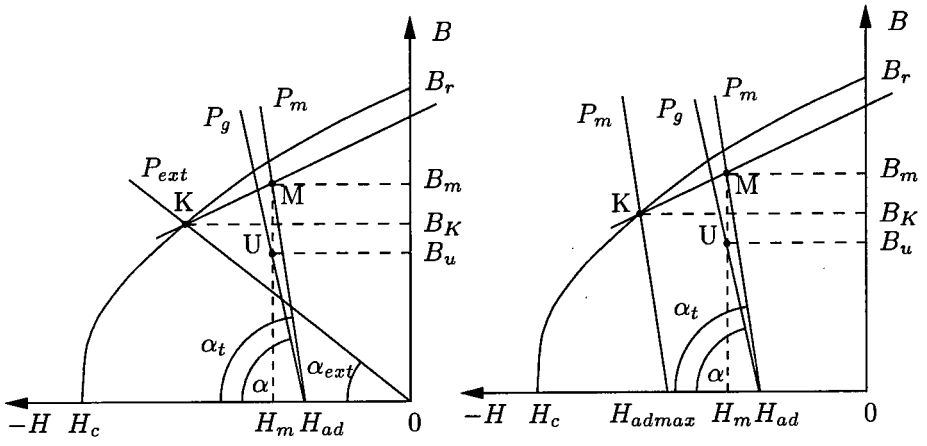

(a) External magnetisation used (b) Magnetisation with armature

Figure 3.4: Demagnetisation curve of a PM for finding the origin of the recoil line and operating point when external magnetisation was used

where

$$a = \frac{1}{n}\sum_{i=1}^{n}\left[\frac{H_c}{H_i} + \frac{B_r}{B_i} - \frac{H_c}{H_i}\frac{B_r}{B_i}\right] \tag{3.32}$$

where (B_i, H_i) are coordinates of points on the demagnetisation curve. For rare-earth PMs the above equation can be simplified due to the practically linear demagnetisation curve of these magnets, i.e.

$$B = B_r(1 - \frac{H}{H_c}) \tag{3.33}$$

The point at which the PM was magnetised is important when trying to determine its operating point. The PM could either be magnetised before being placed in the machine (external) or it could be magnetised after being placed in the machine. If the PM was magnetised after being placed in the machine the demagnetisation effect of the armature reaction determines the recoil line of the PM, while the external permeance determines the position of the recoil line otherwise.

- *External* magnetisation means the recoil line is determined by the external leakage permeance P_{ext}. For the external magnetic circuit

$$P_{ext} = \frac{B_{ext}S_m}{H_{ext}h_m} \tag{3.34}$$

and

$$\tan \alpha_{ext} = P_{ext} \frac{h_m}{S_m} \tag{3.35}$$

The point K, in Fig 3.4a, is obtained by combining eqns (3.26) and (3.31), where $H_{ad} = 0$, to get:

$$H_K = \frac{1}{2}\left(N_K + \sqrt{N_K^2 + \frac{4B_r H_c}{a \tan \alpha_{ext}}}\right) \tag{3.36}$$

where

$$N_K = \frac{H_c}{a} - \frac{B_r}{a \tan \alpha_{ext}} \tag{3.37}$$

- PM magnetised with *armature*, means the recoil line is determined by the demagnetising armature reaction. The origin of the recoil line, point K, is determined by the total permeance drawn from the point H_{admax}, which corresponds to the maximum MMF F_{admax} acting directly on the magnet. This current is usually the maximum current due to rotor reversal or due to a locked rotor. The point K, in Fig 3.4b, is obtained by combining eqns (3.26) and (3.31) to get:

$$H_K = \frac{1}{2}\left(N_K + \sqrt{N_K^2 + \frac{4}{a}\left(\frac{B_r}{\tan \alpha_t} - \frac{H_{admax}}{\sigma_l}\right) H_c}\right) \tag{3.38}$$

where

$$N_K = \frac{H_c}{a} + \frac{H_c}{a} - \frac{B_r}{a \tan \alpha_t} \tag{3.39}$$

The recoil line can then be written in terms of the point K as:

$$B_m = B_K + \mu_0 \mu_c (H_m - H_K) \tag{3.40}$$

where $\mu_0 \mu_c$ is the recoil magnetic permeability which is equal to the magnetic permeability at the magnetic remanent point B_r.

The operating point M on the recoil line is then, from eqns (3.26) and (3.40):

$$H_m = -\frac{B_K - \mu_0 \mu_c H_K - H_{ad} \tan \alpha_t / \sigma_l}{\tan \alpha_t + \mu_0 \mu_c} \tag{3.41}$$

The useful magnetic flux, point U, is at the intersection eqn (3.29) and H_m, as indicated on Fig 3.4. The useful magnetic flux density is:

$$B_u = \frac{\Phi_g}{S_m} \tag{3.42}$$

3.1.5 Nonlinear magnetic circuit using saturation factor

From Ampere's law the total MMF per pole pair is

$$2F_p = 2V_g + V_{ry} + 2V_{st} + V_{sy} + V_m \tag{3.43}$$

where V_g is the magnetic voltage drop (MVD) across the airgap, V_{ry} is the MVD in the rotor yoke, V_{st} is the MVD in the stator teeth, V_{sy} is the MVD in the stator yoke and V_m is the MVD across the PM.

The saturation factor k_{sat} of the magnetic circuit is defined as the ratio of the MMF per pole pair to the airgap magnetic drop taken twice, i.e.

$$k_{sat} = \frac{2(V_g + V_{st}) + V_{ry} + V_{sy} + V_m}{2V_g} \tag{3.44}$$

and

$$V_g = \frac{\Phi_g}{P_g k_{sat}} \tag{3.45}$$

3.1.6 Airgap and Leakage Permeances for different rotor configurations

The permeances are calculated using simple field plotting of the flux between two highly permeable materials. The magnetic field is divided up into simple geometric structures whose permeances can be easily defined [97]. The assumption that the permeance of the PM is high is an limitation of this method, since the permeability of most PM materials is close to that of a vacuum.

The airgap permeance consists of the permeance of the direct flux path across the airgap in parallel with the permeance due to the fringing flux. The permeance of the direct flux, in Fig 3.5 and 3.6, is:

$$P_{g1} = \mu_o \frac{w_m l}{g'} \tag{3.46}$$

where the equivalent airgap g' has to take into account the stator slots and the magnetic saturation. The mechanical airgap clearance g is increased to $g' = g k_c k_{sat}$.

The total permeance, taking into account the fringing flux (Fig 3.5 and 3.6), is:

$$P_g = P_{g1} + 4(P_{g2} + P_{g3} + P_{g4} + P_{g5}) \tag{3.47}$$

where P_{g2} to P_{g5} are the fringing fluxes for both the surface PM rotor and the buried PM

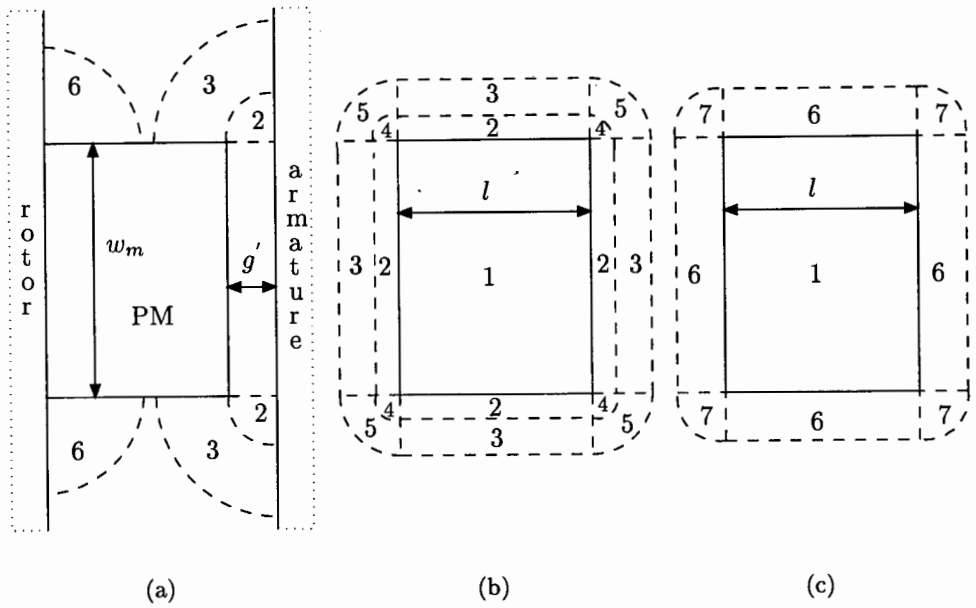

Figure 3.5: Flat model of a surface mounted PM machine: (a) longitudinal section, (b) airgap field, (c) leakage field

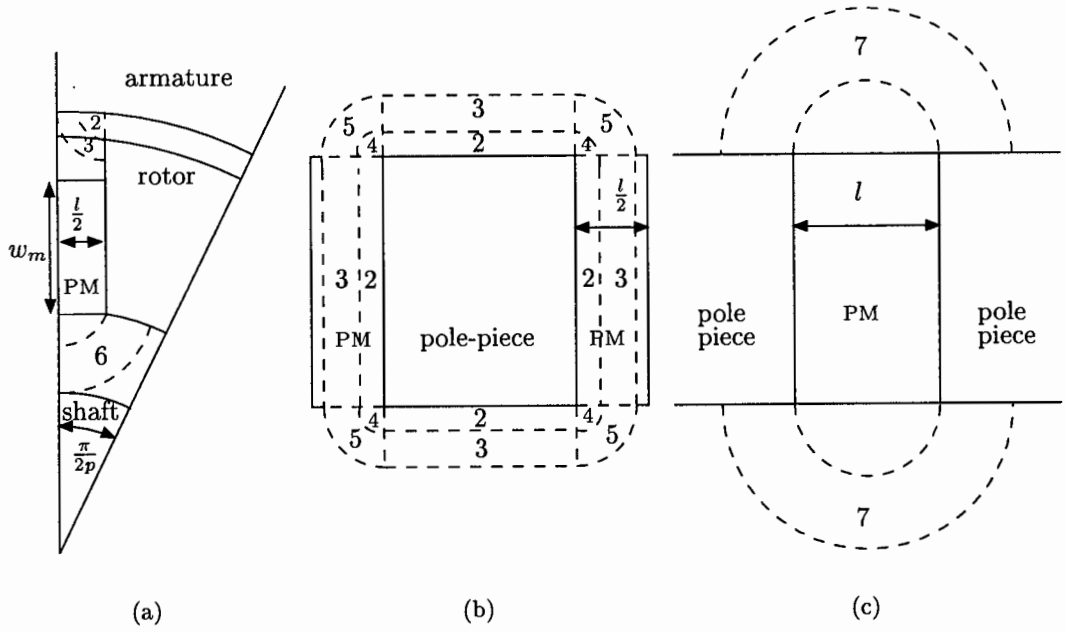

Figure 3.6: Model of a buried PM machine: (a) longitudinal section, (b) airgap field, (c) side leakage field

(spoke type) rotor. In the surface PM rotor the fringing flux is around the magnet, while in the buried PM rotor it is around the pole-shoe.

The rotor leakage permeance is essential in obtaining the operating point of the PM. The surface PM rotor and the buried PM rotor will be discussed separately since the rotor's shape determines the leakage permeance components.

The surface PM rotor has leakage flux between the PM and the rotor yoke, as shown in Fig 3.5c, i.e.

$$P_{lm} = 4(P_{l6} + P_{l7}) \tag{3.48}$$

The buried PM rotor has leakage flux between the pole-shoes, as shown in Fig 3.6a and 3.6c, i.e.

$$P_{lm} = 4(P_{l6} + 8P_{l7}) \tag{3.49}$$

where P_{l6} is the leakage below the PMs and P_{l7} is the leakage across the pole-shoe on the sides of the PMs.

3.2 Finite Element Approach

The finite element method uses the variational method for formulating the partial differential equations of the field problem in terms of a variational expression called the energy functional. The Euler equation of this functional will yield the original differential equation. The minimisation of the energy functional is implemented in the finite element method.

The machine is analysed on the assumption that it has infinite axial length ($z \to \infty$). A two dimensional model (x and y axis) is thus used with the added assumption that the slot current is axially-directed, i.e. $\vec{J} = \vec{k}J(x,y)$, and the additional magnetisation vector $\vec{M}_o = M_{ox}.\vec{i} + M_{oy}.\vec{j}$ of the medium, with a resultant axially-directed magnetic vector potential, i.e. $\vec{A} = \vec{k}A(x,y)$ where $\vec{i} = 0$, $\vec{j} = 0$, $\vec{k}$ are unit vectors.

The assumptions made for further analysis are thus:

1. The end and edge effects are neglected, and no field variations are assumed to occur in the axial direction (z-direction).

2. The permeability of the iron is modelled as a non-linear function of the field strength.

3. Temperature effects on the permeability are ignored.

4. The source function is represented by a current density distribution in the cross-section of ideal conductors.

The above simplifications allow for the simplification of the general Poisson's equation used for magnetostatic fields in vector potential $\vec{A}$. Poisson's equation is then:

$$\nabla \times (\nu \times \nabla \vec{A}) = \vec{J} \tag{3.50}$$

where ν is the reciprocal of the magnetic permeability (μ).

The nonlinear Poisson's equation for z directional current density and magnetic vector potential becomes:

$$\frac{\partial}{\partial x}(\nu(\frac{\partial \vec{A}}{\partial x})) + \frac{\partial}{\partial y}(\nu(\frac{\partial \vec{A}}{\partial y})) = -\vec{J} \tag{3.51}$$

which is subject to the appropriate Dirichlet and homogeneous Neumann boundary conditions set on a closed surface. The Dirichlet boundary condition is $\vec{A} = f(s)$ and the homogeneous Neumann condition is $\frac{\partial \vec{A}}{\partial \vec{n}} = 0$ where $f(s)$ is a specified function along a boundary and n represents a space coordinate normal to the modelled surface [106].

The field problem can now be written in variational terms as a energy functional as:

$$F = \int\int_R (\int_0^B \vec{H} d\vec{B}) dxdy - \int\int_R \vec{J}\vec{A} dxdy \tag{3.52}$$

where R is the model domain.

In isotropic materials the energy functional can be simplified further depending in the type of ferromagnetic material:

- Soft magnetic materials

$$\vec{B} = \mu_0(\vec{H} + \vec{M}) = \mu_0(1 + \chi)\vec{H} = \mu\vec{H} \tag{3.53}$$

$$F = \int\int_R (\frac{1}{2\mu}B^2 - \vec{J}\vec{A}) dR \tag{3.54}$$

- Hard magnetic materials

$$\vec{B} = \mu_0(\vec{H} + \vec{M}) + \vec{B}_r = \mu_0(1 + \chi)\vec{H} + \vec{B}_r = \mu_m\vec{H} + \vec{B}_r \tag{3.55}$$

$$F = \int\int_R (\frac{1}{2\mu_m}B^2 - \frac{1}{\mu_m}\vec{B}_r\vec{B} - \vec{J}\vec{A}) dR \tag{3.56}$$

where $\vec{M}$ is the magnetisation density of the ferromagnetic material, χ is the magnetic susceptibility and μ_m is the magnetic permeability of hard magnetic materials. Eqn (3.55) assumes that the magnet remains in a linear operating region under all conditions, this approximation is true for rare earth magnets. The magnetic permeability μ_m is thus equal to the inner

permeability of the magnet which is approximately equal to the recoil permeability, shown in eqn (3.40), for rare earth magnets.

The finite element analysis method is used with a discretised model of small sub-regions, called elements. The elements are connected at node points and their vertices become the element boundaries. The unknown field variable over each element is approximated by continuous functions expressed in terms of the nodal values of the field variable. The functions defined over each finite element are called interpolation functions or shape functions. The field variable, magnetic vector potential (A), has a value inside each element as:

$$A_k(x,y) \approx \sum_{i}^{n} N_i(x,y)A_i \tag{3.57}$$

where $N_i(x,y)$ is the shape function of the ith node, A_i is the magnetic vector potential at the ith node and the index i ranges over the number of element vertices (n).

The energy functional can be written for each element within a model where the total energy functional is the sum of the individual functionals:

$$F = \sum_{e=1}^{N_e} F_e \tag{3.58}$$

where N_e is the total number of elements in the model.

The energy functional for a particular element can then be written using eqn (3.56) and eqn (3.57) as:

$$F_e = \int\int_R (\frac{1}{2\mu_m}|\nabla \times (\sum_{i=1}^{n} N_i A_i \vec{k})|^2 - \frac{1}{\mu_m}\vec{M}_r \nabla \times (\sum_{i=1} nN_i A_i \vec{k}) - j\sum_{i=1} nN_i A_i)dR \tag{3.59}$$

where $\vec{k}$ is an unit vector.

The variational method is actually the minimisation of the energy functional by setting its first derivative with respect to every vertex value $\vec{A}_i$ to zero, so that:

$$\frac{\partial F}{\partial \vec{A}_i} = \sum_{e=1}^{N_e} \frac{\partial F_e}{\partial \vec{A}_i} = 0 \tag{3.60}$$

The solution of the minimisation function when using a Cartesian coordinate system per element is:

$$\frac{\partial F_e}{\partial A_i} = \int\int_R (\frac{1}{\mu_m}(N'_{ix}\sum_{j=i}^{n} N'_{jx}A_j + N'_{iy}\sum_{j=1}^{n} N'_{jy}A_j) - \frac{1}{\mu_m}(M_{rx}N'_{ix} - M_{ry}N'_{iy}) - jN_i)dxdy \tag{3.61}$$

where $N'_{ix} = \frac{\partial N_i}{\partial x}$ and $N'_{iy} = \frac{\partial N_i}{\partial y}$ from the shape function.

The minimisation of eqn (3.61) is carried out for all the elements of the field region and can be expressed in matrix form in which the unknown vector potential is determined

$$[S].[A] = [J] \tag{3.62}$$

where J is called the forcing vector and S is the stiffness matrix which is nonlinear, symmetric, sparse and band structured.

The matrix S is nonlinear since it depends not only on the shape and the size of the elements but also on the reluctivities, which depend on A. The problem is thus a nonlinear algebraic one which is solved using the Newton-Raphson method [105]:

$$A^{k+1} = A^k - [\frac{\partial}{\partial A_k} S^k A^k]^{-1}(S^k A^k - J) \tag{3.63}$$

3.2.1 Winding inductances

The winding inductance can be expressed with the aid of the dimensions and permeability of the magnetic circuit using the FEM. These inductance calculations incorporate circuit theory with the field theory. The following methods are used in the FE analysis of electrical machines and devices:

(a) the magnetic field energy gives the *static linkage inductances* as:

$$L_e = \frac{2w_\mu}{I_m^2} \tag{3.64}$$

where w_μ is the energy of the magnetic field excited by the circuit and I_m is the maximum current in the circuit. The magnetic field energy is calculated using the FEM from :

$$w_\mu = \frac{1}{2}\int \vec{A} \cdot \vec{J} ds \tag{3.65}$$

where $\vec{J}$ is the current density of a particular element [57].

This method has been used to calculate the reactances of a synchronous machine [88] using a simplified FEM that excluded the stator slots.

The limitation of this method is that the interaction of the d-axis and q-axis stator currents on one another cannot be calculated. The effect of the permanent magnet field, which increases the saturation levels within the model, could not be included in the inductance calculations.

(b) the magnetic flux linkage and magnetic vector potential method gives the *static linkage inductance* in the form:

$$L = \frac{\phi_m}{I_m} = \frac{\int_S \vec{B_m} \cdot \vec{dS}}{I_m} = \frac{\int_S \nabla \times \vec{A_m} \cdot \vec{dS}}{I_m} \tag{3.66}$$

On the basis of Stoke's theorem the flux linkage in any given contour can be calculated as the line integral of vector potential around the contour l, i.e.

$$\phi_m = \oint_l \vec{A}.\vec{dl} \tag{3.67}$$

which is used in eqn (3.66). This total flux between the phase windings includes the stator slot, tooth top and differential leakage in its calculation. The leakages have to be calculated separately and subtracted from the total flux if the individual d-axis and q-axis magnetising inductances are required.

(c) the method of differentiating the magnetic linkage flux and current allows for calculating the so called *dynamic inductance*

$$L_d = \left(\frac{d\phi/dt}{di/dt}\right)_{\phi_m} = -\left(\frac{edt}{di}\right)_{E_m} = \left(\frac{d\phi}{di}\right)_{\phi_m} \tag{3.68}$$

(d) the energy perturbation method gives the so-called *incremental* and *apparent* winding self and mutual inductances [33, 81].

Consider the terminal voltage of the j^{th} winding can be written as:

$$v_j = r_j i_j + \sum_{k=1}^{n} [\frac{\partial \phi_j}{\partial i_k} \frac{di_k}{dt} + \frac{\partial \phi_j}{\partial \theta} \frac{d\theta}{dt}] \tag{3.69}$$

where n is the number of coupled windings and voltage is for a particular rotor position $d\theta/dt = 0$. The incremental inductance is the partial derivative of the flux linkage ϕ_j with respect to a winding current i_k is defined as:

$$L_{jk}^{inc} = \frac{\partial \phi_j}{\partial i_k} \tag{3.70}$$

The total stored magnetic energy in the windings due to the flux linkage is:

$$W = \sum_{j=1}^{n} [\sum_{k=1}^{n} \int_{i_k(0)}^{i_k(t)} (L_{jk}^{inc} i_j) di_k] \tag{3.71}$$

The total stored magnetic energy can be split into self and mutual terms as shown in [81]. The partial derivatives of the total stored magnetic energy give the self and mutual inductances of the windings, as shown in [81], are:

$$L_{jj}^{inc} = \frac{\partial^2 W}{\partial(\triangle i_j)^2} \tag{3.72}$$

and

$$L_{jk}^{inc} = \frac{\partial^2 W}{\partial(\triangle i_j)\partial(\triangle i_k)} \tag{3.73}$$

The incremental inductances in eqns (3.72) and (3.73) can be expressed in finite difference form as [23]:

$$L_{jj}^{inc} \approx [W(i_j - \triangle i_j) - 2W + W(i_j + \triangle i_j)]/(\triangle i_j)^2 \tag{3.74}$$

and

$$\begin{aligned} L_{jk}^{inc} \approx\ & [W(i_j + \triangle i_j, i_k + \triangle i_k) - W(i_j - \triangle i_j, i_k + \triangle i_k) \\ & -W(i_j + \triangle i_j, i_k - \triangle i_k) + W(i_j - \triangle i_j, i_k - \triangle i_k)]/(4\triangle i_j \triangle i_k) \end{aligned} \tag{3.75}$$

$$\tag{3.76}$$

The calculation of the apparent inductances can be calculated in a similar way as the incremental inductances. The energy perturbations calculated for the incremental and apparent inductances are based on the respective reluctivities, ν^{inc} and ν^{app} which are defined as:

$$\nu^{inc} = \frac{\partial H}{\partial B} \qquad \nu^{app} = \frac{H}{B} \tag{3.77}$$

Many authors have used method (b) in finite element analyses since as early as 1971 [27, 32, 43, 44]. These early authors were also developing the FEM and ensuring convergence of their solutions. Some of these early models had fairly course meshes, used first order shape functions, where cumbersome and suffered from convergence problems. Recent papers have used this method very successfully due to the improvements in the finite element method and the increased computing power available [3, 26, 49, 67, 110]. Permanent magnet synchronous machines have also been analysed [25, 69, 93, 100, 114].

An extension of the maximum linkage flux method is to obtain a flux plot through the airgap of the motor. This will not give the linkage flux including stator leakage, but simply the d-axis and q-axis linkage flux. The first harmonic components of this main flux gives the magnetising reactances [91, 92, 95]. A combination of the maximum linkage flux method and

the flux plot through the airgap method will give the magnetising reactance as well as the stator leakage reactance, excluding the end connection reactance.

This method is easy to implement using a finite element package, since it can be automated which will be important when trying to find the performance characteristics at a particular input voltage using an iterate loop, as described in Chapter 4.

The energy perturbation method (d) is a powerful method when calculating transient reactances. This method does however calculate apparent inductances or static inductances and will thus be analysed in comparison to the flux linkage method (b), in Chapter 4.

Chapter 4

Calculation of Synchronous Reactances and Electromotive Forces

The methods of calculating synchronous reactances and electromotive forces (EMF) can be classified as follows:

(a) analytical methods where form factors of armature and field windings are calculated, assuming periodical distribution of magnetic flux density and MMF.

(b) methods using an initial analog or numeric methods to model the magnetic field distribution and an analytical or numerical integration to obtain the form factors.

(c) numerical modelling such as the finite difference and finite element methods.

The first analytical method uses general equations that are not specific to the machine being analysed. The second method is more useful since it uses a better approximation of the magnetic flux distribution in calculating the form factors and nowadays the hardware and software is affordable. The second method and the finite element method have been fully developed in this Chapter, and the results have been compared to experimental results.

4.1 Analytical Methods

4.1.1 Calculation of the magnetic flux density distribution

Due to the large number of simplifications made in the calculation of the induced EMF and synchronous reactances when using classical theory, a closer analysis of the actual magnetic flux distribution within the airgap is necessary. The magnetic flux distribution through the airgap for a number of different permanent magnet synchronous motors, with different rotors,

has been drawn. The idea is to obtain a set of equations for the form factors used in the calculation of induced EMF and synchronous reactance that are applicable to most PM rotor shapes. Normally, in a simplified analysis the assumption is made that the ferromagnetic materials are unsaturated and the fringing flux is marginal. A saturation factor will however be included in the final equation. The distribution of the flux through the airgap is useful in determining the armature reaction factors of the permanent magnet machines. The finite element method includes the fringing flux.

Two basic permanent magnet synchronous motor models have been used in this analysis. The one having surface mounted permanent magnets and the other having buried magnets. Variations of these models have been made to ensure the generalisation of the form factors developed.

Figs 4.1, 4.2, 4.3 and 4.4 show the magnetic flux density distribution for different shapes of surface mounted motors, while Fig 4.5 shows the flux density for a buried magnet motor obtained from finite element modelling.

4.1.2 Form Factors

Since the airgap is not uniform over the whole pole, the field loses its sinusoidal form. The increased harmonic content of the induced EMF causes a reduction in the amplitude of the fundamental harmonic EMF waveform. To determine this reduction in the amplitude of the fundamental field wave, the distortion of the field through the airgap is estimated. The form factor indicates the degree by which the fundamental harmonic has been reduced. The form factors for the excitation field, direct-axis armature reaction and quadrature-axis armature reaction are calculated using the Fourier series.

The form factor of the main field is defined as the ratio of the *first harmonic amplitude-to-the maximum value of the normal component of the main field magnetic flux density* along the d-axis, i.e.

$$k_f = \frac{B_{mg1}}{B_{mg}} \tag{4.1}$$

The peak values of the first harmonic B_{mg1} of the main flux density can be calculated as coefficients of the Fourier series for $\nu = 1$,

$$B_{mg1} = \frac{2}{\pi} \int_{-0.5\pi}^{0.5\pi} B(x) \cos x dx \tag{4.2}$$

The form factors of the armature reaction are defined as the ratios of the *first harmonic amplitudes-to-the maximum values of the normal component of the armature reaction magnetic flux densities* in the d-axis and q-axis, respectively, i.e.

$$k_{fd} = \frac{B_{ad1}}{B_{ad}} \qquad\qquad k_{fq} = \frac{B_{aq1}}{B_{aq}} \tag{4.3}$$

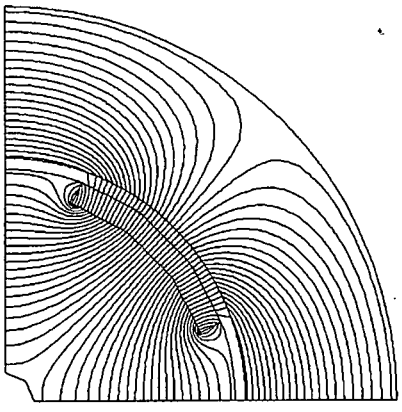

(a) Flux distribution of Main field

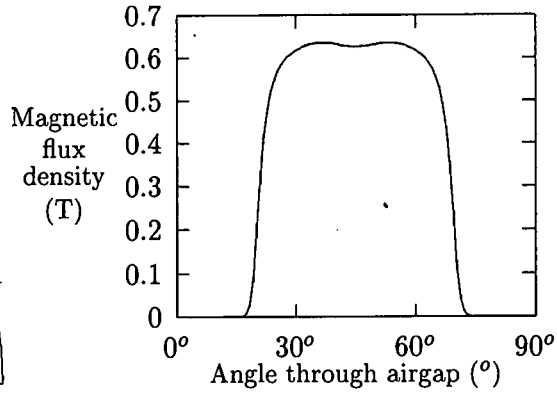

(b) Main field magnetic flux density in airgap

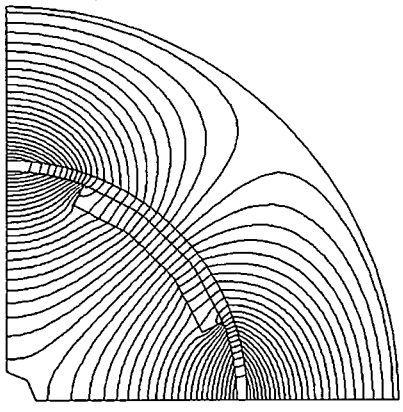

(c) Flux distribution of d-axis

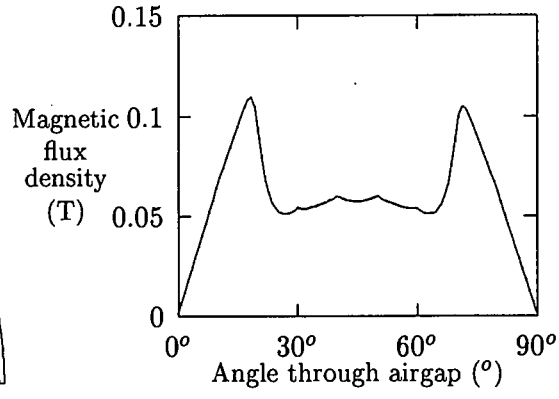

(d) d-axis magnetic flux density in airgap

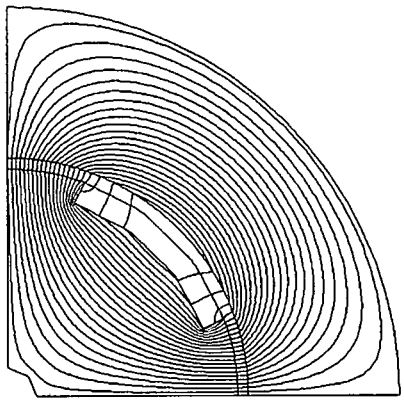

(e) Flux distribution of q-axis

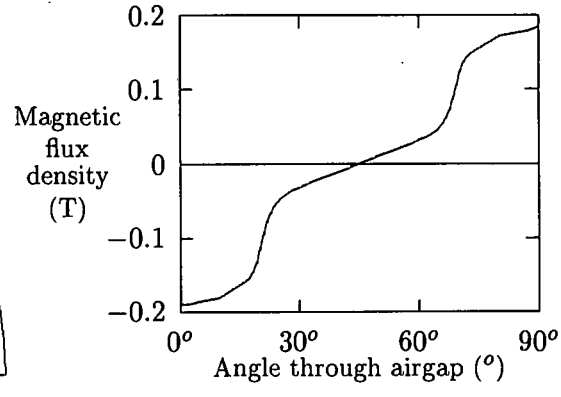

(f) q-axis magnetic flux density in airgap

Figure 4.1: Flux distribution and magnetic flux density plots of a permanent magnet machine with a smooth magnet inset in the rotor

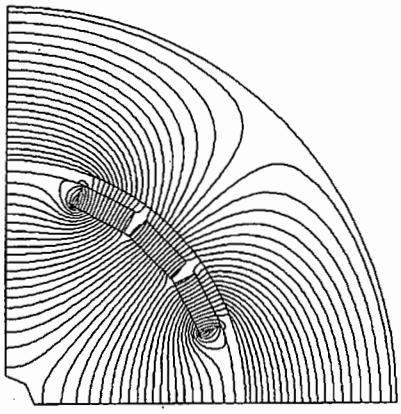

(a) Flux distribution of Main field

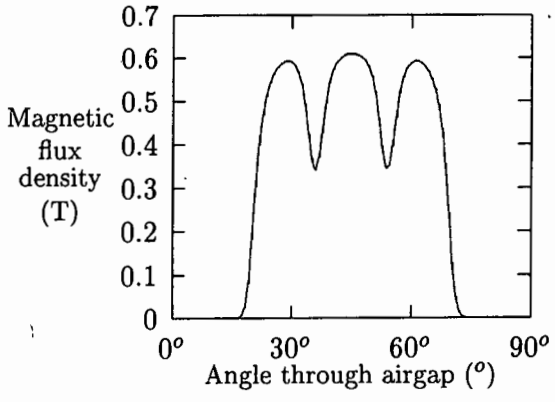

(b) Main field magnetic flux density in airgap

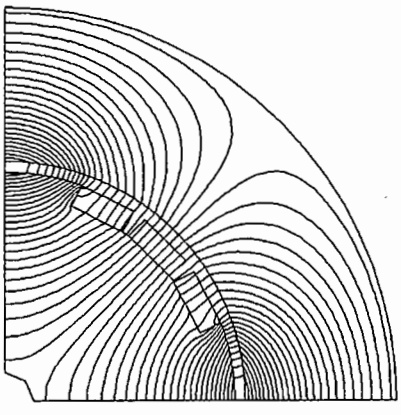

(c) Flux distribution of d-axis

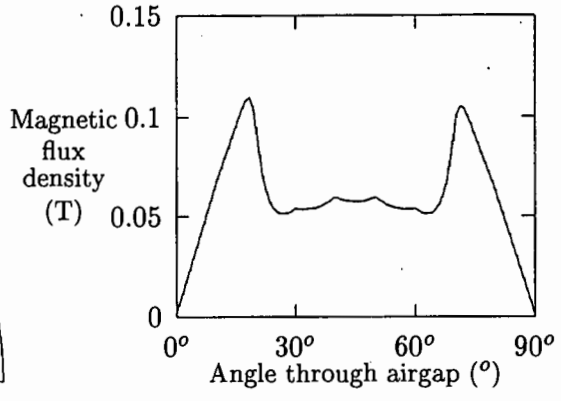

(d) d-axis magnetic flux density in airgap

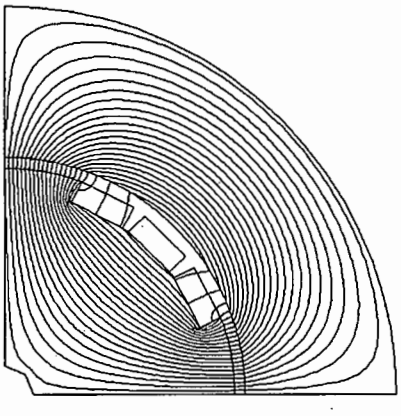

(e) Flux distribution of q-axis

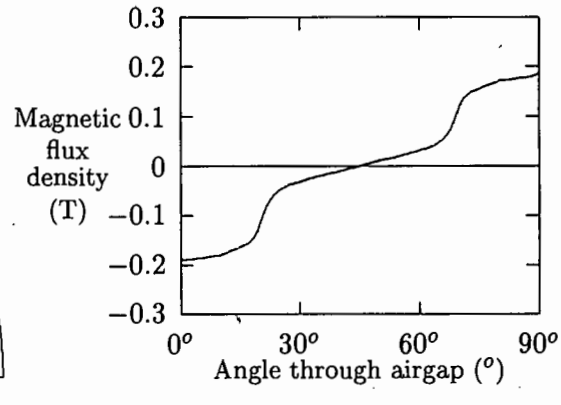

(f) q-axis magnetic flux density in airgap

Figure 4.2: Flux distribution and magnetic flux density plots of a permanent magnet machine with a segmented magnet inset in the rotor

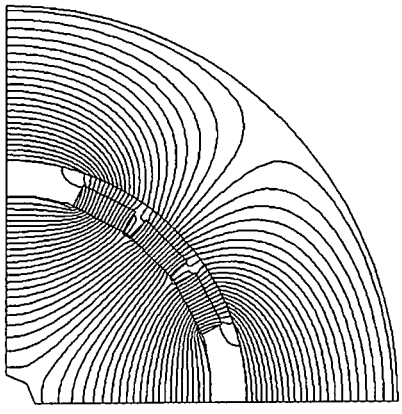

(a) Flux distribution of Main field

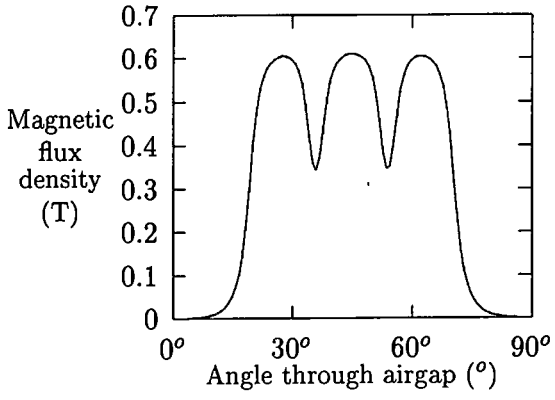

(b) Main field magnetic flux density in airgap

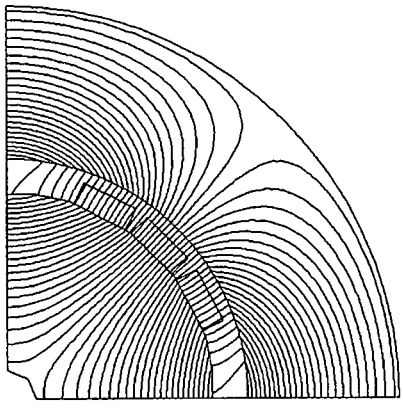

(c) Flux distribution of d-axis

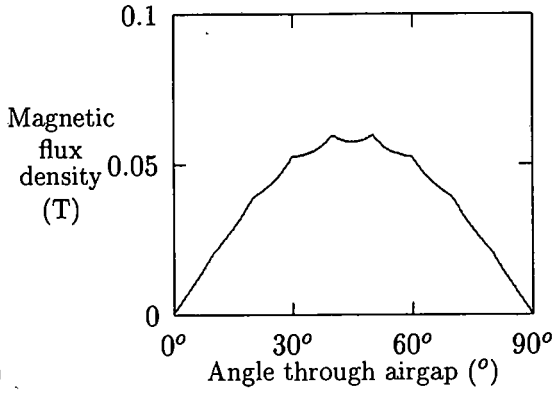

(d) d-axis magnetic flux density in airgap

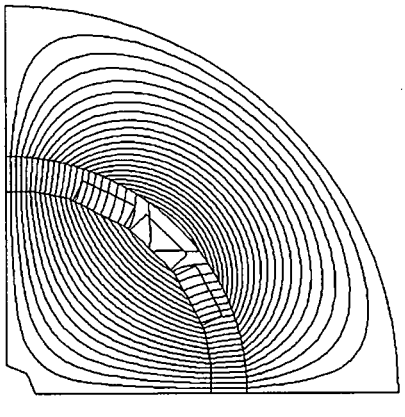

(e) Flux distribution of q-axis

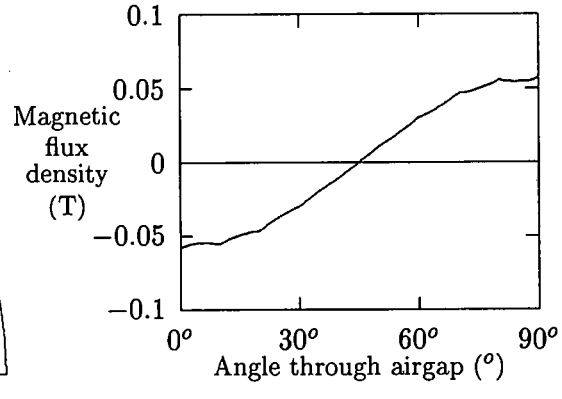

(f) q-axis magnetic flux density in airgap

Figure 4.3: Flux distribution and magnetic flux density plots of a permanent magnet machine with a segmented magnet pole which is surface mounted on the rotor

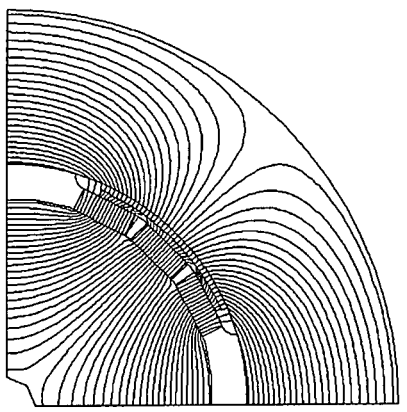

(a) Flux distribution of Main field

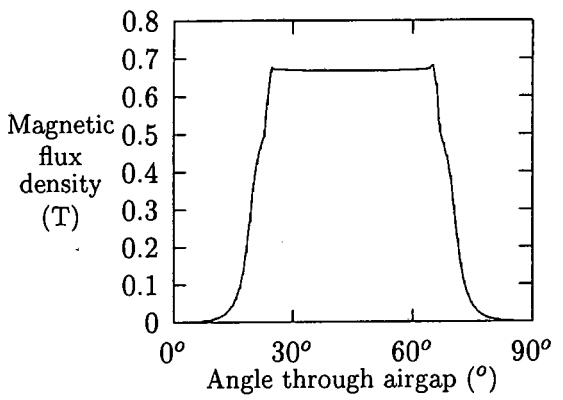

(b) Main field magnetic flux density in airgap

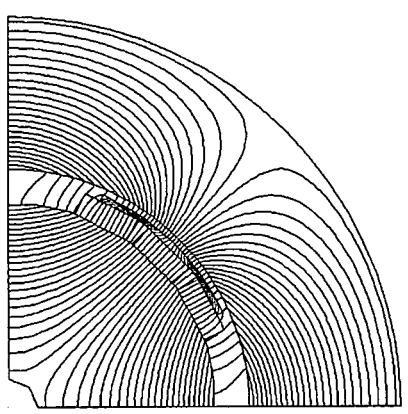

(c) Flux distribution of d-axis

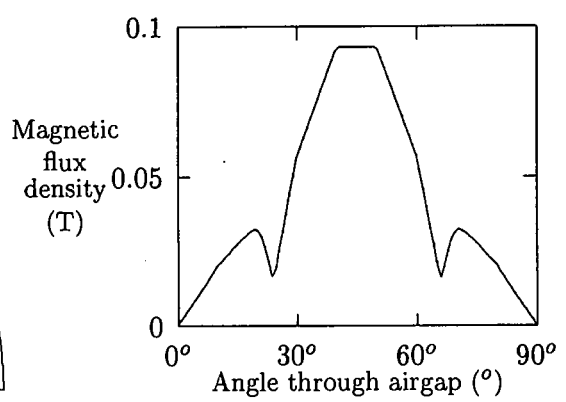

(d) d-axis magnetic flux density in airgap

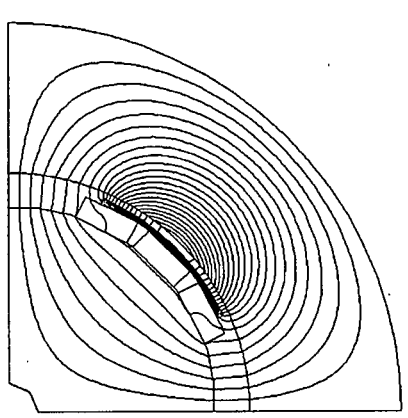

(e) Flux distribution of q-axis

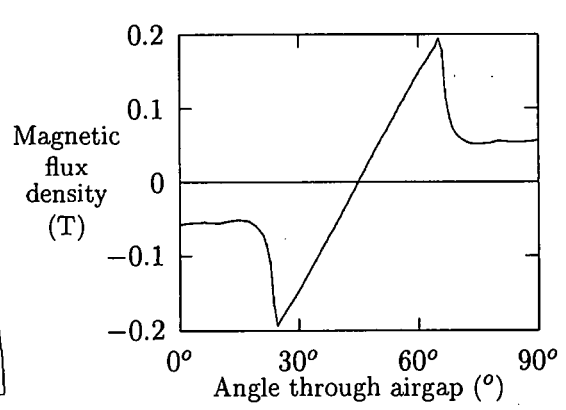

(f) q-axis magnetic flux density in airgap

Figure 4.4: Flux distribution and magnetic flux density plots of a permanent magnet machine with a segmented magnet pole which is surface mounted on the rotor with a steel pole shoe

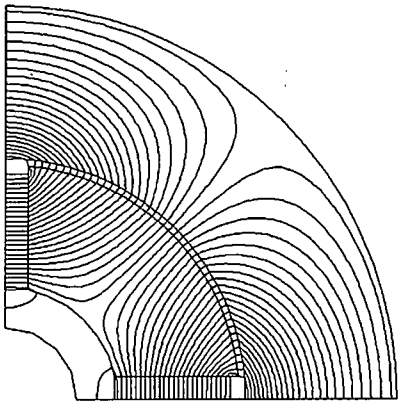

(a) Flux distribution of Main field

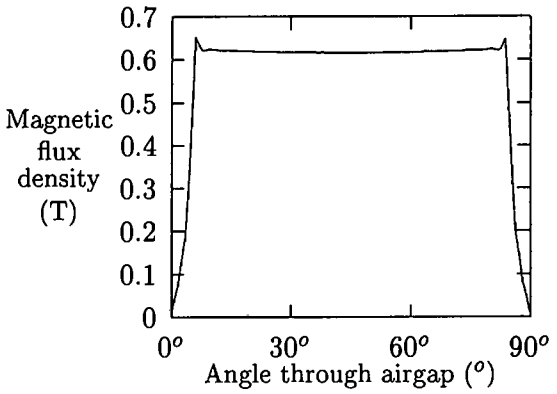

(b) Main field magnetic flux density in airgap

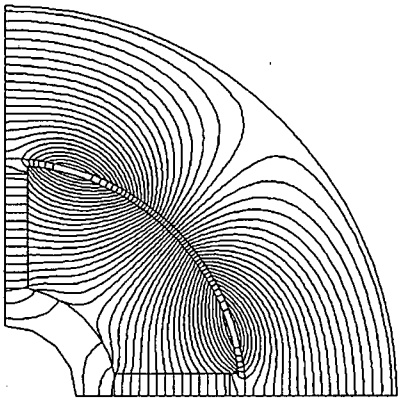

(c) Flux distribution of d-axis

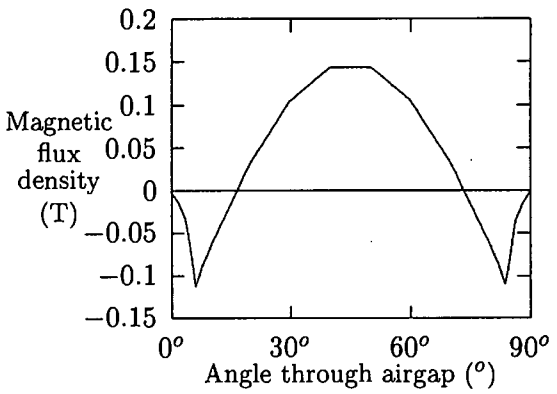

(d) d-axis magnetic flux density in airgap

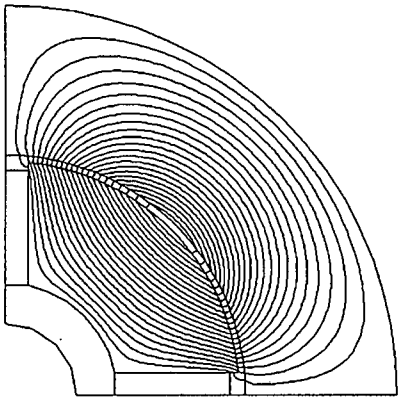

(e) Flux distribution of q-axis

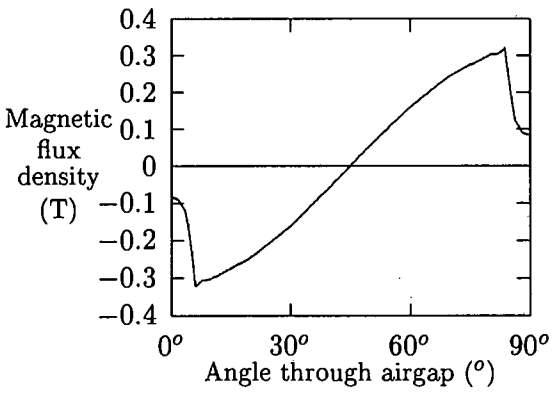

(f) q-axis magnetic flux density in airgap

Figure 4.5: Flux distribution and magnetic flux density plots of a permanent magnet machine with buried magnets in the solid steel rotor

The peak values of the first harmonics B_{ad1} and B_{aq1} of the armature magnetic flux density can be calculated as coefficients of the Fourier series for $\nu = 1$,

$$B_{ad1} = \frac{4}{\pi} \int_0^{0.5\pi} B(x) \cos x dx \tag{4.4}$$

$$B_{aq1} = \frac{4}{\pi} \int_0^{0.5\pi} B(x) \sin x dx \tag{4.5}$$

Main magnetic field

The main magnetic field, for surface mounted permanent magnet motors, can be broken up into three main regions, the area above the magnets, the area between the magnets and the area on the sides of the magnets, shown in Figs 4.1 to 4.4. These three regions are simplified into two regions, the area above the magnets and the area not above the magnets.

The regions of the main magnetic field for the buried PM motors can also be broken up in the same way. The two regions are, the area above the steel rotor and the area above the sides of the magnets (Fig 4.5).

On the basis of the FEM analysis (Figs 4.1 to 4.5) the generalised distribution of magnetic flux density can be plotted as in Figs 4.6 and 4.7.

The first harmonic of the magnetic flux density for the distribution of the main magnetic flux density is:

(a) for rotors with inset-type PMs, surface PMs and surface PMs with mild steel pole shoes where more than one PM is used (Fig 4.6)

$$\begin{aligned} B_{mg1} &= \frac{2}{\pi} \int_{-0.5\pi}^{0.5\pi} B_{mg} \cos x dx \\ &= \frac{2}{\pi} \sum_{i=1}^{K} \int_{0.5\pi\alpha_{i1}}^{0.5\pi\alpha_{i2}} B_{mg} \cos x dx \\ &= \frac{2}{\pi} B_{mg} \sum_{i=1}^{K} [\sin(0.5\pi\alpha_{i2}) - \sin(0.5\pi\alpha_{i1})] \end{aligned} \tag{4.6}$$

where K is the number of magnet segments per pole, and $\alpha_{i1} = \alpha\pi/2$ and $\alpha_{i2} = -\alpha\pi/2$, as shown in Fig 4.6.

(i) in the case of a single smooth PMs.

$$B_{mg1} = \frac{4}{\pi} B_{mg} \sin(0.5\alpha\pi) \tag{4.7}$$

(ii) in the case of a number of PMs with gaps between them. Eqn (4.6) is used, as shown in Fig 4.6.

(b) for buried PMs rotors (Fig 4.7)

$$\begin{aligned} B_{mg1} &= \frac{4}{\pi}\int_0^{0.5\pi} B_{mg}\cos x dx \\ &= \frac{4}{\pi}B_{mg}\sin(0.5\alpha\pi) \end{aligned} \tag{4.8}$$

The form factor of the main magnetic field is the same for the surface and buried magnet configurations.

Armature reaction field in d-axis

The armature reaction fields have be modelled as perfectly sinusoidal functions along a current sheet, ignoring the effects on the flux distribution due to slotting. Calculating the amplitude of the first harmonic from the Fourier series is done in a similar way as discussed above. The rotors of both the surface mounted and buried magnet motors are broken up into two regions. These are the area above the magnets and the area above ferromagnetic material of the rotor.

On the basis of the finite element method analysis (Figs 4.1 to 4.5) the generalised distribution of magnetic flux density can be plotted as in Figs 4.8 and 4.9.

The first harmonic of the magnetic flux density for the distribution of the d-axis magnetic flux density is:

(a) for rotors with inset-type PMs, surface PMs and surface PMs with mild steel pole shoes (Fig 4.8)

$$\begin{aligned} B_{ad1} &= \frac{4}{\pi}\left[\int_0^{0.5\alpha\pi}(B_{ad}\cos x)\cos x dx + \int_{0.5\alpha\pi}^{0.5\pi}(c_g B_{ad}\cos x)\cos x dx\right] \\ &= \frac{1}{\pi}B_{ad}\left[(\alpha\pi + \sin\alpha\pi) + c_g(\pi - \alpha\pi - \sin\alpha\pi)\right] \end{aligned} \tag{4.9}$$

The coefficient $c_g = B_{ad(q)}/B_{ad(d)}$ where $B_{ad(q)}$ is the d-axis magnetic flux assuming a cylindrical rotor with a reluctance path equal to that in the q-axis and $B_{ad(d)}$ is the d-axis magnetic flux assuming a cylindrical rotor with a reluctance path equal to that in the d-axis. The coefficient c_g differs for each of the three rotor shapes. Assuming an unsaturated magnetic circuit and continuity of the tangential magnetic flux in the non-ferromagnetic gap, this coefficient can be approximately given as:

(i) in the case of inset PMs.

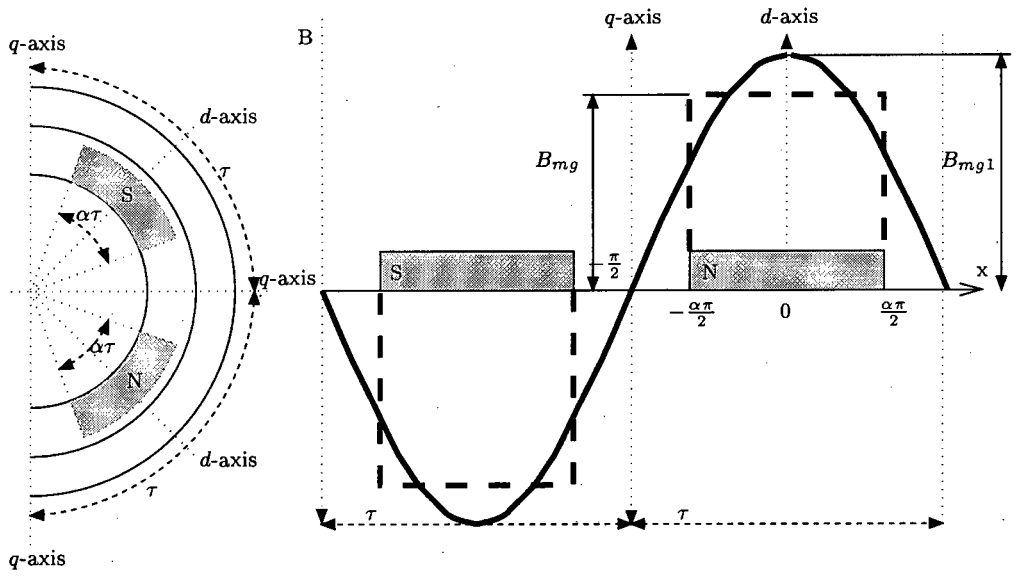

(a)

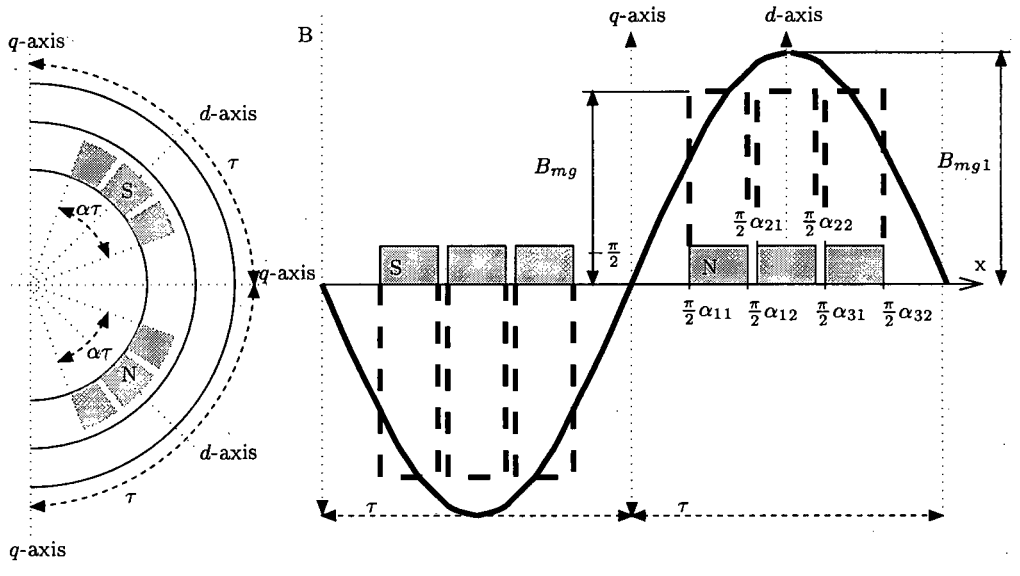

(b)

Figure 4.6: Distribution of the main magnetic flux density for rare-earth PM rotors with: (a) surface PMs that are smooth, and (b) surface PMs in segments

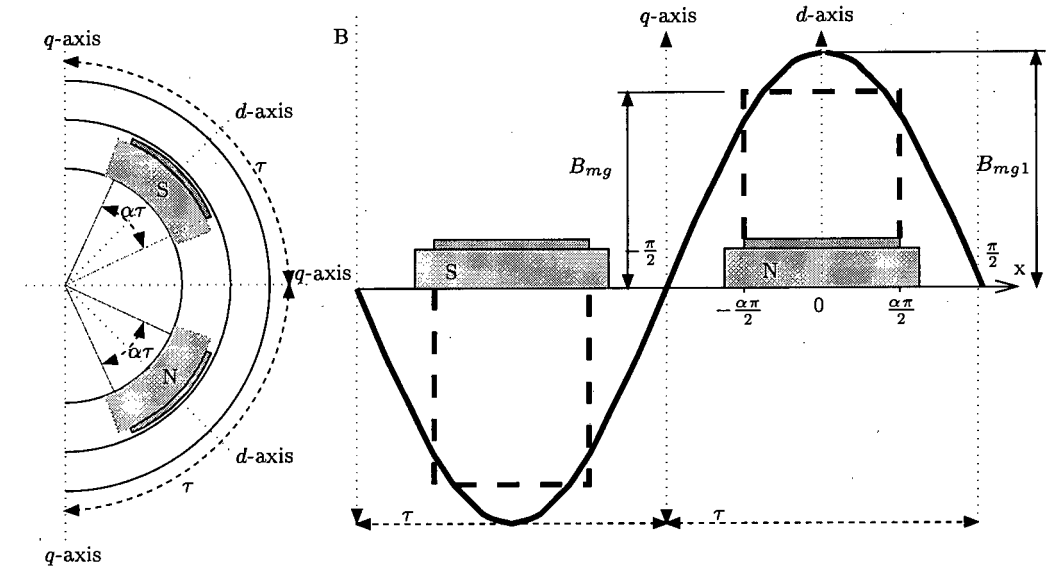

(a)

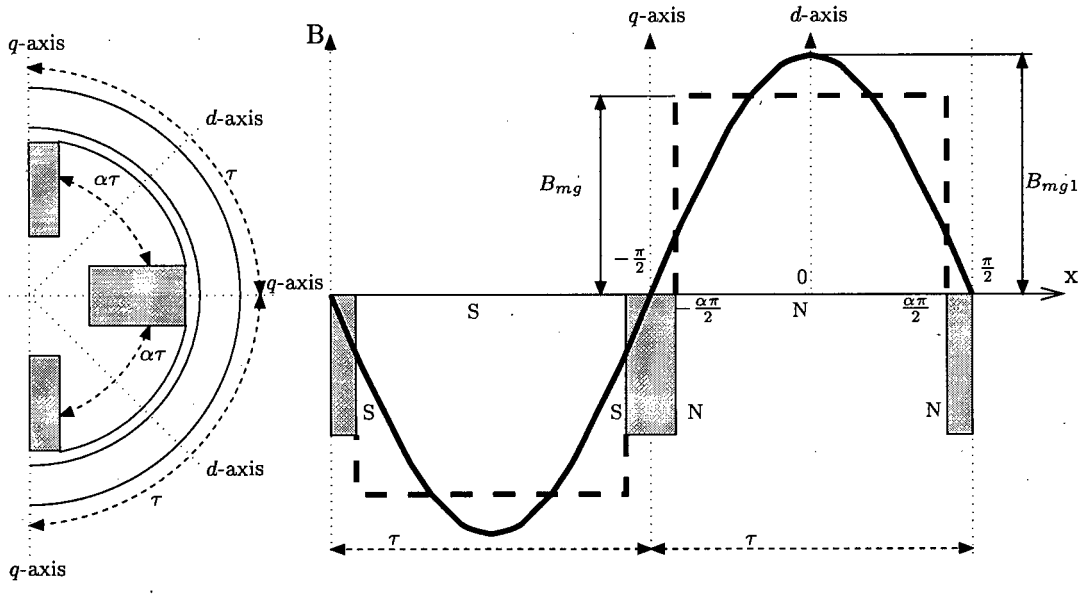

(b)

Figure 4.7: Distribution of the main magnetic flux density for rare-earth PM rotors with: (a) surface PMs rotor with pole shoes and (b) buried PMs

$$\begin{aligned} H_{ad(q)}g_q &= H_{ad(d)}g + H_{ad(d)}h_m \\ \frac{B_{ad(q)}}{\mu_0}g_q &= \frac{B_{ad(d)}}{\mu_0}g + \frac{B_{ad(d)}}{\mu_r\mu_0}h_m \\ \frac{B_{ad(q)}}{B_{ad(d)}} &= \frac{g + h_m/\mu_r}{g_q} \\ c_g &\approx \frac{g + h_m}{g_q} \end{aligned} \tag{4.10}$$

with the assumption that, for the PM, $\mu_r \approx 1$ and where g_q is the mechanical clearance between the rotor and stator in the q-axis, g is the mechanical clearance between the rotor and stator in the d-axis, h_m is the height of the PMs and μ_r is the relative permeability of the PM.

The coefficient $c_g > 1$ for inset type PM rotors.

(ii) in the case of surface PMs.

$$\begin{aligned} \frac{B_{ad(q)}}{\mu_0}g_q &= \frac{B_{ad(d)}}{\mu_0}g + \frac{B_{ad(d)}}{\mu_r\mu_0}h_m \\ \frac{B_{ad(q)}}{B_{ad(d)}} &= \frac{g + h_m/\mu_r}{g_q} \\ c_g &\approx \frac{g + h_m}{g_q} \approx 1 \end{aligned} \tag{4.11}$$

with the assumption that $\mu_r \approx 1$ and $g_q = g + h_m$.

(iii) in the case of surface PMs with mild steel pole shoes.

$$\begin{aligned} H_{ad(q)}g_q &= H_{ad(d)}g + H_{ad(d)}h_s + H_{ad(d)}h_m \\ \frac{B_{ad(q)}}{\mu_0}g_q &= \frac{B_{ad(d)}}{\mu_0}g + \frac{B_{ad(d)}}{\mu_{rs}\mu_0}h_s + \frac{B_{ad(d)}}{\mu_r\mu_0}h_m \\ \frac{B_{ad(q)}}{B_{ad(d)}} &= \frac{g + h_s/\mu_{rs} + h_m/\mu_r}{g_q} \\ c_g &\approx \frac{g + h_m}{g + h_s + h_m} \end{aligned} \tag{4.12}$$

with the assumption that $\mu_r \approx 1$, $h_s/\mu_s \ll g$, $g_q = g + h_s + h_m$, and where h_s is the thickness of the mild steel pole shoe and μ_{rs} is the relative permeability of mild steel.

The coefficient $c_g < 1$ for surface PM rotors with mild steel pole shoes.

(b) for buried PMs rotors (Fig 4.9)

$$\begin{aligned} B_{ad1} &= \frac{4}{\pi}\int_0^{0.5\alpha\pi}(B_{ad}\cos(\frac{1}{\alpha}x))\cos x dx \\ &= \frac{2}{\pi}B_{ad}\left[\frac{\alpha\sin(0.5(1+\alpha)\pi)}{1+\alpha}+\frac{\alpha\sin(0.5(1-\alpha)\pi)}{1-\alpha}\right] \\ &= \frac{2\alpha}{\pi(1+\alpha^2)}B_{ad}\cos\left(\frac{\alpha\pi}{2}\right) \end{aligned} \tag{4.13}$$

For buried PMs rotors the d-axis armature flux density changes as $\cos(x/\alpha)$.

Armature reaction field in q-axis

The q-axis armature field has been modelled using a current sheet, as was the case in the d-axis reactance calculation. The regions which the rotor are divided into are also identical to those used in the d-axis.

The first harmonic of the magnetic flux density for the distribution of the q-axis magnetic flux density is:

(a) for rotors with inset-type PMs, surface PMs and surface PMs with mild steel pole shoes (Fig 4.8)

$$\begin{aligned} B_{aq1} &= \frac{4}{\pi}\left[\int_0^{0.5\alpha\pi}(B_{aq}\sin x)\sin x dx+\int_{0.5\alpha\pi}^{0.5\pi}(c_g B_{aq}\sin x)\sin x dx\right] \\ &= \frac{1}{\pi}B_{aq}\left[(\alpha\pi-\sin\alpha\pi)+c_g(\pi-\alpha\pi+\sin\alpha\pi)\right] \end{aligned} \tag{4.14}$$

The coefficient c_g, for the three different rotors, are as described for the d-axis.

(b) in the case of buried PMs rotors (Fig 4.8c)

$$\begin{aligned} B_{ad1} &= \frac{4}{\pi}\int_0^{0.5\alpha\pi}(B_{aq}\sin x)\sin x dx \\ &= \frac{1}{\pi}B_{aq}\left[\alpha\pi-\sin\alpha\pi\right] \end{aligned} \tag{4.15}$$

The coefficients k_f, k_{fd} and k_{fq} for different rotor configurations are summarised in Table 4.1.

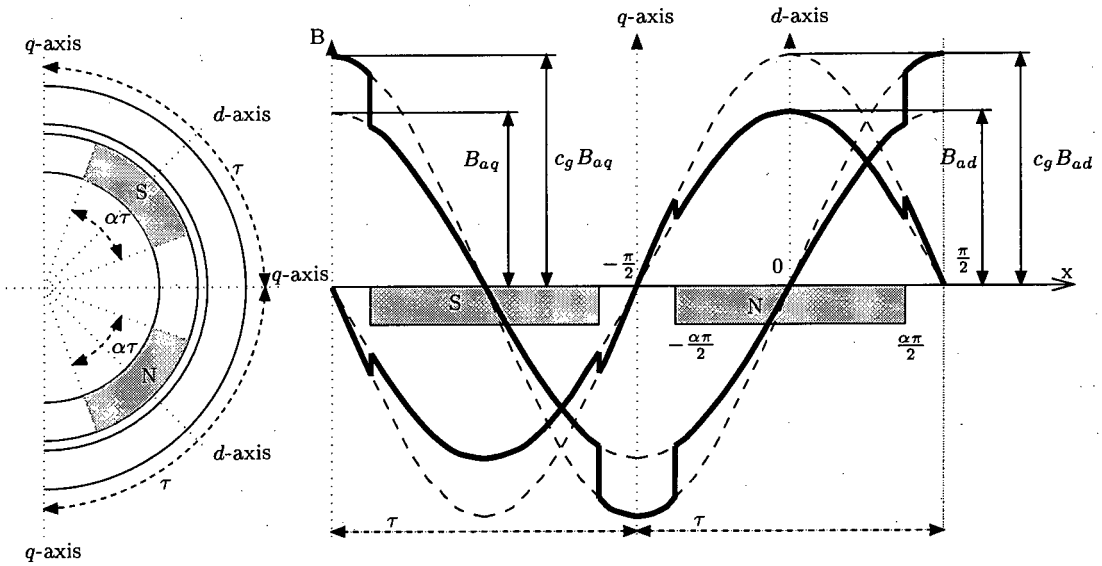

(a)

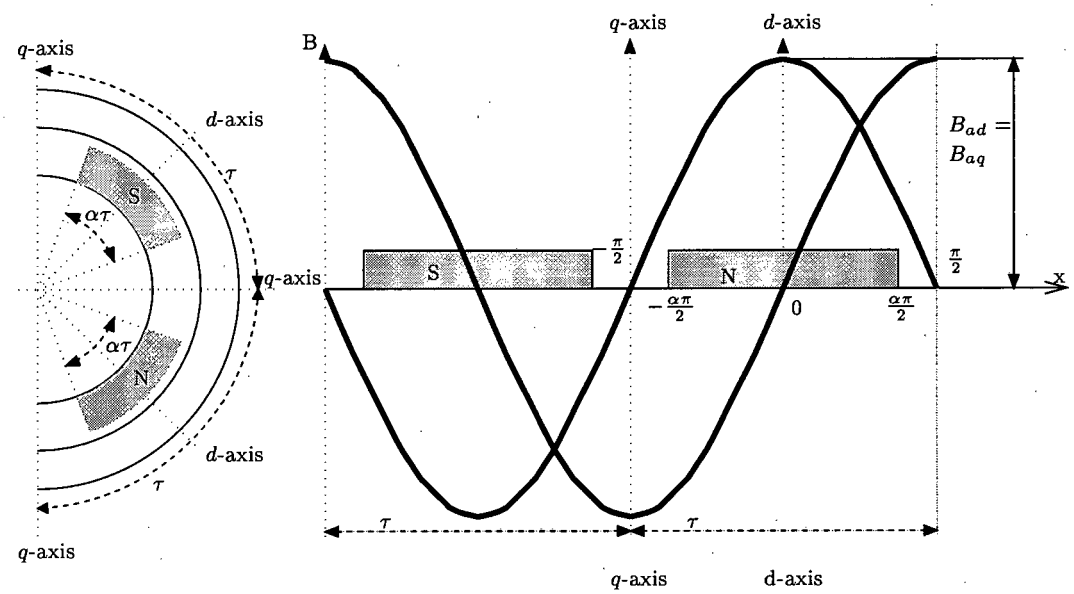

(b)

Figure 4.8: Distribution of the d-axis and q-axis magnetic flux density for rare-earth PM rotors with: (a) inset-type PM rotor (PM1), and (b) smooth surface PMs (PM2)

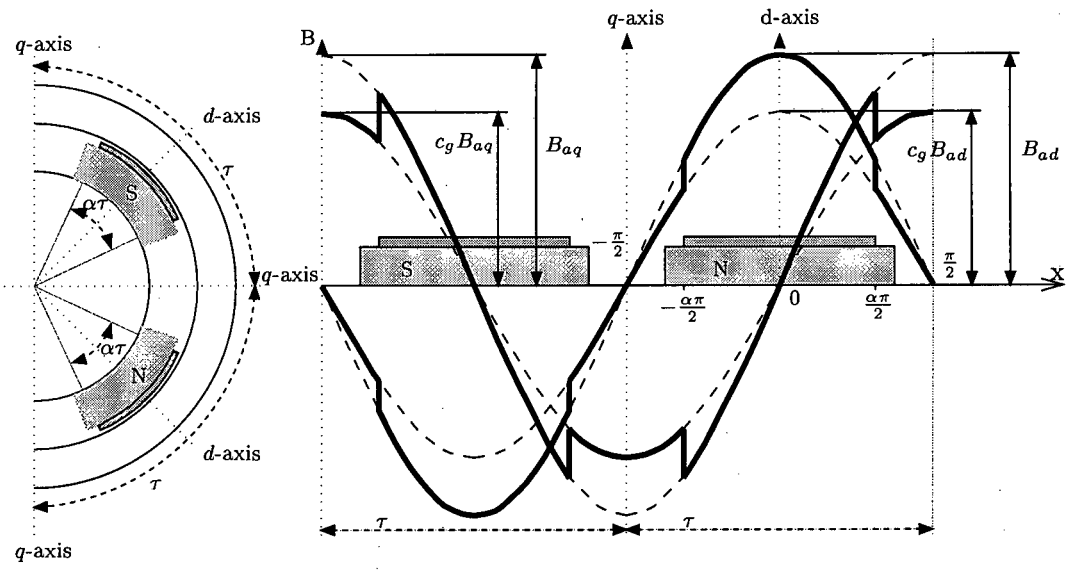

(a)

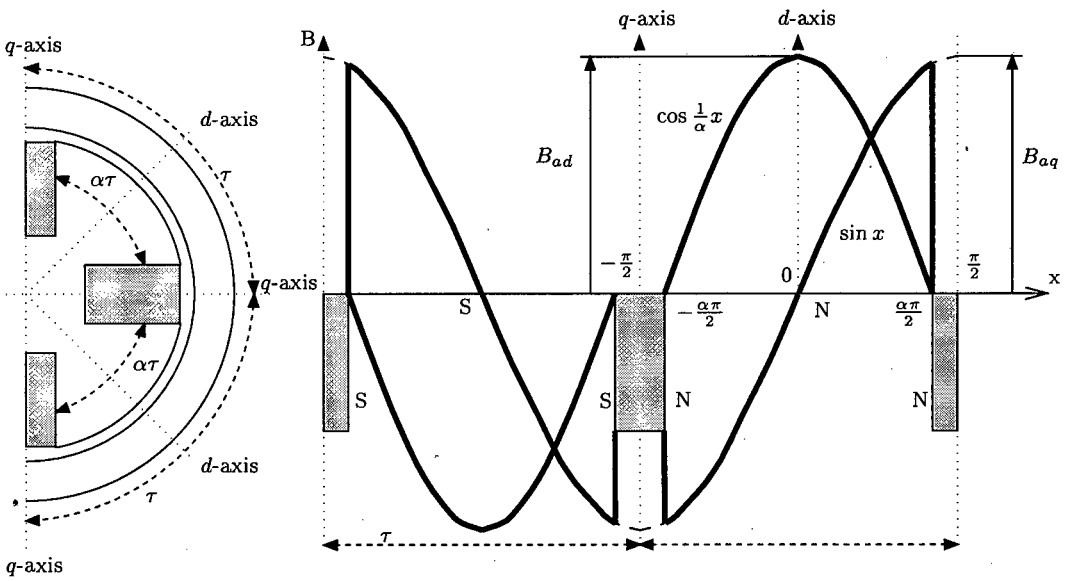

(b)

Figure 4.9: Distribution of the d-axis and q-axis magnetic flux density for rare-earth PM rotors with: (a) surface PMs rotor with pole shoes (PM3), and (b) buried PM rotor (PM4)

Table 4.1: Form factors for different rotor configurations

Rotor Configuration	Inset PM rotor and surface PM Rotor with mild steel pole shoes	Surface PM Rotor	Buried PM Rotor
Main field	$k_f = \frac{2}{\pi}\sum_{i=1}^{K}[\sin(0.5\pi\alpha_{i2}) - \sin(0.5\pi\alpha_{i1})]$	$k_f = \frac{2}{\pi}\sum_{i=1}^{K}[\sin(0.5\pi\alpha_{i2}) - \sin(0.5\pi\alpha_{i1})]$	$k_f = \frac{4}{\pi}\sin(0.5\alpha\pi)$
d-axis	$k_{fd} = \frac{1}{\pi}[\alpha\pi + \sin\alpha\pi + c_g(\pi - \alpha\pi - \sin\alpha\pi)]$	$k_{fd} = 1$	$k_{fd} = \frac{2\alpha}{\pi(1+\alpha^2)}\cos\left(\frac{\alpha\pi}{2}\right)$
q-axis	$k_{fq} = \frac{1}{\pi}[\alpha\pi - \sin\alpha\pi + c_g(\pi - \alpha\pi + \sin\alpha\pi)]$	$k_{fq} = 1$	$k_{fq} = \frac{1}{\pi}(\alpha\pi - \sin\alpha\pi)$

4.2 Finite Element Method

4.2.1 Superposition in synchronous reactance and EMF calculations

The so-called two-reaction theory of synchronous machines under load was developed at the beginning of this century. This theory was firmly based on the principle of superposition and thus could not take into account the non-linear characteristics of ferromagnetic materials.

The saturation of ferromagnetic materials in electrical machines is a function of the magnetic excitation and the armature load. For small disturbances in load it is assumed that the non-linearity is linearised in the immediate neighbourhood of the operating point. This assumption is considered reasonable since the machine parameters vary in a fairly linear fashion. This is generally due to the fact the magnetic circuit of electrical machines consists of an air path and an ferromagnetic path in series. As a result, core saturation would not have a significant effect on the average magnetic circuit permeability, in a small neighbourhood [3].

In any calculation of the synchronous reactances and EMF, under load conditions, the EMF has to be separated from the synchronous reactances. The magnetic saturation that occurs in the loaded machine, at a particular operating point, should remain the same in consequent models in the immediate neighbourhood. This is accomplished by storing the permeability of every element obtained from the loaded non-linear magnetic field calculation [26]. These permeabilities are then fixed and used in consequent linear models with load disturbances.

The methods of calculating the synchronous reactances and EMF, described below, all use linear FEM models with permeabilities obtained from the solution of the loaded machine. The effect of using a linear disturbance model means that the load disturbance does not have

to be small. Using a larger disturbance has the advantage of removing rounding-off errors due to the FEM calculation.

4.2.2 Synchronous reactance using energy perturbation

A reference angle between the d-axis, symmetrical line of rotor, and the stator phases is needed. This angle is defined as (Fig 4.10):

$$\alpha_a = \alpha p \tag{4.16}$$

where α is the mechanical radians between the centre of the rotor and the a-phase of the stator winding. The reference angle to the other phases are defined as:

$$\alpha_b = \alpha_a - \frac{2}{3}\pi \qquad \alpha_c = \alpha_a + \frac{2}{3}\pi \tag{4.17}$$

The energy perturbation method calculates the winding inductances for each stator phase. The transformation has to be made from the rotating three-phase (abc) system to the stationary two-phase ($dq\gamma$) using [59, 84]:

$$[L_{dq\gamma}] = [C][L_{abc}][C_t] \tag{4.18}$$

The synchronous reactances are then:

$$X_{sd} = 2\pi f L_{sd} \qquad X_{sq} = 2\pi f L_{sq} \tag{4.19}$$

The mutual inductance between two windings are equal $M_{ab} = M_{ba}$, although the assumption is made that the mutual inductance between different sets of windings are not assumed to be equal even through each winding has the same number of turns i.e. $M_{ab} \neq M_{ac}$, since the relative position of the rotor would influence the mutual inductance.

The energy perturbation method needs to calculate the self inductances of each phase (abc) and the mutual inductances between these phases. For a particular rotor position and load, a non-linear FEM solution yields the global stored magnetic energy, at the quiescent point [81]. This non-linear FEM solution yields the flux density in each element of the chosen grid. Given these flux densities the apparent permeability for each element can be evaluated using the operating point along the B-H curve. The energy perturbations i.e. $W(i_a \pm \triangle i_a)$ and $W(i_a \pm \triangle i_a, i_b \pm \triangle i_b)$, are calculated using linear FEM assuming that the permeability in each element is constant and equal to the apparent permeability obtained at the quiescent point, as described in Section 4.2.1. It can thus be seen that the energy perturbation method needs one non-linear FEM solution and eighteen linear FEM solutions to obtain the stator inductances for one load and rotor position, in a three-phase motor.

4.2.3 Synchronous reactances using flux linkage

The relationship between the coordinates of the finite element model, and the d-axis and q-axis have to be found. If $I_1 = 0$ then the normal component of magnetic flux density B_r determines the d-axis. From the magnetic field solution of this model a line integral through the airgap gives the distribution of the magnetic vector potential. Numerical Fourier analysis of this vector potential yields an analytical expression for the first harmonic, as follows [3, 43]:

$$\begin{aligned} A_z(p\alpha) &= a_1 cos(p\alpha) + b_1 sin(p\alpha) \\ &= A_{o1} sin(p\alpha + \alpha_d) \end{aligned} \tag{4.20}$$

where $A_{o1} = \sqrt{a_1^2 + b_1^2}$ and $\alpha_d = \arctan(b_1/a_1)$. The angle α_d relates the d-axis to the y-axis of the finite element model since it shows the angle of zero crossing of the magnetic vector potential through the airgap line contour. This angle is usually found to be $\alpha_d = 0$ due to the position of the FEM with respect to the cartesian coordinate system. The q-axis is related to the d-axis by a shift of $\pi/(2p)$ thus:

$$\alpha_q = \alpha_d + \frac{\pi}{2p} \tag{4.21}$$

The d-axis and q-axis synchronous reactances , respectively, excluding end connection leakage reactance in 2-dimensional analysis are:

$$X'_{sd} = 2\pi f \frac{\phi_{ad}}{I_d} \tag{4.22}$$

and

$$X'_{sq} = 2\pi f \frac{\phi_{aq}}{I_q} \tag{4.23}$$

where $'$ indicates the exclusion of end connection leakage reactance, and ϕ_{ad} and ϕ_{aq} are the magnitudes of the flux linkages in the d-axis and q-axis respectively, I_d and I_q are the magnitudes of the d-axis and q-axis stator current respectively and f is the stator supply frequency.

The calculation of the synchronous reactances using eqns (4.22) and (4.23) are sensitive to the values of I_d and I_q, respectively. This is due to the fact that in the full load analysis of a PM synchronous motor the values of I_d and I_q both approach zero at different load angles. The rounding off errors that occur in the FEM, amplify the error in the synchronous reactance as the armature current components tend towards zero. The use of a constant current disturbance, in both I_d and I_q, solves this problem. The synchronous reactances are then

$$X'_{sd} = 2\pi f \frac{\triangle \phi_{ad}}{\triangle I_d} \tag{4.24}$$

and

$$X'_{sq} = 2\pi f \frac{\triangle \phi_{aq}}{\triangle I_q} \tag{4.25}$$

where $\triangle \phi_{ad}$ and $\triangle \phi_{aq}$ are the changes in flux linkages at the load point in the d-axis and q-axis respectively, and $\triangle I_d$ and $\triangle I_q$ are the magnitudes of the d-axis and q-axis stator current disturbances, respectively.

The total synchronous reactances are then:

$$X_{sd} = X'_{sd} + X_{ec} \qquad\qquad X_{sq} = X'_{sq} + X_{ec} \tag{4.26}$$

The d-axis and q-axis flux linkages are obtained from the combination of the phase belt linkages. The real and imaginary components of the flux linkage represent the d-axis and q-axis flux linkages respectively in eqn (4.27).

$$\triangle \vec{\phi} = \frac{2}{3}\left(\triangle \phi_a e^{j\alpha_a} + \triangle \phi_b e^{j\alpha_b} + \triangle \phi_c e^{j\alpha_c}\right) \tag{4.27}$$

where α_a, α_b and α_c denote the angular position of the phase belt axes measured from the d-axis.

The phasor diagram for a synchronous motor shows that the rotor exciting flux and the d-axis armature flux are in the same direction while the q-axis armature flux is perpendicular to the d-axis. The real component in eqn (4.27) should not include the rotor excitation flux, thus.

$$\triangle \phi_{a\ldots c} = \phi^{I}_{a\ldots c} - \phi^{\triangle I}_{a\ldots c} \tag{4.28}$$

where $\phi^{I}_{a\ldots c}$ are the flux linkages in the phase belts during a loaded condition and $\phi^{\triangle I}_{a\ldots c}$ are the corresponding flux linkages during a change in I_d and I_q of $\triangle I_d$ and $\triangle I_q$, respectively.

The magnetic saturation that occurs in the loaded finite element solution is transferred to the problem with the disturbance in the stator current. This is done by storing the permeability of every element obtained from the loaded non-linear magnetic field calculation. These permeabilities can then be used in the linear calculation. This ensures that the saturation effects which occur in the loaded model are not ignored in the results with the current disturbance.

The flux linkage for phase belt a is:

$$\phi_a = pN_c l \sum_{i=1}^{c_1} (2A_i) \tag{4.29}$$

similarly for phases b and c, where N_c is the number of turns per coil, l is the effective stator length, c_1 is the number of coils per phase belt and A is the average vector potential per coil defined as:

$$A = \frac{1}{S_s} \sum_{j=1}^{n} S_j \left(\frac{A_1 + \ldots A_k}{k} \right) \tag{4.30}$$

where S_s is the total area of stator slot taken up by the coil, S_j is the area of the j^{th} element, n is the number of elements per stator slot and $A_1 \ldots A_k$ are the nodal vector potentials of the j^{th} element.

4.2.4 Magnetising (Mutual) Reactances using the loading method

For a two dimensional finite element model, the d-axis and q-axis fundamental components of flux in the airgap can be derived by performing a Fourier analysis on the vector potentials A around the inner surface of the stator in the airgap, as discussed above.

The Fourier series terms a_1 and b_1, which are the magnitudes of the first harmonic cosine and sine terms, represent half the q-axis and d-axis flux per pole, respectively. The flux per pole due to this fundamental harmonic is thus the resultant flux [92]:

$$\Phi_m = 2l\sqrt{a_1^2 + b_1^2} \tag{4.31}$$

and the inner torque angle, assuming $\alpha_d = 0$, is

$$\delta_i = \arctan\left(\frac{b_1}{a_1}\right) \tag{4.32}$$

This flux then induces a voltage in the stator windings:

$$E_i = \sqrt{2}\pi f \Phi_m N_1 k_{w1} \tag{4.33}$$

Writing the d-axis and q-axis components of voltage, as shown in Fig 3.1, in terms of magnetising (mutual) reactances is

$$X_{md} = \frac{E_i \cos(\delta_i) - E_o}{I_d} \tag{4.34}$$

$$X_{mq} = \frac{E_i \sin(\delta_i)}{I_q} \tag{4.35}$$

The value of the induced voltage E_o cannot adopted the value of the open-circuit voltage since for different loads the armature reactions will change the saturation level of the magnetic flux and thus change the value of E_o. The magnetic saturation that occurs in the loaded FE solution should be transferred to a problem with the current disturbance, as described in

Section 4.2.1.

The numerical Fourier analysis of the vector potentials A around the inner surface of the stator in the airgap of the linear magnetic flux model with a disturbance in the stator current give the resultant flux as:

$$\Phi_{m\triangle} = 2l\sqrt{a_{1\triangle}^2 + b_{1\triangle}^2} \tag{4.36}$$

and the inner torque angle is

$$\delta_i' = \arctan\left(\frac{b_{1\triangle}}{a_{1\triangle}}\right) \tag{4.37}$$

This flux then induces a voltage in the stator windings:

$$E_i' = \sqrt{2}\pi f \Phi_{m\triangle} N_1 k_{w1} \tag{4.38}$$

The magnetising reactances are then:

$$X_{md} = \frac{E_i' \cos(\delta_i') - E_i \cos(\delta_i)}{\triangle I_d} \tag{4.39}$$

$$X_{mq} = \frac{E_i' \sin(\delta_i') - E_i \sin(\delta_i)}{\triangle I_q} \tag{4.40}$$

and the induced EMF is

$$E_o = E_i \cos(\delta_i) - I_d X_{md} \tag{4.41}$$

4.2.5 Leakage reactance

The armature leakage reactance can be divided into the same categories as in classical machine theory.

The slot leakage reactance can be obtained from a flux plot of the leakage flux through the slot. This analysis allows the effects of saturation on the magnetic circuit to be included in the calculation [41]. These saturation levels are however not accurate when compared to the saturation levels found in the full model of the motor.

Another method of calculating the slot leakage reactance, tooth-top leakage and differential leakage is to take the difference between the calculated synchronous reactance and the magnetising reactance as:

$$X_l' = X_{sd}' - X_{md} = X_{sq}' - X_{mq} \tag{4.42}$$

The end connection reactance ideally requires a three-dimensional finite element model.

A two-dimensional approximation can be used with the following assumptions [1] :

- The end windings have no magnetic effect on each other.
- There is a uniform current density over the cross section of the end winding.
- The end winding field will not penetrate the stator core.

It has been found that due to the large number of simplifications in calculating the end connection reactance a easier and not less accurate method would be to use conventional classical methods [56]. The total leakage reactance can thus be written as:

$$X_l = X_l' + X_{ec} \tag{4.43}$$

4.2.6 FE models for synchronous reactance and induced EMF calculations

The FE solution determines the phase flux linkages for a specific rotor angle α_a and at a single instant in time. These phase flux linkages are transformed using the two-reaction (d-q) model into the d-axis and q-axis flux linkages specific to the rotor angle.

The FE solution is not only dependent on the relative position of the pole tip and armature teeth, but also on the relative position of the pole tip and armature phase belts. The armature current phase belts are time varying quantities and also change position relative to the d-axis with the variation in α_a. Fig 4.10a shows the space phasor relationship between the d-axis and the phase-belts, referenced to the centre of phase a. For different values of α_a, there is thus different armature current patterns.

The instantaneous phase currents are then:

$$i_a = I_m \cos(\theta + \alpha_a)$$

$$i_b = I_m \cos(\theta + \alpha_a - \frac{2}{3}\pi)$$

$$i_c = I_m \cos(\theta + \alpha_a + \frac{2}{3}\pi) \tag{4.44}$$

where I_m is the magnitude of the armature phase current and θ is the internal power factor of the armature current (Fig 3.1). The FE results for a number of different values of α and θ are needed. The d-axis and q-axis reactances and induced EMF can then be found using the average values over a full 360^o electrical degrees rotation.

The movement of the rotor in the FEM is done using a sliding surface model [111]. The mesh of the rotor and stator are created separately, with part of the airgap joined to both parts (Fig 4.10). A sliding surface with equidistant nodes within the airgap is generated.

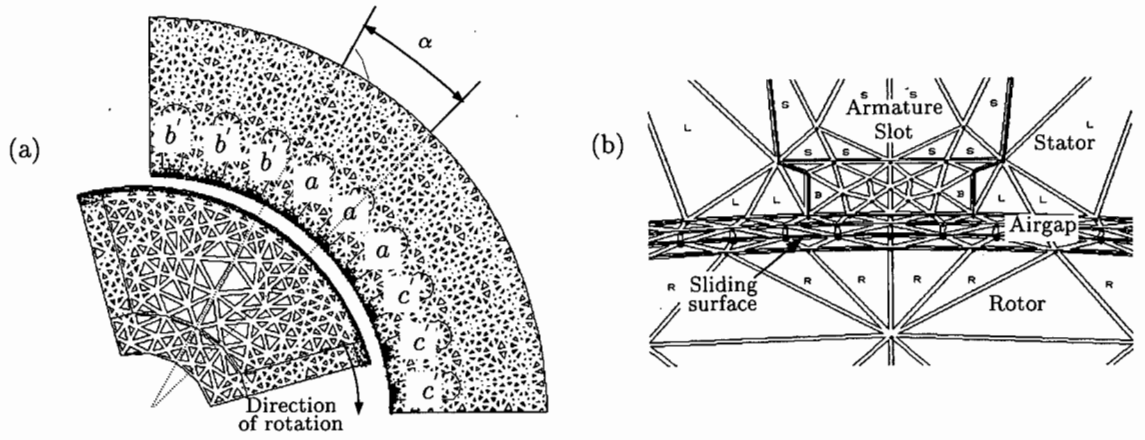

Figure 4.10: A FE model of a buried PM motor showing (a) angle α between d-axis and centre of phase a and (b) airgap sliding surface

The nodes from the rotor and stator mesh match at discrete rotor positions. Fig 4.10b shows the sliding surface in the airgap with a discrete rotation angle of 1^o mechanical degrees. This method of rotor movement avoids mesh distortion and is shown to more accurate than methods that use mesh distortion or mesh rebuilding [111].

Evaluating synchronous motor parameters using a voltage fed source

A two dimensional FEM is used in the calculation of the synchronous reactances and induced EMF. The model assumes the motor is running at a constant synchronous speed from a fixed magnitude voltage source. Damping effects are neglected since the steady-state performance is mainly of interest. Core losses are also neglected in this model. Due to the symmetry in the motors modelled, only one pole of the four poles has been model in the FEM. Periodic boundary conditions were thus used in the second order FEMs.

Fig 4.11 shows a block diagram representation of the calculation procedure. Since the FEM is current driven problem, the input to the FEM is the instantaneous values of the armature phase currents for a particular θ and α_a. An estimate of the load current I_1 is made, for a particular θ and α, for which the field distribution is calculated. The instantaneous armature phase currents are loaded into the FEM using eqn (4.44) and where $I_m = \sqrt{2}I_1$. From the FE solution the synchronous reactances X_{sd} and X_{sq}, magnetising reactances X_{md} and X_{mq}, and the open circuit EMF E_o are obtained. X_{sd} and X_{sq} are obtained using either the flux linkage or energy perturbation method, while X_{md}, X_{mq} and E_o are obtained using the loading method. Using the phasor diagram, shown in Fig 3.1, the terminal voltage V_2 for that particular load current can be obtained. If this voltage is not equal to the desired terminal voltage V a new estimate of the stator current I_1 is calculated. The iterate procedure stops

once the correct accuracy in the voltage is calculated. The synchronous motor characteristics are then stored.

The simulation steps through a number of different current phase angles θ and different rotor positions α_a to obtain the characteristics of the motor over its full load range.

Once the calculation has been done for all θ and α_a the average reactances are calculated for different load angles δ. Fig 4.12 shows the d-axis synchronous reactance X_{sd} versus rotor position α for the buried PM motor (PM4). Fig 4.12 also shows the variation of X_{sd} in relation to the stator slots and the phase sequences. The full performance results of this motor are discussed in Section 4.5.

4.3 Experimental method

Classical methods of determining the equivalent circuit parameters of a synchronous motor are not appropriate for PM excited synchronous motors. The usual methods of measuring the synchronous reactances of large and medium powered PM synchronous machines are by *the load test* [101], *the standstill frequency response test* [5, 29] and *the DC decay test* [70, 73, 112].

The problem with the load test is that there is a lack of uniqueness in specifying E_o and X_{sd} [73]. The analysis of the load conditions of the motor cannot adopt the value of the open-circuit voltage since for different loads the armature reaction will change the saturation level of the magnetic flux and thus change the induced voltage E_o.

Stationary tests, such as the standstill frequency response test and the DC decay test, have been given a large amount of attention over the last decade. This is due to the problems with doing load tests on large synchronous machines. The same cannot be said about small PM synchronous motors. The simplifications made in the standstill frequency response test were made for analysing large synchronous machines and are not appropriate for small synchronous machines. The DC decay test was also designed for large synchronous machines with the assumption that any error in matching the exterior resistance to the winding resistance is negligible. This is not true for small synchronous motors since the winding resistance is comparable with the leakage reactance in small synchronous motors.

A more direct method of measuring the synchronous reactances is thus required. An accurate method of measurement results from the phasor diagram Fig 3.1, which is a modified load test. From the phasor relationship of the synchronous machine the following set of equations can be written for a synchronous motor [85]:

$$V\cos(\delta) = E_o + I_1 X_{sd}\sin(\psi - \delta) + I_1 R_1 \cos(\psi - \delta) \tag{4.45}$$

$$V\sin(\delta) = I_1 X_{sq}\cos(\psi - \delta) - I_1 R_1 \sin(\psi - \delta) \tag{4.46}$$

The q-axis synchronous reactance can be found from eqn (4.46).

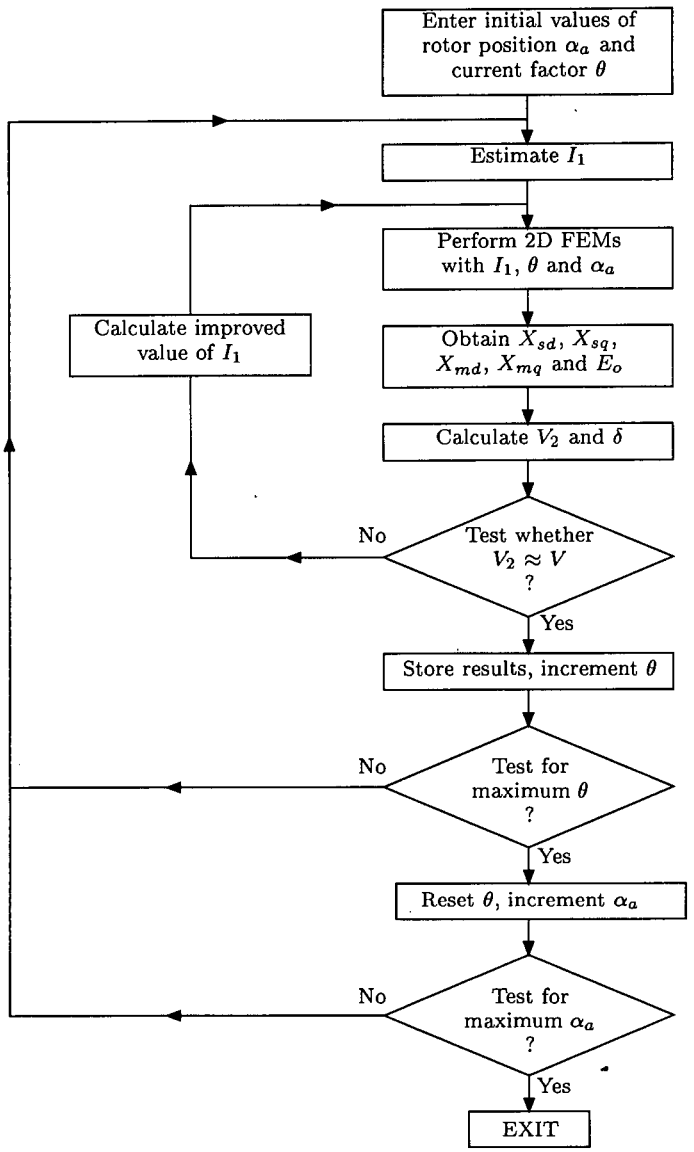

Figure 4.11: Block diagram of performance analysis using the finite element method

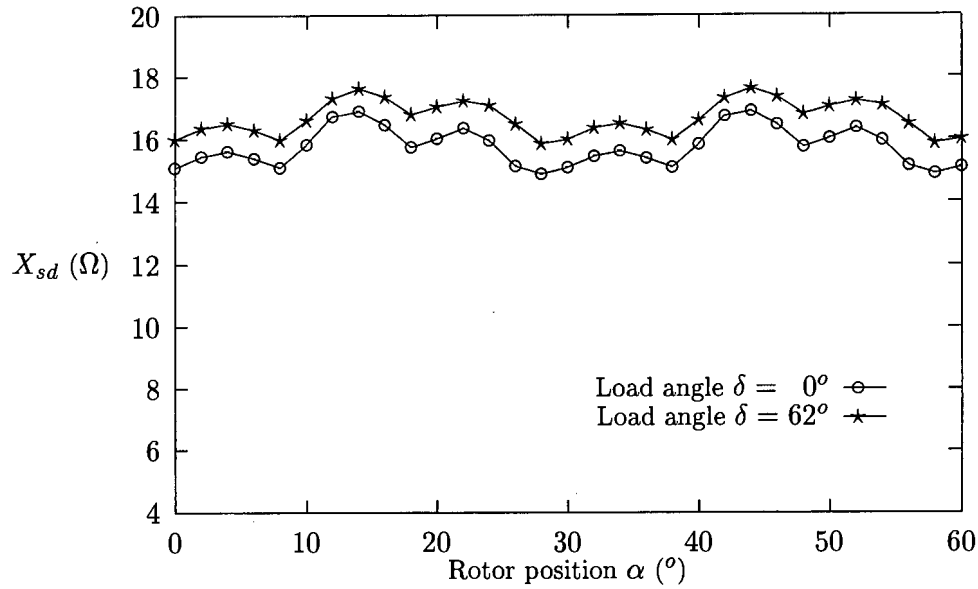

Figure 4.12: X_{sd} versus rotor position for different values of load angle for the buried PM motor (PM4)

$$X_{sq} = \frac{V\sin(\delta) + I_1 R_1 \cos(\psi - \delta)}{I_1 \cos(\psi - \delta)} \tag{4.47}$$

The d-axis synchronous reactance cannot be calculated directly from eqn (4.45) as E_o is not constant for a changing stator current I_1. Hence an additional equation to eqn (4.45) is needed to evaluate E_o and X_{sq}. Assuming constant synchronous reactance and voltage E_o for a small change in I_1 leads to:

$$V^{'}\cos(\delta^{'}) = E_o + I_1^{'} X_{sd}\sin(\psi^{'} - \delta^{'}) + I_1^{'} R_1 \cos(\psi^{'} - \delta^{'}) \tag{4.48}$$

where $I_1^{'} = I_1 + \Delta I$ in which $\Delta I \approx 0.05 I_1$.

From eqns (4.45) and (4.48) the d-axis synchronous reactances can be calculated as:

$$X_{sd} = \frac{V\cos(\delta) - V^{'}\cos(\delta^{'}) - R_1(I_1\cos(\psi - \delta) - I_1^{'}\cos(\psi^{'} - \delta^{'}))}{I_1\sin(\psi - \delta) - I_1^{'}\sin(\psi^{'} - \delta^{'})} \tag{4.49}$$

An extension of this method is to remove the use of ΔI. The method is sensitive to the magnitude of ΔI and to noise on the readings. The accuracy is thus effected by ΔI and a method which is independent of ΔI should be beneficial. Eqn (4.45) can be rewritten as:

$$V\cos(\delta) - I_1 R_1 \cos(\psi - \delta) \;=\; E_o + I_1 X_{sd}\sin(\psi - \delta)$$

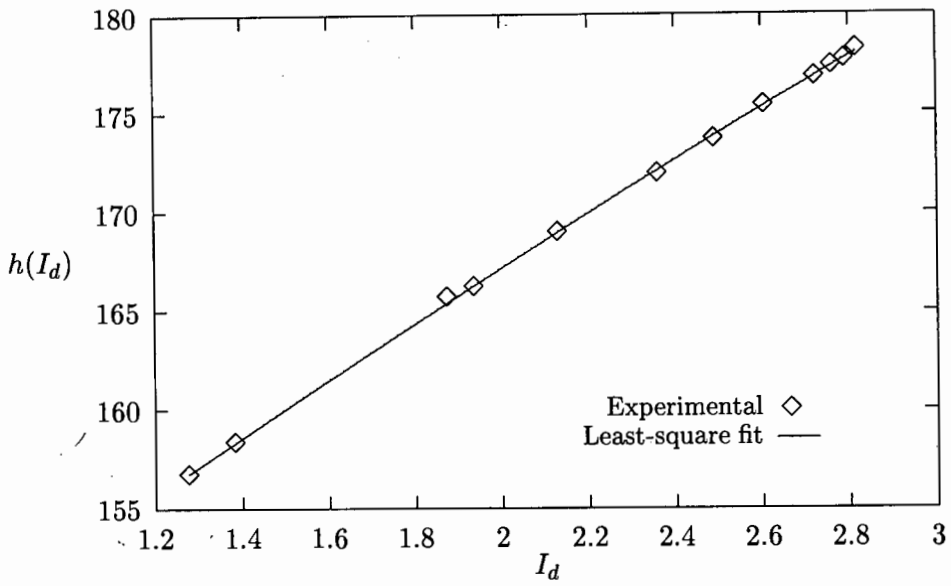

Figure 4.13: The function $h(I_d)$ versus I_d from measurements and least square fit

$$h(I_d) = f(I_d) + I_d g(I_d) \tag{4.50}$$

where $h(I_d) = V\cos(\delta) - I_1 R_1 \cos(\psi - \delta)$, $f(I_d) = E_o$ and $g(I_d) = X_{sd}\sin(\psi - \delta)$ are all functions of I_d. The function $h(I_d)$ can be plotted against I_d for the full range of readings, as shown in Fig 4.13. A best fit curve is found for this set of points using the least-squares method [54]. A function of the fourth order is found to be of sufficient order to represent the points of $h(I_d)$, so it can be written as:

$$h(I_d) = a_0 + a_1 I_d + a_2 I_d^2 + a_3 I_d^3 \tag{4.51}$$

where $a_{0\ldots3}$ are the coefficients of the function.

The partial derivative of eqn (4.50) with respect to I_d gives:

$$\begin{aligned} h'(I_d) &= f'(I_d) + I_d g'(I_d) + g(I_d) \\ h'(I_d) &\approx g(I_d) \end{aligned} \tag{4.52}$$

where $f'(I_d) \approx 0$ and $g'(I_d) \approx 0$ since it is assumed that there is no rapid change in the functions $f(I_d)$ and $g(I_d)$ due to a small change in I_d.

$$g(I_d) = a_1 + 2a_2 I_d + 3a_3 I_d^2 \tag{4.53}$$

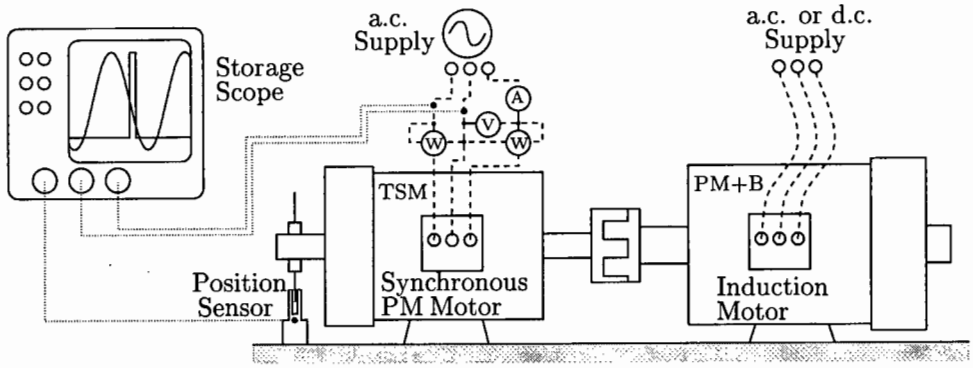

Figure 4.14: Laboratory set for measuring the load angle δ

For discrete values if I_d, the function $f(I_d)$ can be calculated by substituting in the values of $g(I_d)$ into eqn (4.50).

The measurement of the input voltage V, stator phase current I_1, armature winding resistance R_1 and input power P_{in} can be done using standard measuring techniques. The angle ψ is calculated as $\psi = \arccos(P_{in}/m_1 V I_1)$. The load angle δ should be measured using a position sensor and a storage oscilloscope.

The load angle is measured by calculating the angle difference between the position sensor's pulse and the input voltage peak. The machine set for doing these measurements is shown in Fig 4.14. The calibration of the rotor position sensor is needed since there is no obvious reference to determine the position of the d-axis, which is necessary for referencing the torque angle measurement. The calibration is done by running the synchronous motor at approximately synchronous speed from an external motor drive, in Fig 4.14 this is done using an induction motor which will later be used as the machine set brake. The open circuit voltage of the synchronous machine is displayed on the oscilloscope as well as the pulse from the position sensor. The peak open circuit voltage indicates the reference position of the q-axis from which the position of the d-axis can be deduced. The phase angle between this voltage peak and the centre of the position sensor's pulse indicates the phase shift (offset) δ_{off} of the position sensor from the d-axis.

The synchronous motor is operated under load conditions and measurements are taken. The measured phase shift δ_{meas} between the terminal voltage and the position sensor lead to the load angle:

$$\delta = \delta_{meas} - \delta_{off} \tag{4.54}$$

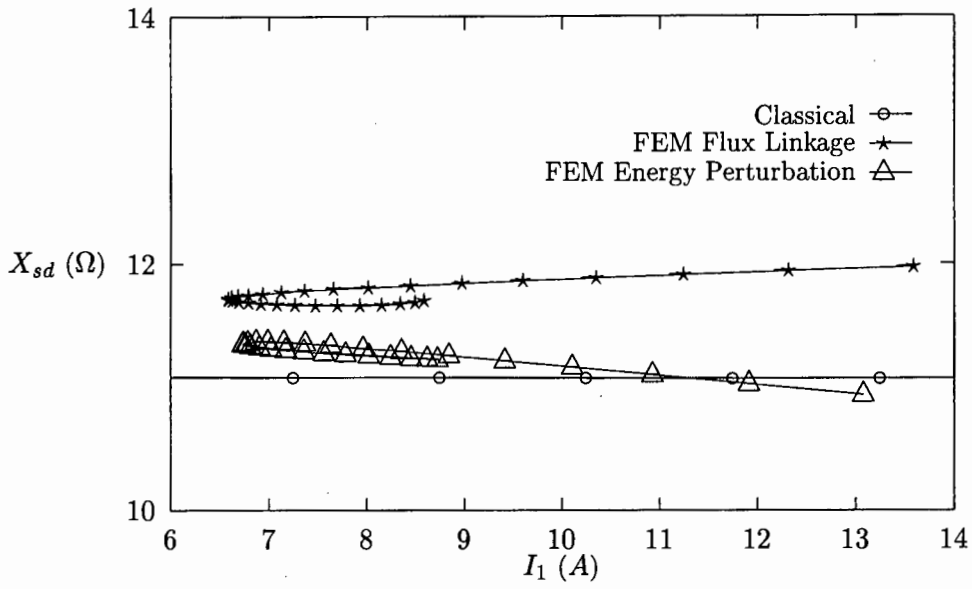

Figure 4.15: Synchronous reactances X_{sd} versus stator current at a constant terminal phase voltage of $220V$ for rotor design PM1 (inset PMs)

4.4 Comparison of reactances using analytical and finite element methods for PM1 and PM2

Calculations have been done on the synchronous motor models shown in Figs 2.2b and 2.2c, synchronous motor designs PM1 and PM2. Both motors use the same stator from a 1.5 kW induction motor, as described in Chapter 2. The dimensions of the stator are shown in Table 2.1.

The form factors, used in the analytical calculations, are calculated as for the inset type PM rotor and the surface mounted PM rotor, as described in Section 4.1, for PM1 and PM2 respectively. For PM1 the coefficient $c_g = 3.5975$ is > 1 as expected, and $k_{fd} = 1.299$ and $k_{fq} = 3.162$. The FEM calculations are done as described in Section 4.2.

Figs 4.15, 4.16, 4.17 and 4.18 show the d-axis and q-axis synchronous reactances for PM1 and PM2, respectively. The results show that there are fairly small differences in the calculated results between the analytical method and the two FEM methods. The analytical results for motor PM2 are more accurate than for PM1. This is since PM2 is easier to model than PM1 in the analytical method, as no form factor is needed. The results for the synchronous reactances shows a difference between the FEM flux linkage and FEM energy perturbation methods. The results from the energy perturbation method are always less than those from the flux linkage method.

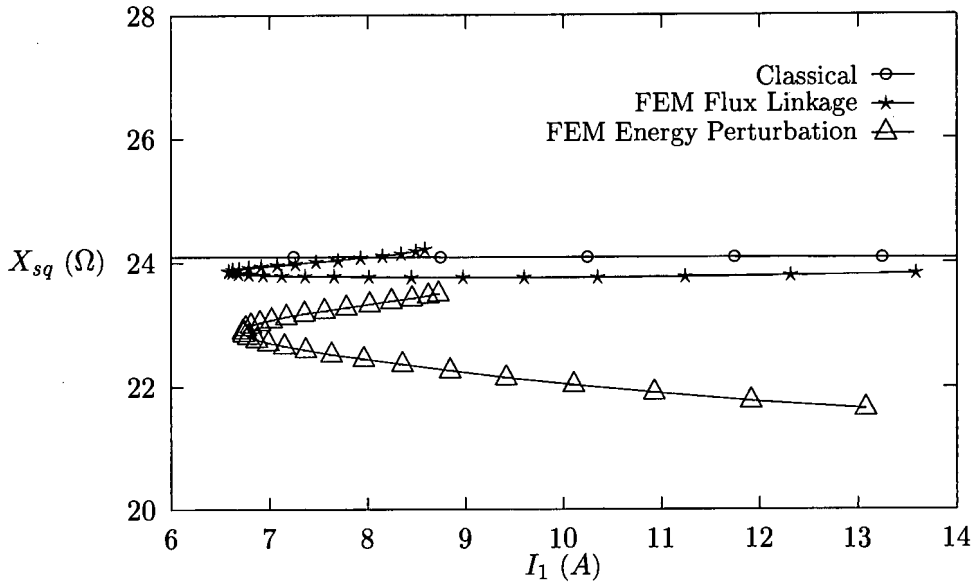

Figure 4.16: Synchronous reactances X_{sq} versus stator current at a constant terminal phase voltage of $220V$ for rotor design PM1 (inset PMs)

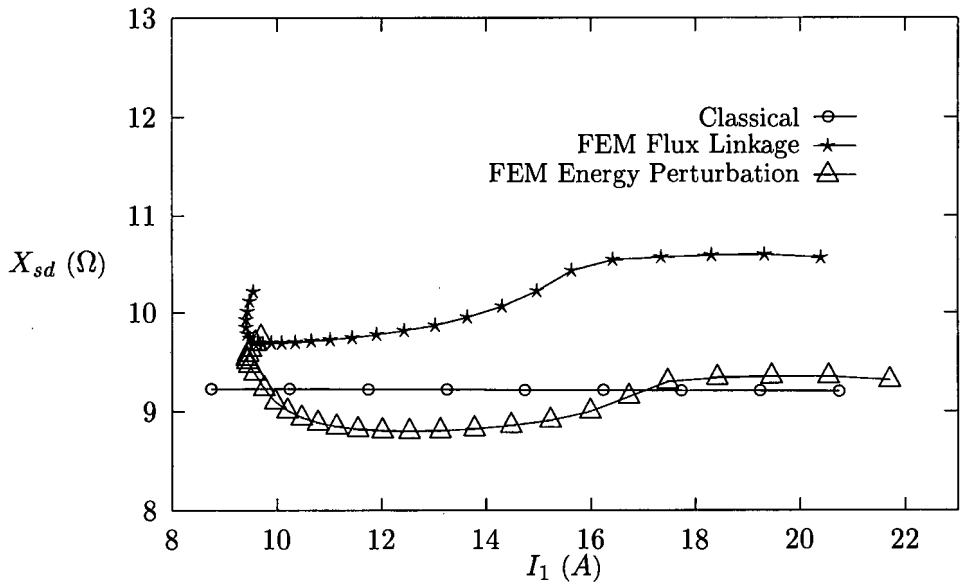

Figure 4.17: Synchronous reactances X_{sd} versus stator current at a constant terminal phase voltage of $220V$ for rotor design PM2 (surface PMs)

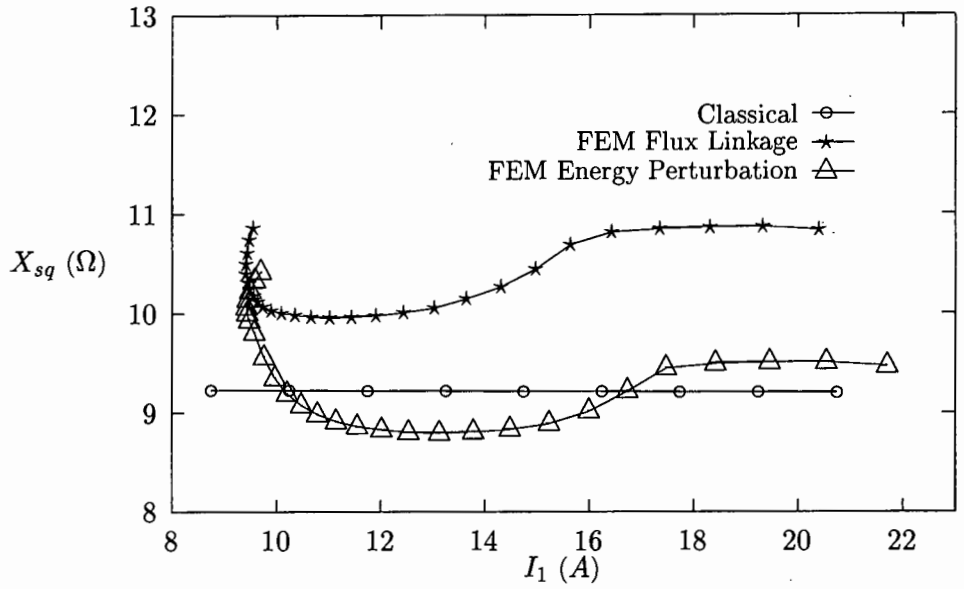

Figure 4.18: Synchronous reactances X_{sq} versus stator current at a constant terminal phase voltage of $220V$ for rotor design PM2 (surface PMs)

4.5 Comparison of results from analytical method, finite element method and experimental measurements for PM3 and PM4

The same stator has been used as for the designs PM1 and PM2 (Table 2.1). The rotor designs for the surface mounted PM motor with pole shoes (PM3) and the buried PM motor (PM4) are shown in Figs 2.2d and 2.3, respectively.

The analytical method uses form factor equations based on the rotor design. For the PM3 motor these factors can be derived on the basis of Fig 4.9a. The d-axis and q-axis form factors, for PM3, can thus be found using eqns (4.9, 4.14). The coefficient $c_g \approx (g + h_m)/(g + h_s + h_m) = 0.796$ which is < 1, as can be seen from Fig 4.9a. For the rotor of PM3 $\alpha = b_p/\tau = 45^o/90^0 = 0.5$, $k_{fd} = 0.963$ and $k_{fq} = 0.833$. The armature reactances are $X_{md} = 8.871\Omega$ and $X_{mq} = 7.676\Omega$ with $I_1 = 0$ A, and the leakage reactance $X_l = 1.982\Omega$, for $f = 50$ Hz. For $I_1 = 12$ A, the leakage reactance $X_l = 1.724\Omega$. The difference between the leakage reactance values at $I_1 = 0$ A and at 12 A is due to the magnetic saturation of the slot and differential leakage, as discussed in Section 3.1.1. The armature reactances X_{md} and X_{mq} are obtained with the magnetic saturation neglected i.e. $k_{sat} = 1$ in eqns (3.11,3.12). The synchronous reactances according to eqns (3.9,3.10) at $f = 50$ Hz, $V = 220$ V and $I_1 = 12$ A are $X_{sd} = 10.595\Omega$ and $X_{sq} = 9.400\Omega$.

The form factors for the buried PM motor are calculated using eqns (4.13,4.15) with

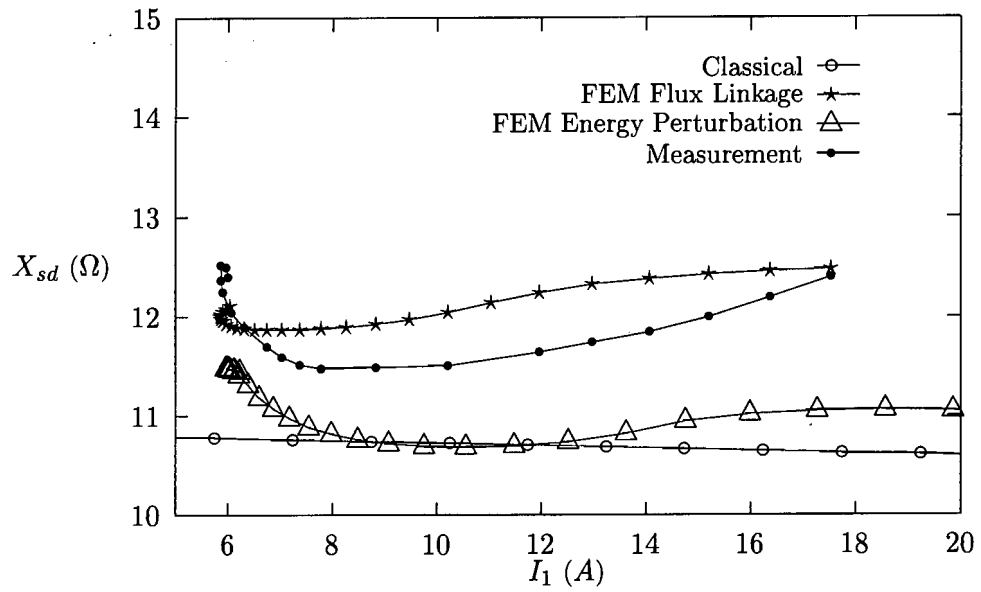

Figure 4.19: Synchronous reactances X_{sd} versus stator current at a constant terminal phase voltage of $220V$ for rotor design PM3 (surface PMs with pole shoes)

$\alpha = 0.870$, as illustrated in Fig 4.9b. The coefficients $k_{fd} = 0.924$ and $k_{fq} = 0.744$. The armature reactances are $X_{md} = 60.989\Omega$ and $X_{mq} = 49.079\Omega$ with $I_1 = 0$ A, and the leakage reactance $X_l = 2.252\Omega$, for $f = 50$ Hz. For $I_1 = 10$ A, the leakage reactance $X_l = 2.124\Omega$.

Figs 4.19, 4.20, 4.21 and 4.22 show the d-axis and q-axis reactances versus armature current I_1 and load angle δ, for motor PM3. It can be seen from these graphs that in the q-axis reactance the analytical approach has the greatest error in the calculation. The analytical results show $X_{md} > X_{mq}$ where as the measurements and the FEMs show $X_{md} < X_{mq}$. This is due to the complicated structure of the synchronous motors rotor and the large amount of q-axis flux that flows through the rotor pole shoe, which cannot be accounted for correctly in the one-dimensional analytical method. This high concentration of flux flowing through the mild steel pole shoe can be clearly seen in Fig 4.4. The analytical approach gives better results for the d-axis reactance, but still not as accurate as the FEMs.

The results for open circuit EMF (E_o) are shown in Figs 4.23 and 4.24, for PM3. The analytical method tends to over estimate the EMF. This is due to the fact that the armature reaction and material saturation have been neglected in these calculations. Figs 4.23 and 4.24 also show the increase in E_o with armature current due to the shift in I_d from a positive magnetising component to a negative demagnetising component. This negative I_d makes the the flux path for the magnets less saturated, thus the increase.

Figs 4.25, 4.26, 4.27 and 4.28 show the d-axis and q-axis reactances versus armature current I_1 and load angle δ, for motor PM4. It can be seen from these graphs that in the

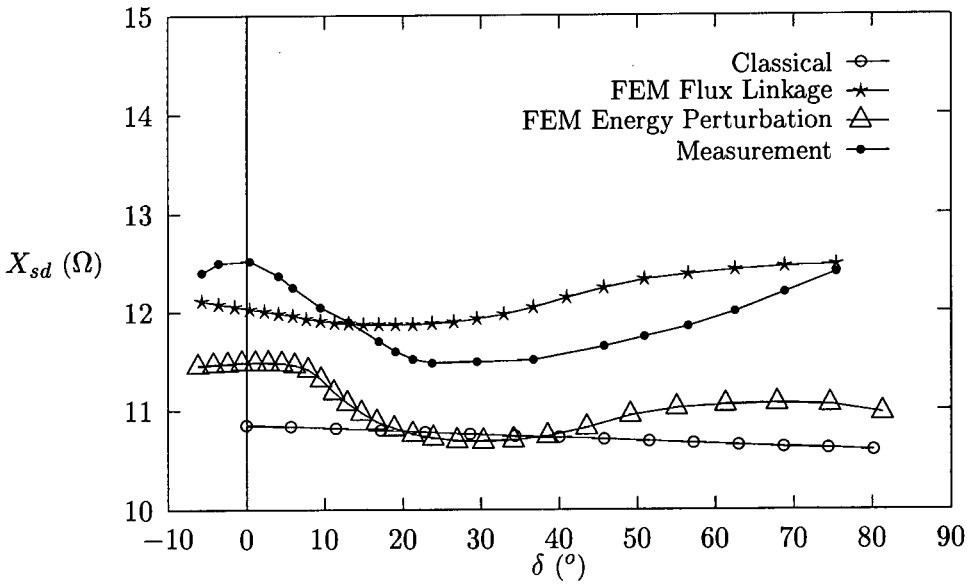

Figure 4.20: Synchronous reactances X_{sd} versus the torque load angle δ at a constant terminal phase voltage of $220V$ for rotor design PM3 (surface PMs with pole shoes)

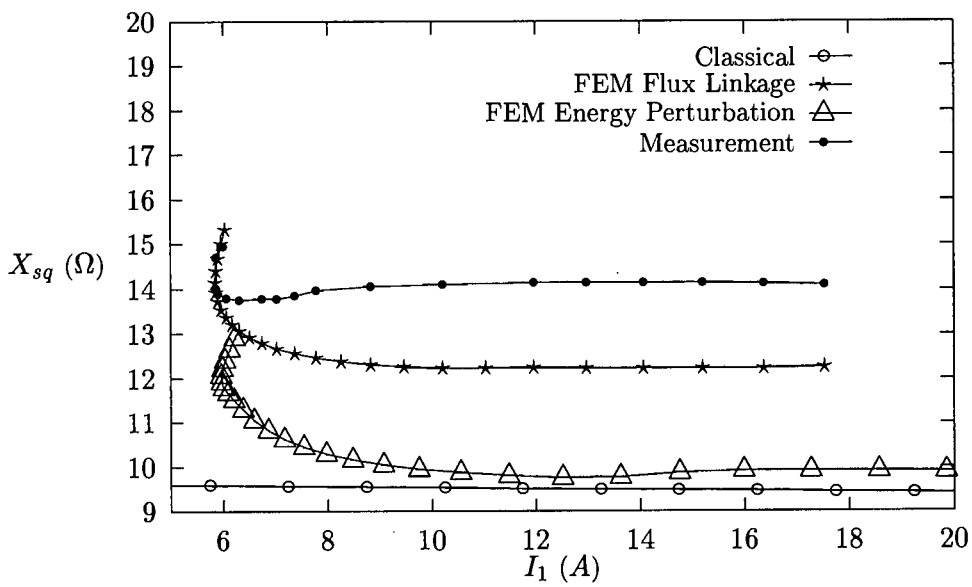

Figure 4.21: Synchronous reactances X_{sq} versus stator current at a constant terminal phase voltage of $220V$ for rotor design PM3 (surface PMs with pole shoes)

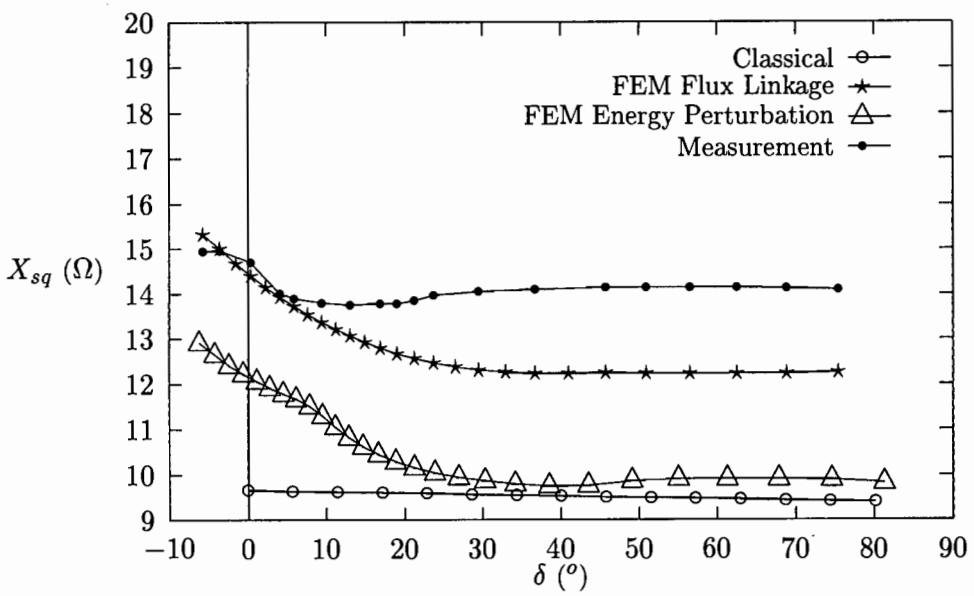

Figure 4.22: Synchronous reactances X_{sq} versus the torque load angle δ at a constant terminal phase voltage of $220V$ for rotor design PM3 (surface PMs with pole shoes)

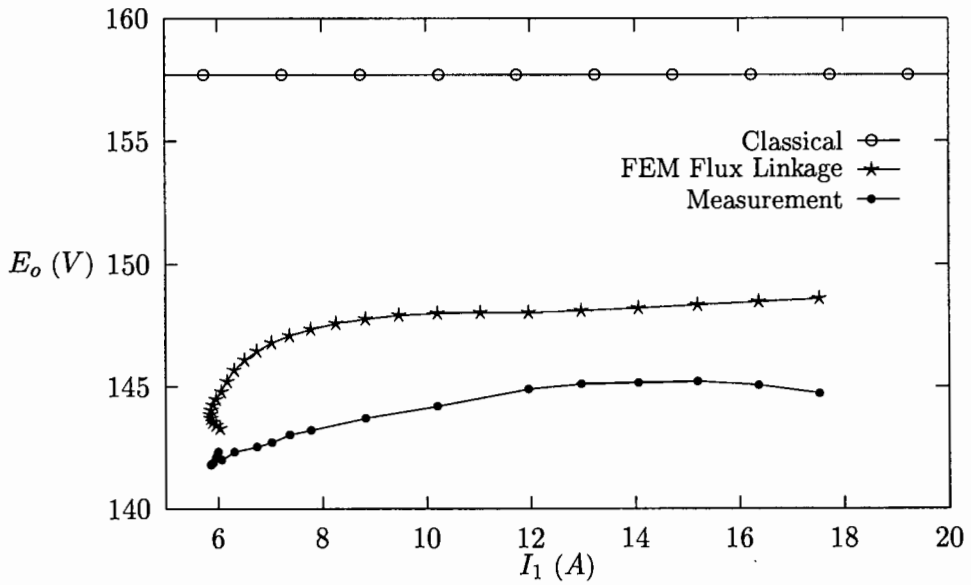

Figure 4.23: Open circuit EMF E_o versus stator current at a constant terminal phase voltage of $220V$ for rotor design PM3 (surface PMs with pole shoes)

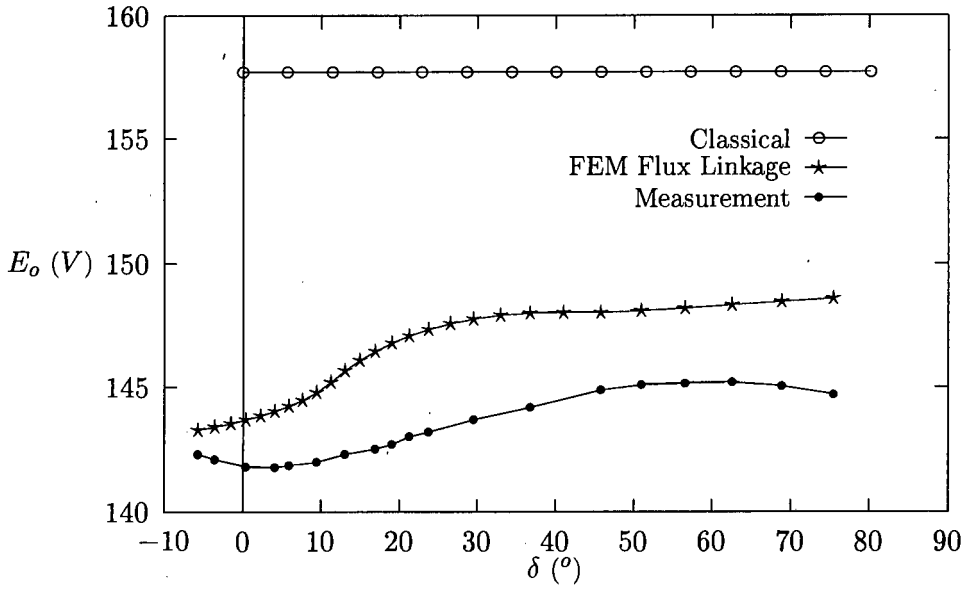

Figure 4.24: Open circuit EMF E_o versus the torque load angle δ at a constant terminal phase voltage of $220V$ for rotor design PM3 (surface PMs with pole shoes)

d-axis and q-axis reactances the analytical approach has the greatest error in the calculation. This is mainly due to the structure of the buried PM rotor not being correctly modelled by the one-dimensional analytical approach. The form factor does not take into account the increased reluctance due to the PMs in the calculation of X_{md}.

The results for open circuit EMF (E_o) are shown in Figs 4.29 and 4.30, for PM4. The analytical method tends to over estimate the EMF for the same reasons as discussed for PM3. The induced EMF E_o also increases with increase in armature current, as for PM3.

The interaction between the d-axis and q-axis stator current are impossible to calculate using analytical methods. This interaction is seen in the hook like curves of the synchronous reactances versus stator currents (Figs 4.19, 4.21, 4.25 and 4.27). Figs 4.20 and 4.26 show the d-axis reactances versus load angle δ, and Figs 4.22 and 4.28 show the q-axis reactances versus load angle δ for PM3 and PM4, respectively. The d-axis reactances do not decrease with an increase in δ, as would be expected, but first decrease and then increases with an increase in δ. This is due to the complex relationship between the d-axis reactance and the q-axis reactances in both motors.

The calculation of the leakage reactances, using the FEM, was done using the difference between the synchronous reactance and the magnetising reactance, as shown in eqns (4.42). This gives two separate components of leakage reactance for the two axes. Figs 4.31 and 4.32 shows a small difference between the d-axis and q-axis leakage reactances from the finite element method. This is due to the effects of saturation on the two axes being different at

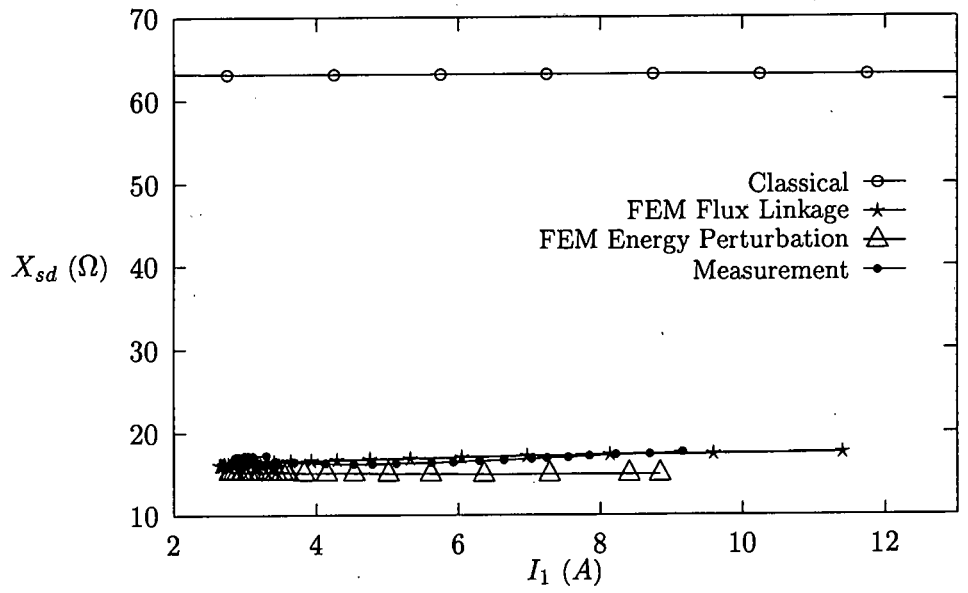

Figure 4.25: Synchronous reactances X_{sd} versus stator current at a constant terminal phase voltage of $220V$ for rotor design PM4 (buried PMs)

different armature current values or load angles. Saturation affects the two leakage components separately i.e. in Fig 4.31 the leakage reactance in the d-axis is increasing while it is decreasing in the q-axis for an increase in stator current. The analytical approach gives similar results as those calculated from the FEM.

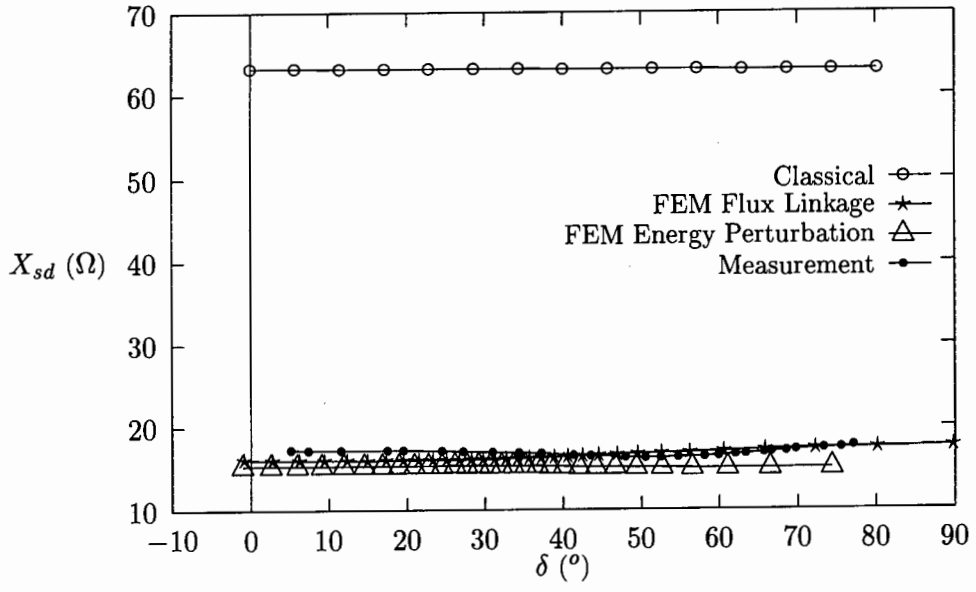

Figure 4.26: Synchronous reactances X_{sd} versus the torque load angle δ at a constant terminal phase voltage of $220V$ for rotor design PM4 (buried PMs)

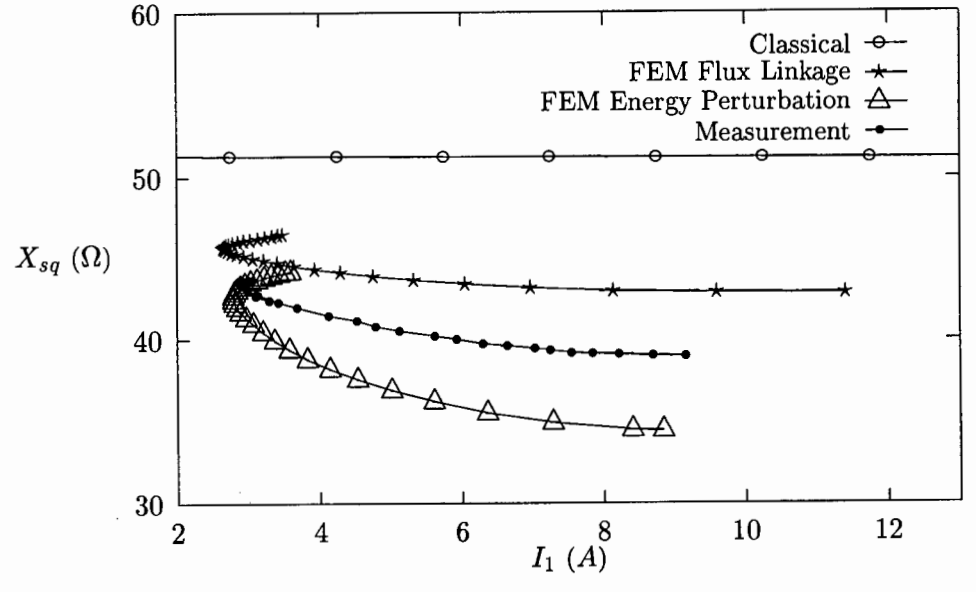

Figure 4.27: Synchronous reactances X_{sq} versus stator current at a constant terminal phase voltage of $220V$ for rotor design PM4 (buried PMs)

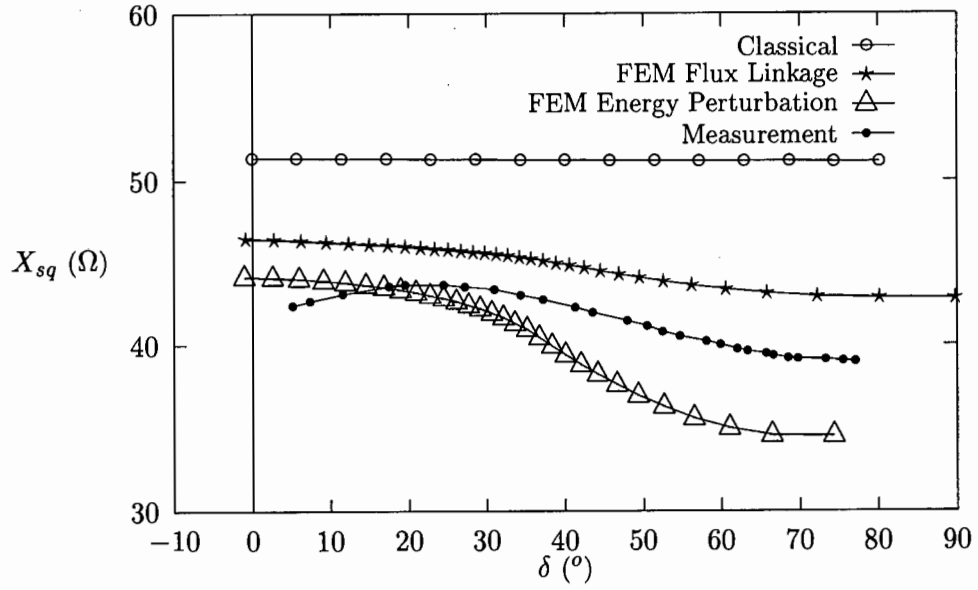

Figure 4.28: Synchronous reactances X_{sq} versus the torque load angle δ at a constant terminal phase voltage of $220V$ for rotor design PM4 (buried PMs)

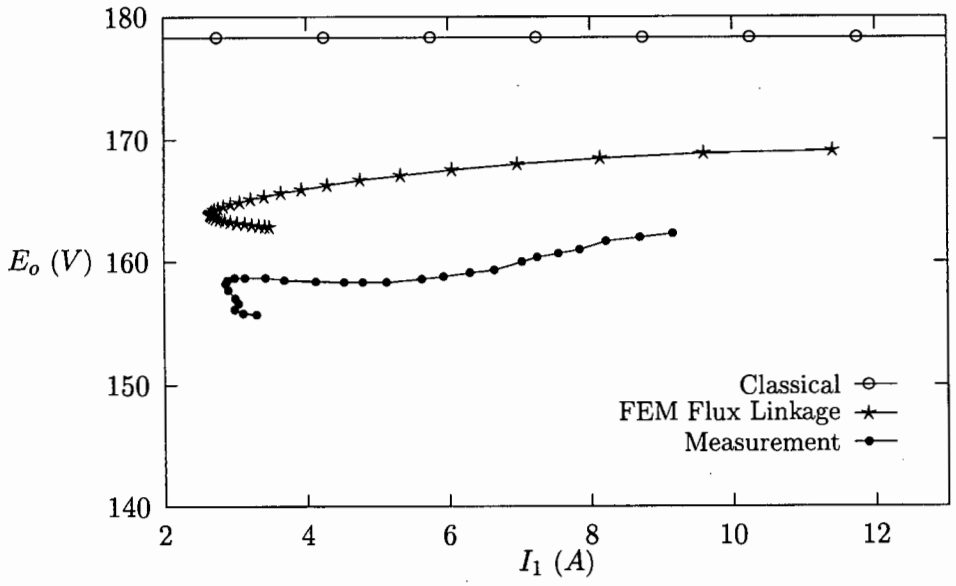

Figure 4.29: Open circuit EMF E_o versus stator current at a constant terminal phase voltage of $220V$ for rotor design PM4 (buried PMs)

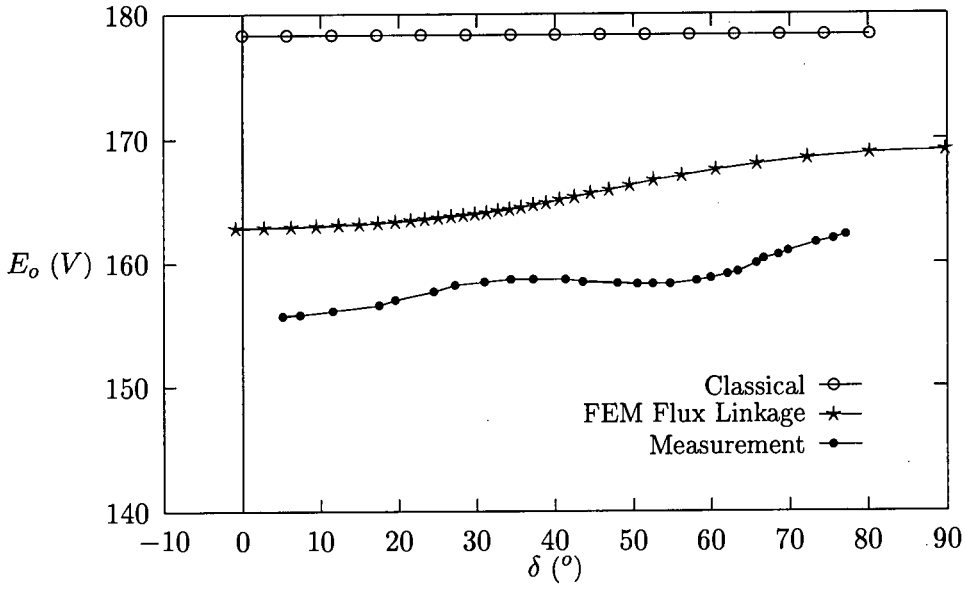

Figure 4.30: Open circuit EMF E_o versus the torque load angle δ at a constant terminal phase voltage of $220V$ for rotor design PM4 (buried PMs)

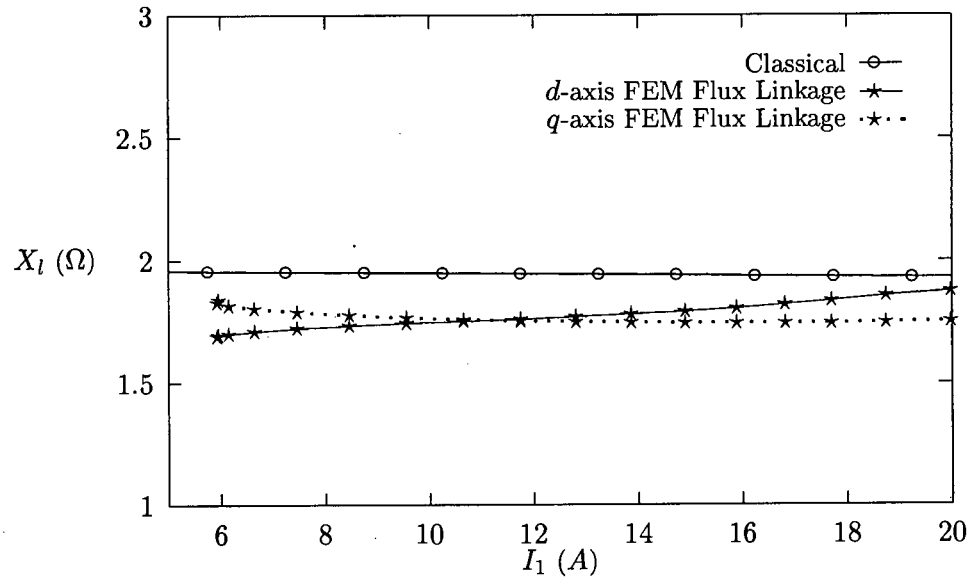

Figure 4.31: Leakage reactances X_l versus stator current at a constant terminal phase voltage of $220V$ for rotor design PM3 (surface PMs with pole shoes)

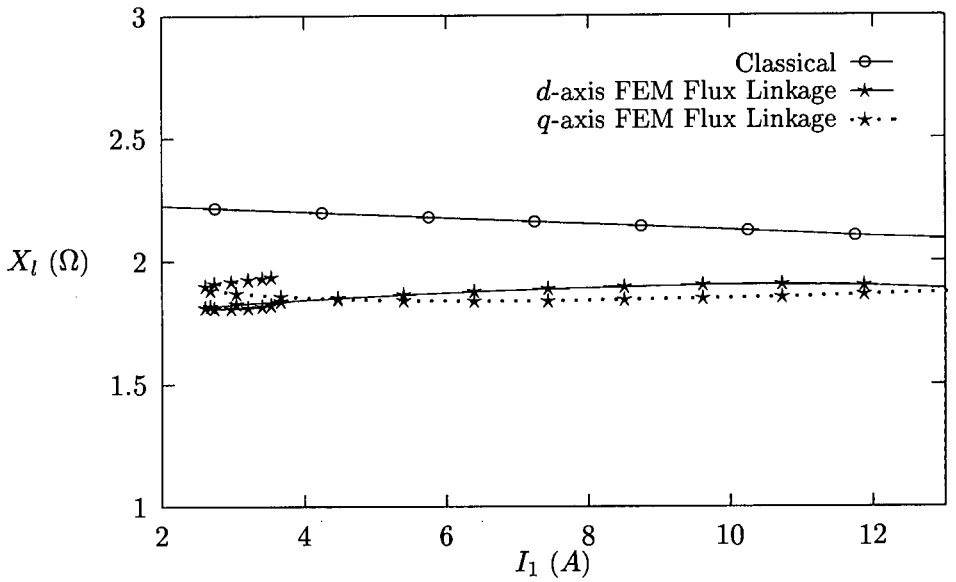

Figure 4.32: Leakage reactances X_l versus stator current at a constant terminal phase voltage of $220V$ for rotor design PM4 (buried PMs)

Chapter 5

Brushless Universal motor

5.1 Operation of a Brushless Universal motor

The universal motor is a motor that combines the ease of starting of the brushless DC motor with the high efficiency and smooth torque production of the synchronous motor. The universal motor thus has two modes of operation. The one being a DC mode with position feedback control and the other being AC synchronous mode with no feedback.

The brushless DC mode feeds a square-wave excitation of 120^o per phase from an inverter. This results in approximately a square-wave current waveform per phase. The position sensors' feedback ensures that the motor operates at the maximum speed for the particular voltage and load level. This mode is used at high torque levels where a reduced speed is needed, above the synchronous stability point or to ensure that the maximum power limit of the motor is not exceeded. This mode is also used for starting and speeding the motor up to synchronous speed.

The brushless AC synchronous mode feeds a sinewave input voltage to the motor created by a pulse-width-modulation (PWM) control sequence. The synchronous mode operates at constant speed over a range of torques up to its stability point. No feedback is required for this constant speed region, although the load angle is monitored for switching into DC mode.

Fig 5.1 shows the AC and DC modes of operation. The motor starts-up in DC mode and accelerates until synchronous speed is reached at which time it switches to synchronous mode. As the motor reaches its maximum power rating the motor switches from synchronous to DC modes. At extremely high torque levels current limiting is introduced, in the DC mode, to prevent damage to the stator windings and permanent magnets.

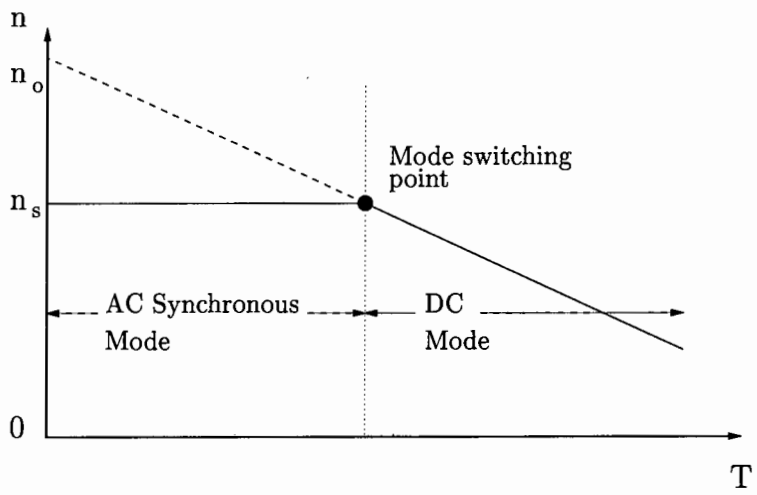

Figure 5.1: Speed - torque characteristics of a universal motor

5.2 Comparative analysis of an PM AC synchronous motor and a PM brushless DC motor

The design of a universal motor drive systems requires a PM brushless DC motor that can perform optimally in both synchronous and DC operating modes. A comparative analysis of the two modes is thus needed.

5.2.1 Synchronous Mode

The ideal synchronous motor has the following characteristics:

(a) the input stator current is sinusoidal;

(b) the stator windings are distributed sinusoidally through the stator;

(c) the airgap magnetic flux density distribution is sinusoidal.

In the practical synchronous motor none of the above assumption are completely realised. The stator windings are in slots and thus the winding factor k_{w1} is used to obtain the fundamental winding distribution, the airgap magnetic flux density is more trapezoidal in shape than sinusoidal and the stator input current is not purely sinusoidal when driven from a voltage source PWM inverter.

The RMS phase EMF for a three phase synchronous motor is:

$$E_o = \frac{1}{\sqrt{2}} \frac{p}{a} k_{w1} N_1 \Phi_m \omega_r \tag{5.1}$$

where $\omega_r = \omega/p$ is the mechanical rotational speed (rad/s). Eqn (5.1) can also be written in terms of the maximum flux density as shown in Chapter 3. The line-to-line EMF is $E_{l-l} = \sqrt{3}E_o$ and the RMS electromagnetic torque can then be written as:

$$T_e = \frac{3}{\sqrt{2}}\frac{p}{a}k_{w1}N_1\Phi_m I_1 \qquad \text{or} \qquad T_e = \frac{3}{\sqrt{2}}\frac{1}{a}k_{w1}N_1 D_{2out} l B_{mg} I_1 \tag{5.2}$$

5.2.2 DC Mode

The ideal DC motor has the following characteristics:

(a) the input stator current is rectangular;

(b) the stator windings are full pitched and concentrated;

(c) the airgap magnetic flux density distribution is rectangular.

In the practical brushless DC motor the stator windings are spread out in more than one stator slot and are not concentrated. The airgap magnetic flux density is also not rectangular in shape, this is due to the fringing on the sides of the PMs and due to the less than a full pitch magnet width. The flat top current waveforms are thus more trapezoidal in shape, although this depends on the pole-arc to pole-pitch ratio. The torque produced is not constant and the torque ripple is a function of the current waveform.

The peak phase EMF for a PM brushless DC motor running off a full bridge inverter, firing each phase for only 120^o, is:

$$e_o = \frac{4}{\pi}\frac{p}{a}\frac{k_w N_1 \Phi_g}{\alpha}\omega_r \tag{5.3}$$

where k_w is the winding factor which accounts for the spread of the stator windings, Φ_g is the magnetic flux per pole in the airgap which should be seen as being constant for the 120^o cycle of each phase, and α is the pole-arc to pole-pitch ratio reducing the effective airgap flux density. The EMF for a PM brushless DC motor, in eqn (5.3), can also be written in terms of the airgap flux density as:

$$e_o = \frac{1}{a}k_w N_1 D_{2out} l B_{mg} \omega_r \tag{5.4}$$

The line-to-line EMF is $e_{l-l} = 2e_o$, due to the 120^o commutation sequence. The total electromagnetic torque is then:

$$T_e = \frac{4}{\pi}\frac{p}{a}\frac{k_w N_1 \Phi_g}{\alpha} i \qquad \text{or} \qquad T_e = \frac{2}{a}k_w N_1 D_{2out} l B_{mg} i \tag{5.5}$$

where i is the constant current that flows through each phase for its 120^o of commutation. The RMS current flowing through each phase is thus $I = \sqrt{\frac{2}{3}}i$.

5.2.3 Torque per Ampere for synchronous and DC operating modes

A comparison of the torque per ampere ratio's (TR) for the two modes of operation is done based on the electromagnetic torque T_e, in eqns (5.2) and (5.5). If it is assumed that the fundamental rotor magnetic flux Φ_m during sinusoidal operation is equal to the magnetic flux per pole Φ_g during DC operation, then the ratio of the DC to AC torque per ampere ratio can be written as:

$$TR_r = \frac{TR_{DC}}{TR_{AC}} = \frac{T_e/I\ (DC)}{T_e/I_1\ (AC)} = \frac{\sqrt{\frac{3}{2}}(4k_w)/(\pi\alpha)}{\frac{3}{\sqrt{2}}k_{w1}} \tag{5.6}$$

which can be simplified to $TR_r = 0.7351/\alpha$ with the assumption that $k_{w1} = k_w$. The pole-arc to pole-pitch ratio α can vary from 1 for a full pitched pole face to 0.666 for a 120^o pole-arc. This means that the ratio of the DC to AC torque per ampere ratio can be $TR_r = 0.7351 \ldots 1.1026$ depending on α.

When the assumption is made that the airgap magnetic flux densities are equivalent, the ratio changes to:

$$TR_r = \frac{2\sqrt{\frac{3}{2}}}{\frac{3}{\sqrt{2}}} = 1.1547 \tag{5.7}$$

These ratios have shown that the performance criteria are similar for both operating modes. Many authors have discussed this idea and generally concluded that the torque per ampere of the two modes are almost equal [74, 80].

Since the output power of the sinusoidal and DC modes are considered identical the optimisation of both modes can be achieved by analysing just one mode, within reason.

5.3 Solid State Inverter

The drive system consists of a 3-phase full bridge diode rectifier, a 3-phase insulated-gate-bipolar-transistor (IGBT) inverter, shaft position sensors, current transformer, sinusoidal PWM controller, square-wave controller and a mode selector (Fig 5.2). A simplified schematic representation of the inverter circuit for voltage-source configuration is shown in Fig 5.3.

The inverter topology used for both sinusoidal and DC square-wave operation is identical. The switching sequences are entirely responsible for distinguishing between the two operating modes.

5.3.1 Sinusoidal PWM switching

The synchronous operation of the motor is done using a sinusoidal PWM switching topology. A synchronous regular sampled PWM is used to ensure the maximum reduction in harmonics,

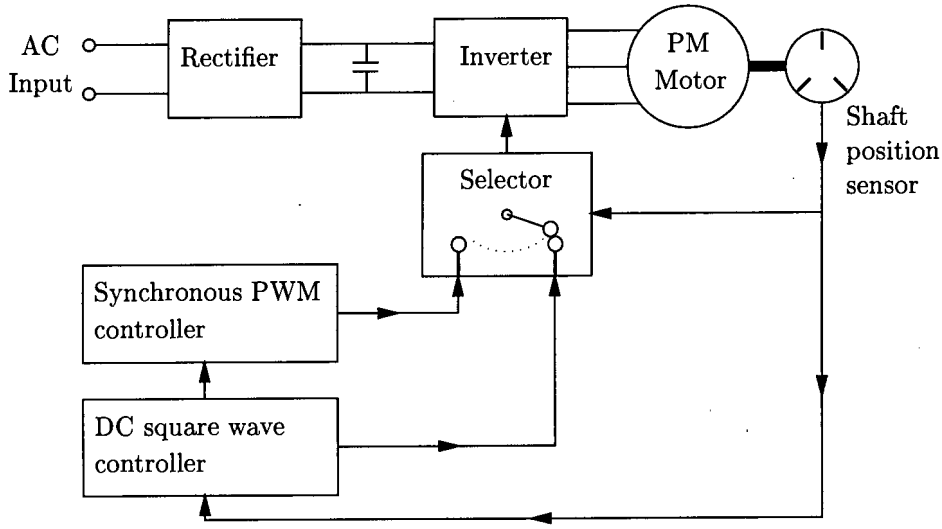

Figure 5.2: Universal motor block diagram

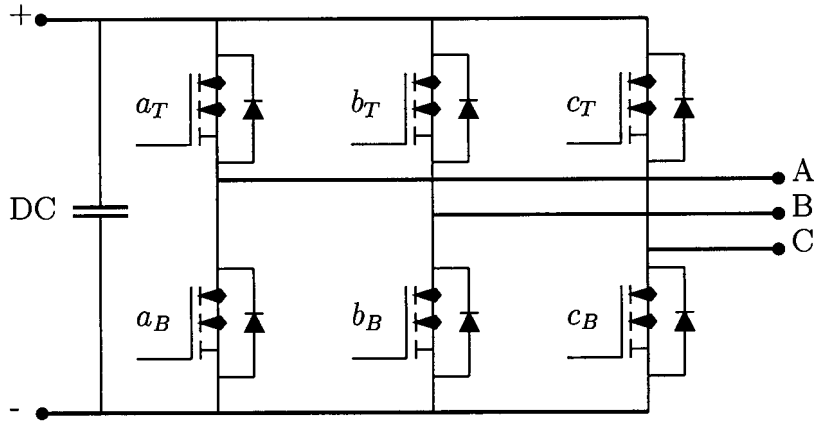

Figure 5.3: Schematic of IGBT inverter

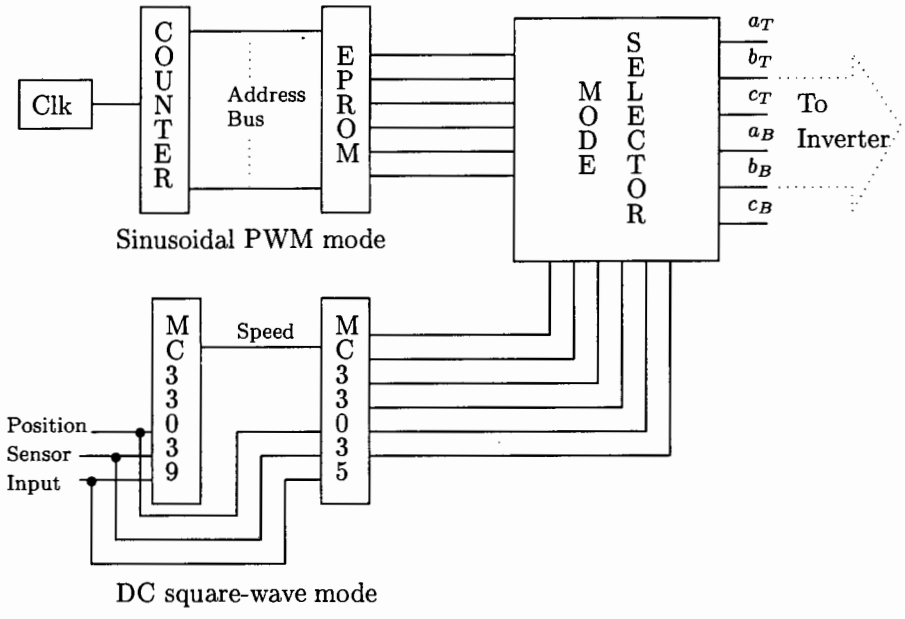

Figure 5.4: Block diagram showing the link between sinusoidal PWM and DC modes

as discussed in [16, 17]. The frequency modulation ratio m_f is an odd integer and a multiple of three, which also cancels out dominant harmonics [77].

The sinusoidal PWM switching consists of the constant frequency clock, a set of counters and an erasable programmable read-only memory (EPROM). A simplified schematic is shown in Fig 5.4, and a more detailed schematic is shown in Appendix C. Six bits of each byte of data from the EPROM drive the six transistors of the inverter. Fig 5.4 shows that the individual data lines from the EPROM each represent a transistor. The clock frequency determines the synchronous speed which is fixed at a synchronous speed of 50 Hz.

5.3.2 DC square-wave switching

The DC square-wave controller is designed around the monolithic brushless DC motor controller integrated circuit MC33035, from Motorola. The MC33035 chip is a second generation controller with all the necessary features, such as current limiting, speed control, forward and reverse direction and dynamic braking. This controller uses 120^o firing on each phase.

The speed control function allows for a steady rise in speed from start-up with the added benefit of having current limiting at low speeds. This ensures that the motor's stator windings do not overheat or that the magnets do not get demagnetised due to high starting currents. The acceleration of the motor can also be kept at the maximum due to the drive's switching frequency being determined directly from the position sensors.

The current is regulated in each of the three stator phases. A single current sensor placed

in the DC link is sufficient, since the bus current flows through the two active phases connected in series at each instant in time. The bottom driver of each phase is used for current limiting.

The speed is controlled using a square-wave PWM, which is built into the MC33035 chip. The square-wave PWM reduces the average voltage across the windings and thus is able to control the motor's speed from standstill up to full speed.

The DC controller is used in three phase closed loop control with the rotor position and speed feedback. The speed is obtained from the speed control adapter integrated circuit MC33039 specifically designed for use with the MC33035 Motorola chip. The MC33039 chip determines the speed economically since it only uses the three position sensor outputs.

5.3.3 Mode switching control circuit

The most frequently used mode of operation of a PM brushless universal motor is the synchronous mode. This is since it is the most efficient operating mode [51] and this type of motor would generally be used in constant speed applications where loads exceeding the synchronous stability limit or maximum power limit would be for short periods of time only. In applications, such as conveyor belts, a sudden increase in load is possible which would either stall or overrate the motor. In this type of situation a reduced speed mode is better than no movement at all or destroying the stator windings and demagnetising the PM. The DC mode thus becomes essential until the load is reduced.

The aim of mode switching is to ensure that the motor operates continuously under all types of load conditions and switches between the two modes smoothly and automatically. The motor operates in the more efficient synchronous mode, at a constant speed, whenever possible. Fig 5.5 shows a flow chart representation of the switching modes. Different criteria are used when switching from synchronous mode to DC mode than when switching from DC mode to synchronous mode. A simplified schematic of the mode switching is shown in Fig 5.4, and a more detailed schematic of the mode switching control and mode switching logic are shown in Appendix C.

The start-up mode is actually the DC mode with the added use of the MC33035 chip's speed control. A constant slope speed ramp is used to ensure smooth acceleration of the motor and load. The motor's speed is increased until the synchronous speed is reached, at which time it is switched to synchronous mode. If the motor is not able to reach synchronous speed the motor remains in DC mode indefinitely. When switching from DC mode to synchronous mode the sinusoidal PWM has to be synchronised with the rotor's position. This ensures that the phase angle between the inverter and motor are approximately zero at the time of synchronising.

The switching from synchronous mode to DC mode is done when the load angle reaches the maximum power limit of the motor. This load angle is set below the synchronous stability angle of the motor.

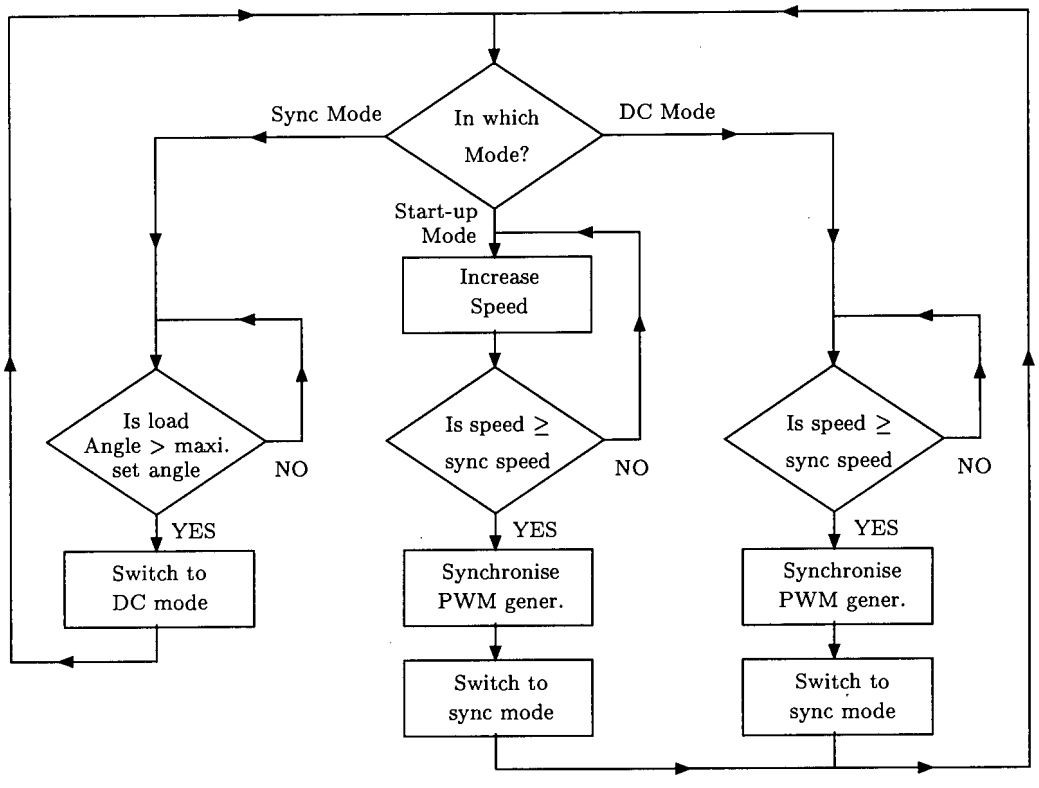

Figure 5.5: Flow chart of mode switching logic

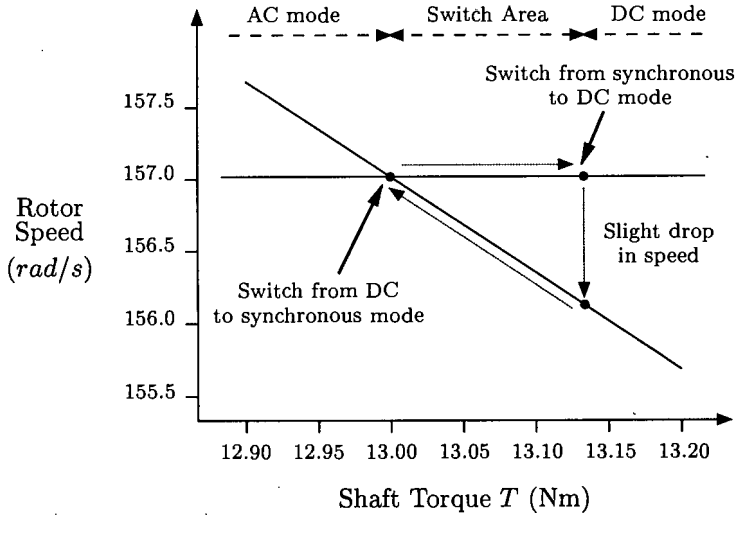

Figure 5.6: Speed - torque characteristics at switching point

Table 5.1: Comparison of RMS voltages for different switching modes

Switching Mode	m_a	V_{RMS}/V_{DC} Ratio
Square-wave		0.7070
Sinusoidal PWM	1	0.6124
	1.2	0.6781
	1.4	0.7131
	1.6	0.7361

In an attempt to simplify the mode switching circuitry, the point of switching from synchronous to DC modes is not at the intersection of the speed-torque characteristics of the two operating modes. Instead the switching is done at a slightly higher load angle (torque) and thus the motor experiences a drop in speed when moving to DC operation, as is illustrated in Fig 5.6. This short transient is not considered a problem since the DC mode uses position feedback. The switching back to synchronous mode is done at synchronous speed. This forms a hysteresis loop which drastically reduces the complexity of the switching circuitry.

5.3.4 Matching switching point

For a smooth transition from DC to synchronous mode it has been found that the stator voltage in the synchronous mode has to be increased. This ensures at the RMS current levels at the point of switching, from DC to synchronous modes, are similar. To ensure that this is possible the RMS voltages of the two modes should be approximately equal. Section 5.2 showed that this would be necessary since the torque per ampere ratios (TR) are approximately equal for the two operating modes.

The amplitude modulation ratio m_a, for the synchronous mode, is not kept in the linear region ($m_a <= 1$), since the voltage has to be increased to match the DC mode's RSM voltage. This increased voltage, due to over-modulation ($m_a > 1$), is to ensure that the synchronous motor can instantaneously produce enough torque to match the DC mode's torque at the time of switching. Table 5.1 shows the RMS voltage V_{RSM} over DC bus voltage V_{DC} for a 120^o square-wave and sinusoidal PWMs with different m_a values. The bus voltage is kept at a constant voltage of $V_{DC} = 513$V. The amplitude modulation ratio is thus set to $m_a = 1.4$ to ensure a stable transition from DC to AC mode.

The effect of increasing m_a on the harmonic content of the stator current has been considered. A significant increase in the number of harmonics would lead to greater core losses and thus reduced efficiency. Fig 5.7 shows the normalised current waveforms for sinusoidal PWM with $m_a = 1$ and $m_a = 1.4$, and DC square-wave operation. Table 5.2 shows the

Table 5.2: Harmonics content of the normalised stator current i/I_{RSM} for synchronous PWM and DC modes

Harmonic Order	Synchronous PWM Mode		DC Mode
	$m_a = 1.0$	$m_a = 1.4$	
1	1.390555	1.400439	0.636296
3	0.000837	0.014635	0.002862
5	0.003796	0.001742	0.058675
7	0.004256	0.004923	0.003605
9	0.059544	0.025116	0.130941
11	0.001461	0.000324	0.002228
13	0.013911	0.011294	0.071291
15	0.010554	0.011123	0.003705
17	0.001028	0.000666	0.048035
19	0.010505	0.013208	0.002000
21	0.024935	0.024186	0.064753
23	0.001371	0.002209	0.003572
25	0.027361	0.022298	0.015602
27	0.023472	0.019652	0.002921
29	0.002435	0.001637	0.035255
31	0.025629	0.020801	0.000670
33	0.048451	0.028085	0.014346

corresponding frequency magnitude spectrum for the three current waveforms. From Table 5.2 it is clear that there is no significant increase in harmonic content when m_a is increased from 1 to 1.4. The harmonic content of the current waveform for DC square-wave operation, however, shows significantly more harmonics than the two PWM waves. The sinusoidal PWM mode with $m_a = 1.4$ is expected to be a more efficient mode of operation than the DC mode.

5.4 Practical model

Fig 5.8 shows the motor used in this research into universal motor drives. The motor has a model D90L frame from GEC South Africa. The motor used in this universal motor drive is the buried PM motor (PM4) described in Fig 2.3, which uses the stator as shown in Table 2.1. The fan casing has been extended to accommodate the optical position sensors. Fig 5.9 shows a end view of the motor with the fan casing and fan removed. The simple, cost effective position sensor design is shown. The holder and indicator disc of the position sensor are made out of PVC.

The IGBT switches used in the inverter drive are shown in Fig 5.10. These switches are mounted on a large heat sink for prototyping purposes. Fig 5.10 also shows the Semikron isolation drivers used to drive the IGBTs. It is foreseen that a commercial version of this

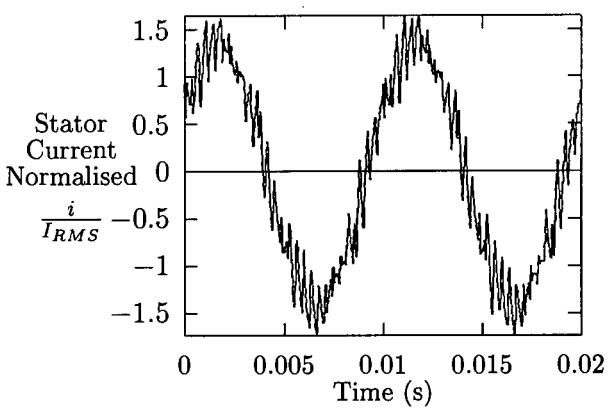

(a) Sinusoidal PWM ($m_a = 1.0$) ($I_{RSM} = 2.66$ A)

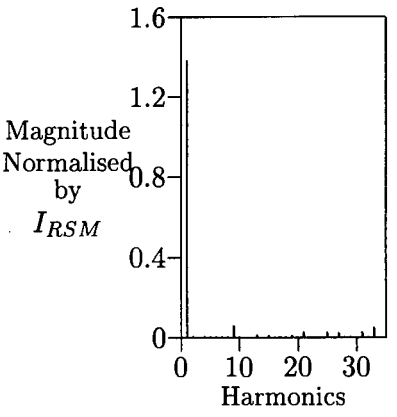

(b) ($m_a = 1.0$)

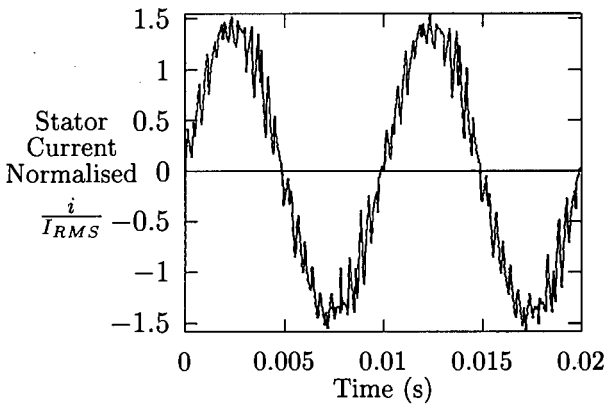

(c) Sinusoidal PWM ($m_a = 1.4$) ($I_{RSM} = 2.73$ A)

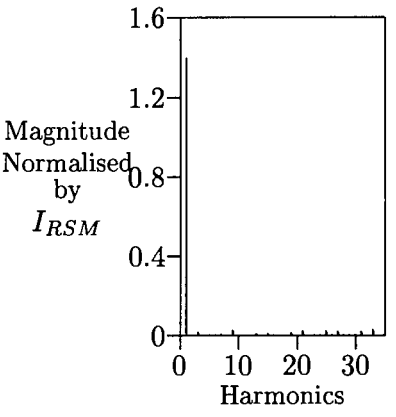

(d) ($m_a = 1.4$)

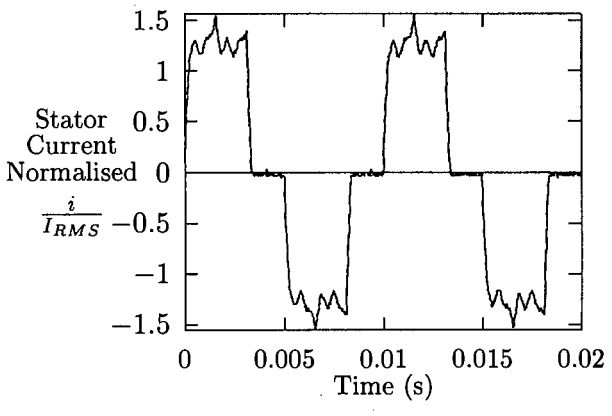

(e) DC Square-wave (I_{RSM} - 2.64 A)

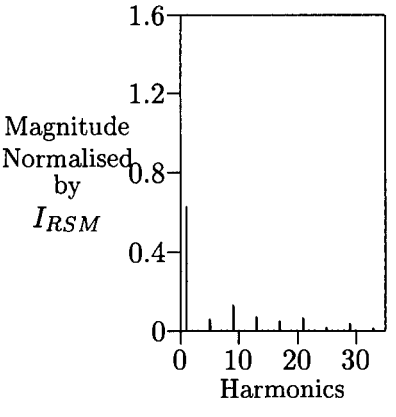

(f) DC Square-wave

Figure 5.7: Stator current waveforms and frequency spectrum magnitudes for sinusoidal PWM mode with $m_a = 1.0$ and $m_a = 1.4$, and DC square-wave mode

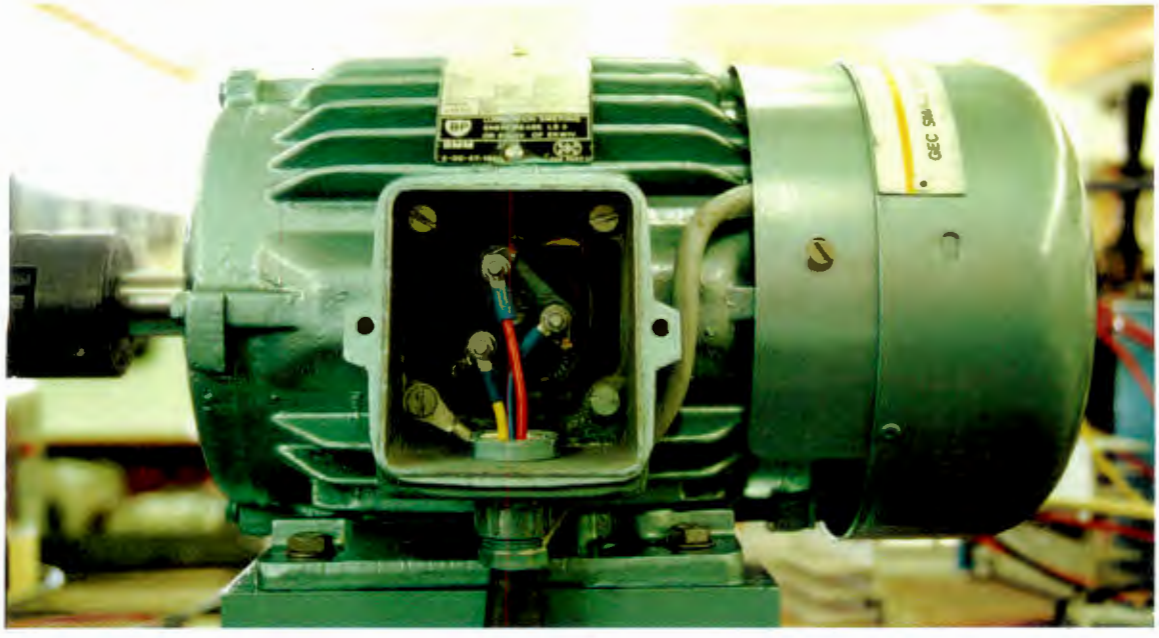

Figure 5.8: PM universal motor

Figure 5.9: Optical position sensors connected to end of motor casing

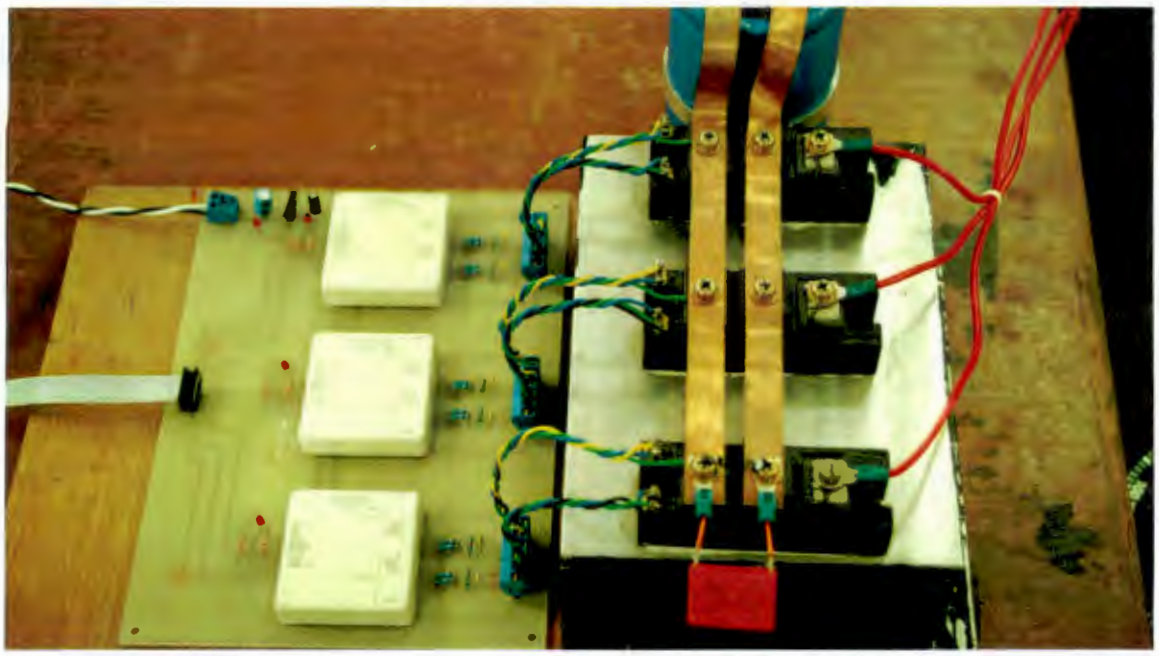

Figure 5.10: IGBT and Semikon modules

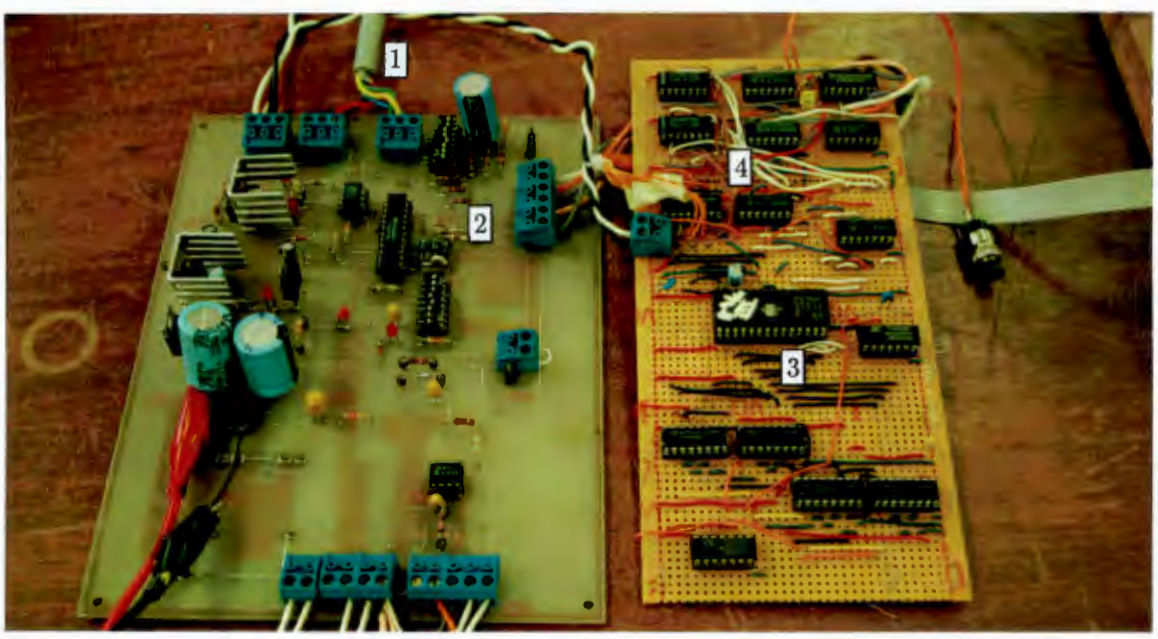

KEY:
1 – Position input signals
2 – DC square-wave generation
3 – PWM sinewave generation
4 – Switching logic

Figure 5.11: Prototype electronics used for sinusoidal PWM and DC generation

drive would not use the semikron drives as they are bulky and expensive. Appendix B gives a breakdown of the costs of this motor drive at the prototype stage. It can be seen that these Semikron drives are an substantial proportion of the cost of the drive.

The prototype electronic board for the synchronous and DC modes of switching are shown in Fig 5.11. Most of the development was done on veroboard so that design changes and improvements could be made with no additional expense to the project.

The development of a PM brushless universal motor has been shown to be competitively priced against a variable speed induction motor drive of similar power rating, as shown in Appendix B.

5.5 Performance of the PM Brushless Universal Motor's Operating modes

The phase shift angle α of the brushless DC control has been investigated to ensure the optimum angle is chosen. Fig 5.12 shows the effect of advancing or retarding the phase shift angle, around the optimum point, on the efficiency of the motor. Fig 5.13 shows the speed - torque characteristics due to the change in α. From Figs 5.12 and 5.13 it can been seen that the motor's performance is extremely sensitive to a retarding of the phase shift angle by as little as 3^o (electrical). The advancing of α shows an increase in rotor speed at low load levels due to the field weakening [109]. The increase in α also causes an increase in the phase current resulting in the reduced efficiency [51].

The efficiency of the complete drive is tested and a comparison of the different modes is shown in Fig 5.14. The sinusoidal PWM mode has $m_a = 1.4$. The DC mode is tested for constant speed operation and for maximum speed operation, with $\alpha = 0^o$. The constant speed DC mode maintained a constant speed until it reached the shunt torque-speed characteristic of the DC mode. The constant speed DC mode uses PWM switching to reduce the average voltage and thus maintain a constant speed, but with increase switching losses over the maximum speed DC mode. Fig 5.15 shows the constant speed characteristic of the synchronous motor and the shunt characteristic of the DC motor.

5.6 Integrated motor

The integrated drive combines the electronic controls, power electronics and mechanical motor into one casing [51, 53, 71]. The traditional concept is to separate the mechanical functions from the electronic functions which in turn requires a network of cables. In the integrated drive, the electronic control and power electronics are mounted inside the motor against the casing, thus reducing the number of input wires to the motor and forming a structurely sound design. The future of the universal motor depends on the success of integrating it into an

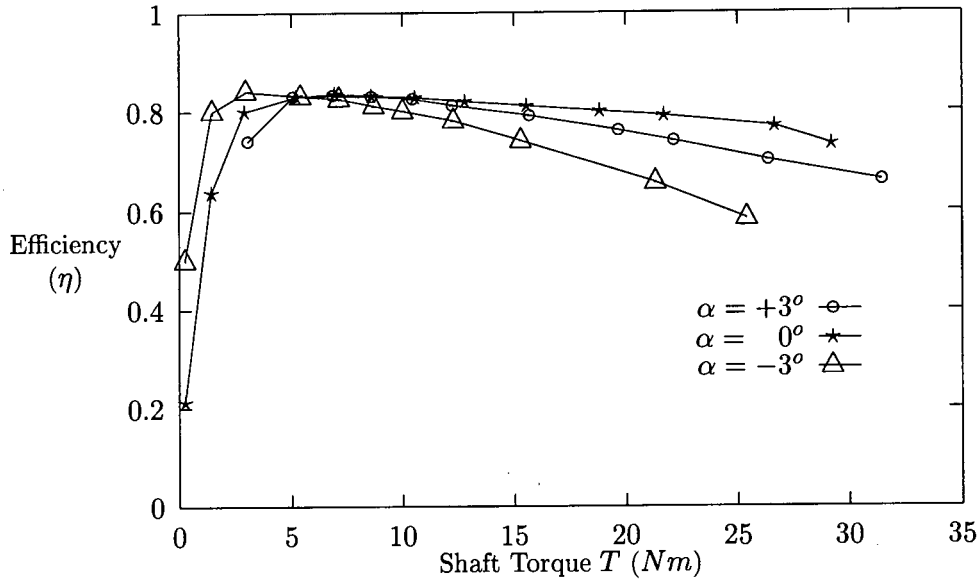

Figure 5.12: Efficiency versus output torque in brushless DC mode with different values of firing angle (α)

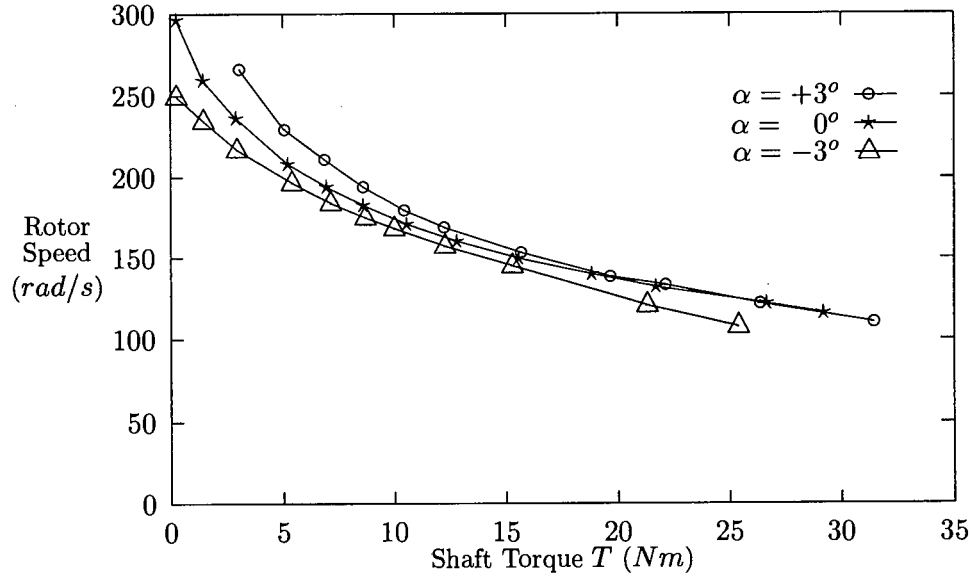

Figure 5.13: Rotor speed versus output torque in brushless DC mode with different values of firing angle (α)

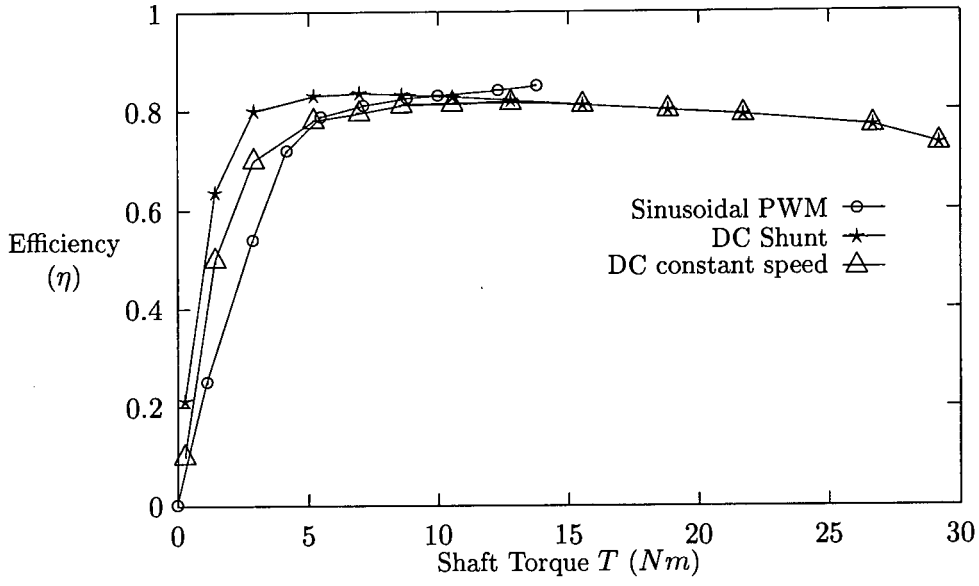

Figure 5.14: Efficiency versus output torque for synchronous and brushless DC modes of operation

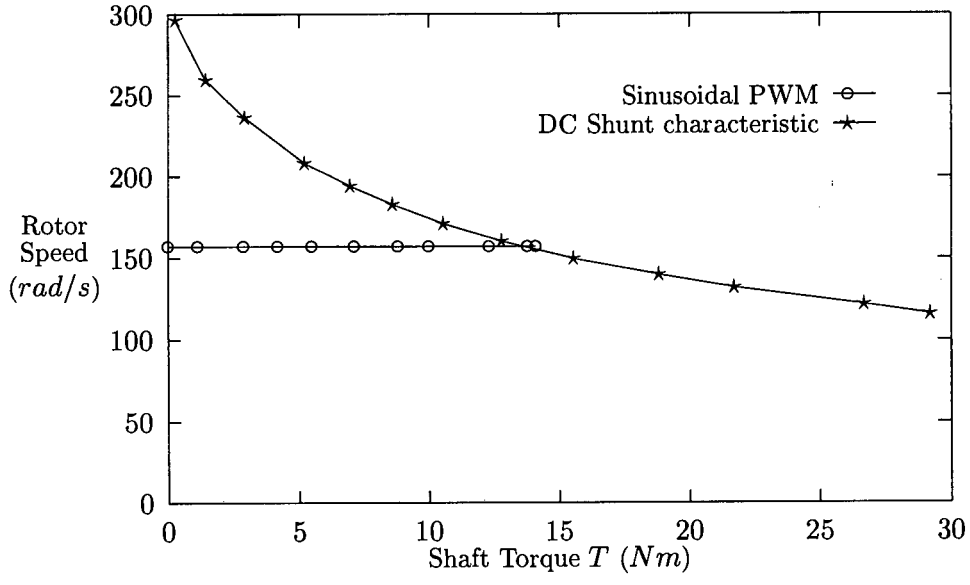

Figure 5.15: Speed - torque characteristics of the synchronous and DC brushless motors

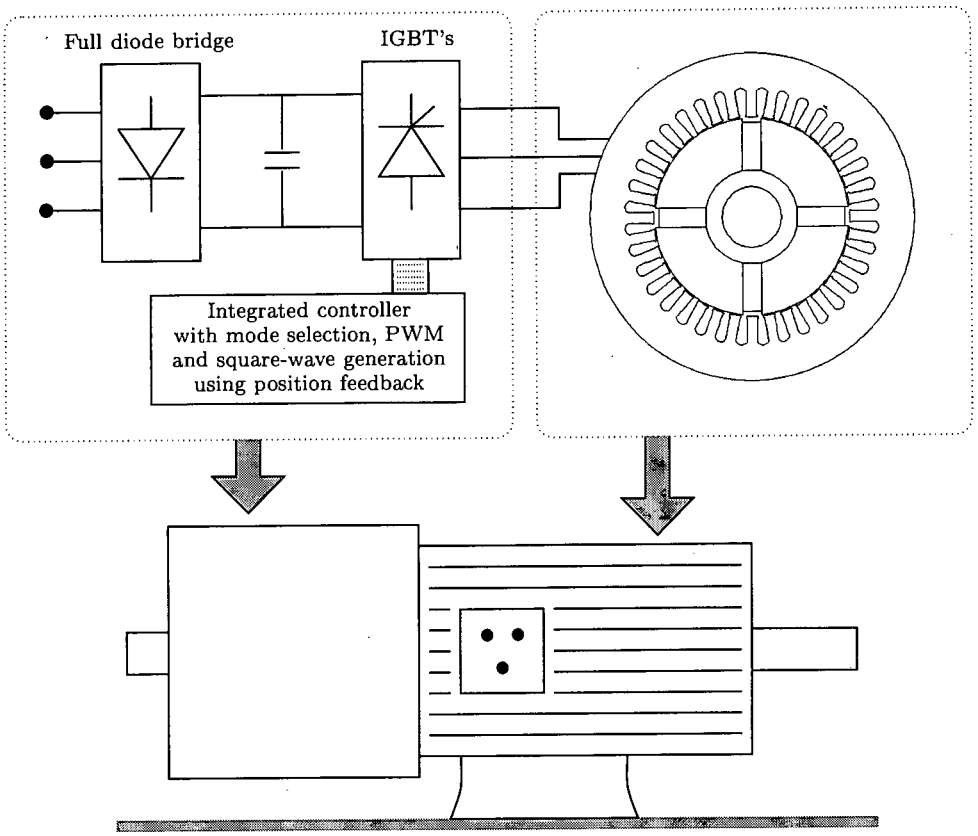

Figure 5.16: Total integration of mechanical, power electronics and control into a smart motor

integrated or smart motor. Fig 5.16 shows graphically the concept of an integrated universal motor. The motor would use either a three-phase or single-phase supply with a single speed control signal.

Chapter 6

Optimisation

Optimisation methods try to find the maximum or minimum of a function, where there may exist restrictions or constraints on the independent variables. Finding the maximum or minimum of a function which is also the global maximum or minimum of the function has considerable difficulty and is the complex part of any optimisation method. In engineering, it is generally considered practical only to search for local solutions.

In the optimisation of electrical machines the objective function and constraints can be computed using either classical (circuital) approach or a numerical field computation approach, such as the FEM. The classical approach (Chapter 4) is not considered to be very accurate except in cases where the motor's magnetic and electric circuit can be modelled very simply. The FEM (Chapter 4) is much more accurate but requires substantially more sophisticated software and computational time. The FEM is considered the more appropriate method to use for optimisation of PM synchronous motors due to its superior accuracy over classical approaches.

The **aim** of this optimisation procedure is to minimise the volume of PM material used on the rotor, while ensuring a rated power, desired power factor and efficiency. Only the rotor is being optimised since the stator of an existing induction motor is used to reduce the total manufacturing costs. The motor is being optimised for synchronous operation, although the motor will run as a universal motor in both synchronous and DC modes (Chapter 5). This is since the dominant mode of operation is synchronous. The mechanical losses are assumed to be constant for a given rated output power and speed.

In numerical field computation problems the standard prerequisites of local optimisation (convexity, differentiability, accuracy of the objective function) are usually not guaranteed. Deterministic optimisation tools for solving local optimisation, such as steepest-decent, conjugate gradient and quasi-Newton methods, are not ideally suited to numeric electromagnetic problems [47]. This is due to the objective functions containing discretisation errors and the derivatives of the objective functions can only be approximated by difference schemes. Recently, non-iterative optimisation schemes have been proposed using artificial neural networks

[66, 76, 94]. Stochastic methods of optimisation have, however, become more popular over the last few years for optimisation of electrical machines due to their high probability of finding global minimum [22] and their simplicity. Stochastic methods such as simulated annealing (SA) [9, 96, 107], genetic algorithm (GA) [22, 36, 113] and evolution strategies [55] have been successfully used for different aspects of electrical machine design.

The recently proposed *population based incremental learning* (PBIL) method [6] is a stochastic non-linear programming method which shows many advantages over the present stochastic methods. A short overview of non-linear programming methods is given, which helps to place the PBIL method with respect to other non-linear programming methods.

Stochastic optimisation has the disadvantage that it is not very efficient. This problem is compounded by the large computation time of numeric field computations. A solution to this problem is the use of *response surface methodology* [20], which has already been successfully used for optimisation of segmental PM DC motors [22].

6.1 Mathematical formulation of optimisation problem

The optimisation of an electrical machine can be formulated as a general constrained optimisation problem with more than one objective i.e. minimisation of the amount of permanent magnet material, maximisation of the efficiency and output power. Finding the extremum (`Extr`) of vector-optimisation problems is defined as:

$$\texttt{Extr}\, F(\vec{x}) = \texttt{Extr}\, [f_1(\vec{x}), f_2(\vec{x}), \ldots, f_k(\vec{x})] \tag{6.1}$$

where

$$F : \Re^n \rightarrow \Re^k \qquad g_i, h_j : \Re^n \rightarrow \Re \qquad \vec{x} \in \Re^n \qquad \vec{x} = (x_1, x_2, \ldots, x_n)$$

subject to specified equality and inequality constraints:

$$g_i(\vec{x}) \leq 0 \qquad (i = 1, 2, \ldots m) \tag{6.2}$$

$$h_j(\vec{x}) = 0 \qquad (j = 1, 2, \ldots p) \tag{6.3}$$

and specified limits for the independent variables:

$$\vec{x}_{min} \leq \vec{x} \leq \vec{x}_{max} \tag{6.4}$$

$F(\vec{x})$ is the vector objective function with the objectives $f_i(\vec{x})$ to be minimised, $\vec{x}$ is the vector of design variables used in the optimisation, g_i are the nonlinear inequality constraints, h_j are the equality constraints, and $\vec{x}_{min}$ and $\vec{x}_{max}$ are vectors of lower and upper bounds for

the design variables.

In vector optimisation problems there is a conflict between the individual objective functions $f_i(\vec{x})$ since there exists no solution vector $\overline{\vec{x}}$ for which all objectives gain their individual minimum. Vector optimisation problems can be transformed from multi-objective optimisation into single objective optimisation using the method of objective weighting. Although objective weighting always leads to a non-inferiority (Pareto-optimal) feasible solution [28, 115], the estimation of the weighting factors and the optimisation starting point is a subjective choice, and their influence can rarely be estimated in advance.

A more practical method of optimisation is to minimise only one objective function while restricting the others with appropriate constraints. Most constraints will be upper or lower bound inequality constraints, which means constrained optimisation procedures are required. The optimisation is thus done for a feasible region, in which all the constraints are satisfied for the design variables.

6.2 Non-linear programming methods

In non-linear programming both the objective and constraint functions maybe non-linear. There is no general agreement to the best optimisation method or approach [40]. The extremely vast subject of non-linear programming has been divided into direct search methods, stochastic methods and gradient methods [21, 94]. A short review of these three classes is described below.

Most numerical field problems have constraints of one form or another. A summary of the main constrained optimisation techniques is also discussed below.

6.2.1 Direct search methods

Direct search methods are minimisation techniques that do not require the explicit evaluation of any partial derivatives of the function, but instead rely solely on values of the objective function plus information gained from earlier iterations. Direct search methods can loosely be divided into three classes, named tabulation, sequential and linear methods [21].

Tabulation methods assume that the minimum lies within a known region. The methods of locating the optimum are: (i) evaluate the function at *grid* points covering the region given by the inequalities, (ii) a *random search* and assume that the minimum would be found within a sufficiently large number of evaluations, or (iii) a generalised *Fibonacci search* by finding the solution of the multivariate minimisation problem by using a sequence of nested univariate Fibonacci searches [40].

Sequential methods investigate the objective function by evaluating the function at the vertices of some geometric configuration in the space of the independent variables. This method originated with evolutionary operation (EVOP) proposed by Box [19].

Evolutionary operation is based on *factorial designs.* The objective function is evaluated at the vertices of a hypercube in the space of the independent variables. The vertex with the minimum function value becomes the centre point of the next iteration and a new design is constructed about this point. This is a mutation type search mechanism which directs the search towards the optimal. *Fractional factorial experimentation* assume systematic and symmetric vertices to reduce the number of objective function evaluations.

The simplex method evaluates the objective function of n independent variables at $n+1$ mutually equidistant points, forming the vertices of a regular simplex. The vertex with the highest value is reflected in the centroid of the remaining n vertices, forming a new simplex. The size of the simplex is reduced if one vertex remains unchanged for more than M consecutive iterations, thus narrowing the search to the minimum.

Linear methods use a set of direction vectors to direct the exploration [42]. There are a large number of linear methods available such as:

(i) *The alternating variable search method* which considers each independent variable in turn and alters it until a minimum of the function is located, while the remaining $(n-1)$ variables remain fixed.

(ii) *The method of Hooke and Jeeves* which uses exploratory moves and pattern moves to direct the search towards the minimum by attempting to align the search direction with the principal axis of the objective function.

(iii) *Rosenbrock's method* which uses n mutually orthonormal direction vectors. Perturbations along each search direction are done in turn and if the result is no greater than the current best value, this trial point replaces the current point. This is repeated until the minimum is obtained.

(iv) *Davies, Swann and Campey method* uses n mutually orthonormal direction vectors and a linear univariate search algorithm on each direction in turn. After each stage is complete, the direction vectors are redefined.

(v) *Quadratic convergent methods* minimise functions which are quadratic in the independent variables making use of conjugate directions.

(vi) *Powell's method* is based on mutually conjugate directions and ensures that a direction is replaced only if by doing so a new set of direction vectors, at least as efficient as the current set, is likely to be obtained.

6.2.2 Stochastic methods

Simulated annealing (SA). This method generates a sequence of states based on an analogy from nature's thermodymanics where a system is slowly cooled in order to achieve its lowest energy state. This is done using natures own minimisation algorithm based on the Boltzmann probability distribution. Thus the design configuration is changed from one to two with objective functions f_1 and f_2, with a probability of $p = exp[-(f_2 - f_1)/kT]$. If $f_2 > f_1$, the new state is accepted with probability p. If $f_2 < f_1$, then the probability is greater than one and the new state f_2 is accepted. At a given temperature, the configurations are arbitrarily changed using a random number generator and the designs are also changed if so dictated by a probability greater than one. The temperature is thus lowered for the next round of searches. This makes uphill excursions less likely and limits the search space. SA ultimately converges to the global optimum.

Multiple-restart stochastic hillclimbing (MRSH). This method initially generates a random list of solution vectors of the independent variables, using binary vectors. The solution vector corresponding to the minimum result of the objective function is used in an iterative loop. A bit of the solution vector is toggled and evaluated. The minimum for a sufficiently large number of iterations is assumed to be the minimum of the objective function.

Genetic algorithm (GA). This search method is rooted in the mechanisms of evolution and natural genetics. A GA combines the principles of survival of the fittest with a randomised information exchange. GAs generate a sequence of populations by using a selection mechanism, and use crossover as the search mechanism to guide the search towards the optimal solution.

Population-based incremental learning (PBIL). This is a combination of evolutionary optimisation and hillclimbing [6]. PBIL is an abstraction of the GA that maintains the statistics of the GA, but abstracts away the crossover operation and redefines the role of the population.

6.2.3 Gradient methods

Gradient methods select the direction $\vec{d_i}$ of the n dimensional direction vector, using values of the partial derivatives of the objective function f with respect to the independent variables, as well as values of f itself together with information gained from earlier iterations. The solution is thus improved, that is

$$F(\vec{x}_{i+1}) \leq F(\vec{x}_i) \qquad \vec{x}_{i+1} = \vec{x}_i + h_i\vec{d}_i \tag{6.5}$$

where h_i is the step increment and $\vec{d_i}$ is the search direction. Types of gradient optimisation methods are:

Methods of steepest descent uses the normalised gradient vector at the current point to obtain a new point using a specified step length.

Newton's methods uses a second order truncated Taylor series expansion of the objective function $F(\vec{x})$. The method requires zero, first and second derivatives of the function at any point.

Quasi-Newton method's use an approximation of the second derivative of the function which is updated after each iteration.

6.2.4 Constrained optimisation techniques

Constrained optimisation problems are generally transformed to unconstrained ones, and are then optimised using one of the non-linear programming methods described above. Some of the techniques used on constrained problems are:

Feasible direction method attempts to maintain feasibility by searching from one feasible point to another along feasible arcs. This methods assumes a feasible point can be found when the procedure starts.

Penalty function transforms the optimisation problem to include the constraints which enable F to be maintained whilst controlling constraint violations by penalising them.

Exact penalty function is similar to the classical penalty function except that the absolute value of the constraints are used [40].

Sequential unconstrained minimisation technique is also similar to the classical penalty function except the penalty coefficient is increased after each step of the algorithm.

Augmented Lagrangian function or multiplier penalty function uses a Lagrangian function to which the penalty term is added. The problem is transformed to an augmented Lagrangian function which is minimised.

6.3 Population-based incremental learning

In terms of Darwinian's models of natural selection and evolution, life is a struggle in which only the fittest survive to reproduce. GAs are based on natural selection and genetic recombination, and were first proposed by Holland [50]. GAs generate a sequence of populations by using a selection mechanism, crossover and mutation as search mechanisms.

In nature, competition for resources such as food means that the fittest individuals of a species dominate over the weaker ones. This natural phenomenon is called "the survival of the fittest". The fittest individuals thus get a chance to reproduce and in this way ensures, implicitly, the survival of the fittest genes. The reproduction process combines the genetic material (chromosome) from the parents into a new gene. This exchange of part of the genetic material among chromosomes is called *crossover*.

GAs encode the solution as a population of binary strings. Each solution is associated with a fitness value determined from the objective function. The main operation in GA is crossover, although *mutation* plays the role of regenerating lost genetic material by causing sporadic and random alteration of the bits of the binary strings. GAs are generally characterised by their population size, crossover type, crossover rate and elitist selection [8]. These control parameters affect how well the algorithm performs. The optimum set of parameters is dependent on the application.

PBIL is an abstraction of the GA that explicitly maintains the statistics contained in a GA's population, but abstracts away the crossover operation [6, 8]. PBIL is in fact a combination of evolutionary optimisation and hillclimbing. The algorithm uses a real valued probability vector which, when sampled, reveals a high evaluation solution vector with high probability.

The PBIL algorithm creates a probability vector from which samples are drawn to produce the next generations population. As in the GA, the solution is encoded into a binary vector of fixed length. Initially the values of the probability vector are set to 0.5. A number of solution vectors, analogous to the population in GAs, are generated based upon the probabilities of the probability vector. The probability vector is pushed towards the generated solution vector with the highest evaluation (fitness value). This probability vector can thus be considered a prototype for high evaluation vectors for the function space being explored. Each bit of the probability vector is updated using:

$$p_i = [p_i \times (1.0 - \delta l)] + (\delta l \times s_i) \tag{6.6}$$

where p_i is the probability of generating a one in the bit position i, s_i is the ith position in the solution vector for which the probability vector is being changed and δl is the learning rate. The learning rate is the amount the probability vector is changed after each cycle.

A new set of solution vectors are produced after each update of the probability vector.

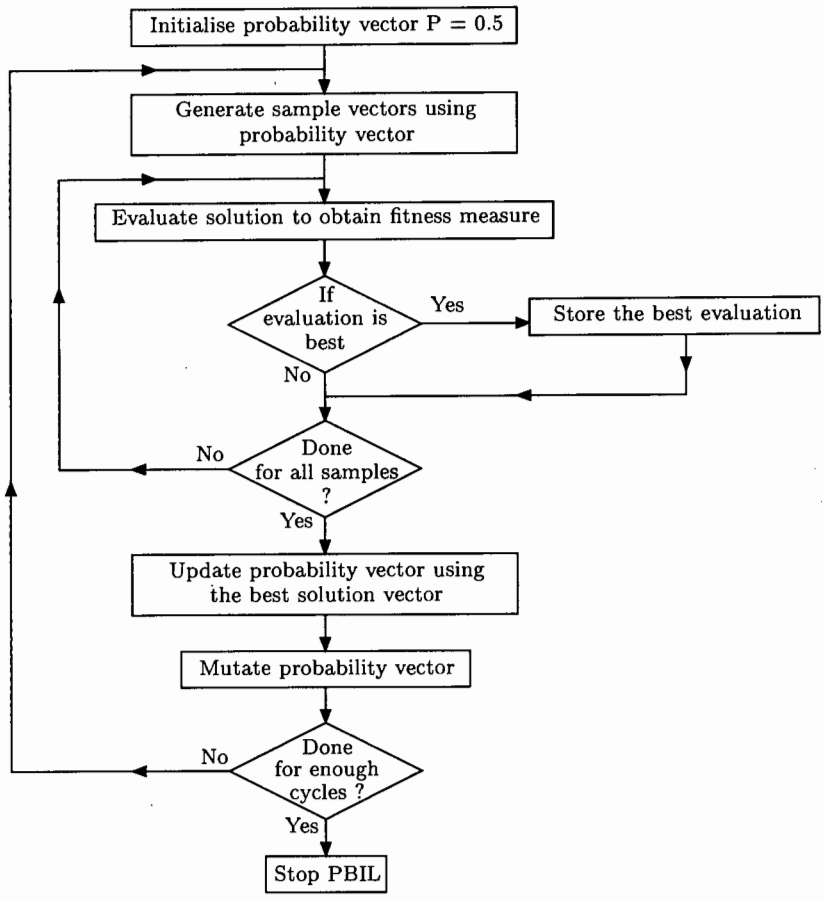

Figure 6.1: Flow chart of PBIL algorithm

The entries in the probability vector start to drift towards either 0.0 or 1.0, as the search progresses, to represent a high evaluation solution vector.

Mutation is used in PBIL for the same reasons as in the GA, to inhibit premature convergence. Mutations perturb the probability vector with a small probability in a random direction. PBILs are generally characterised by their number of samples, learning rate, number of vectors to update from and mutation rate [8]. Fig 6.1 shows a flow chart representation of PBIL.

PBIL has been shown to work as well, or better, than the GA [7]. The main advantage of the PBIL over the GA is that since PBIL is characterised by fewer parameters and their values are less problem related, as little problem-specific knowledge as possible is needed [7].

6.4 Response surface methodology

Due to the large computation time of numeric field computations based on finite element analysis, a faster approach than a straight PBIL is needed for modelling the objective function being optimised. Response surface methodology (RSM) is a collection of mathematical and statistical techniques useful for analysing problems of several independent variables and model exploitation.

By careful design of the FEM experiments, RSM seeks to relate the output variable to the input variables that affect it. The computer experimental result y as a function of the input independent variables $x_1, x_2, \ldots, x_n$ is:

$$y = f(x_1, x_2, \ldots, x_n) + \delta b(x_1, x_2, \ldots, x_n) + \delta\epsilon \tag{6.7}$$

where $\delta b(\vec{x})$ is the bias error and $\delta\epsilon$ is a random error component [20]. If the expected result is denoted by $E(y) = \eta_s$, then the surface represented by $\eta_s = f(x_1, x_2, \ldots, x_n)$ is called the response surface.

The form of the relationship between the result and the independent variables is unknown. A polynomial expression is used as a suitable approximation for the true functional relationship between y and the independent variables. A polynomial expression of degree d can be thought of as a Taylor's series expansion of the true underlying theoretical function $f(\vec{x})$ truncated after terms of dth order. The assumption that low order polynomial models can be used to approximate the relationship between the result and the independent variables within a restricted region of the operability space is essential to RSM. Second order polynomial models are used to model the response surface.

$$f(x) = b_o + \sum_{i=1}^{n} b_i x_i + \sum_{i=1}^{n} b_{ii} x_i^2 + \sum_{i=1}^{n} \sum_{j=1}^{n} b_{ij} x_i x_j \tag{6.8}$$

where $i < j$, and the coefficients b_o, b_i, b_{ii} and b_{ij} are found using the method of least squares [78]. These unknown coefficients can be estimated most effectively if proper computer experimental designs are used to collect the data. Designs for fitting response surfaces are called response surface designs.

6.4.1 Response surface designs

An experimental design for fitting a second order model must have at least three levels of each factor, so that the model parameters can be estimated. Rotatable designs are the preferred class of second order response surface designs [20]. The variance of the predicted response at a point x, in a rotatable design, is a function only of the distance of the point from the design centre and not a function of direction.

The collecting of the sample results is essential since a sufficiently accurate approximation

has to be found with a minimum of experiments. If not all the factorial combinations are employed the design is called an incomplete factorial design. The *Box-Behnken three level design* [18] has been chosen for investigating the response surface. This is an incomplete factorial design which is a reasonable compromise between accuracy of the function and the required number of computations. The design generates second order rotatable designs or near-rotatable designs, which also posses a high degree of orthogonality.

6.4.2 Estimation of errors in response surface fitting

The errors in design of experimental methods are generally divided into two types [20]: (i) systematic or bias errors $\delta b(\vec{x})$ which are the difference between the expected value of the response $E(y) = \eta_s$ and the approximating function $f(\vec{x})$, and (ii) the random or experimental error $\delta\epsilon$ in sampling.

In numeric computer experiments replicated experiments result in the same result, so random errors cannot be defined. Only the bias error from systematic departure of the fixed polynomial from the real response, due to an insufficient polynomial order, can be calculated. An estimate of the variance σ^2 of the bias error is [72]:

$$s_e^2 = \frac{1}{m-p}\sum_{i=1}^{m}(y_i - \hat{y}_i)^2 \tag{6.9}$$

where s_e is the standard error of estimate, m is the number of observations, p is the number of coefficients in the polynomial, y_i is the observed response and $\hat{y}_i$ is the predicted response.

The normalised error is [22]:

$$\overline{\delta b} = \frac{s_e}{y_o} \tag{6.10}$$

where $y_o = (y_1 + y_2 + \ldots + y_n)/m$.

The accuracy of the response surface $E(y)$ is varied by changing the size of the investigated region, since only second order polynomials are used.

6.5 PM synchronous motor output characteristics

The motor's characteristics have been calculated using finite element analysis and classical machine theory (Chapter 4). The whole FEM process from mesh building to obtaining the relevant information from the field quantities has been automated. This was done using MagNet5's script language [35], and a controlling program that writes the scripts and evaluates the numeric field results using classical machine theory.

The model building routine is divided into the surface PM rotor, with and without mild steel pole shoes, and buried PM rotor parts. Since only the design of the rotor is being optimised, the same stator is used in both the surface PM and buried PM rotor designs. The

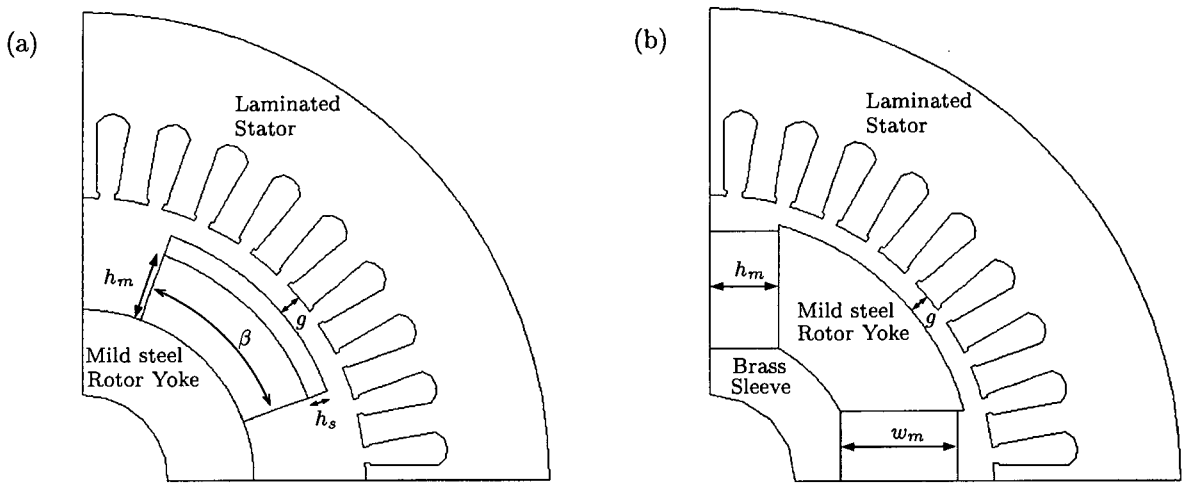

Figure 6.2: Geometric layout of PM rotors showing design variables for (a) surface PM rotor with a mild steel pole shoe and (b) buried PM rotor

independent variables used in the surface PM rotor design are the airgap g, PM thickness h_m, pole shoe thickness h_s and the overlap angle β, and in the case of the buried PM rotor design they are the airgap g, PM thickness h_m and PM width w_m (Fig 6.2).

The model building routine validates the rotor design, to ensure that it is geometrically possible to fit into the stator, before the mesh is built. Fig 6.3 shows the logic sequence followed by the control program. The output characteristics of the PM motor are the output power, power factor and efficiency ratings, the thermal limits of the stator winding, and the volume of PM material used. The power factor has been included as a constraint due to the importance of having a motor with a good power factor when using an inverter drive.

The characteristics obtained from the FEM, using the flux linkage and magnetising loading methods, as shown in Chapter 4, are E_o, X_{sd}, X_{sq}, X_{md} and X_{mq}. The following simplifications are made for the FEM:

(a) The end leakage reactance is calculated using classical theory since it would be difficult to calculate using a two-dimensional FEM.

(b) The induced EMF and inductive reactance are assumed constant throughout the load range, and equal to the value obtained at rated current.

(c) The model is independent of rotor position, so only one rotor position is used in the analysis.

The electromagnetic power developed P_e is calculated using eqn (3.7) and the electrical input power is $P_{in} = 3VI_1\cos(\theta + \delta)$, from the phasor diagram in Fig 3.1. An iterative

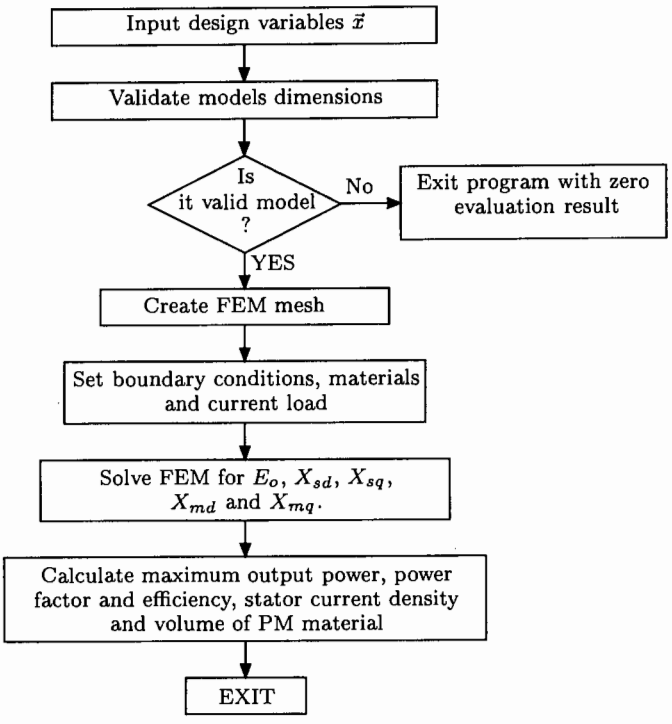

Figure 6.3: Flow chart of the control program which produces the motor output characteristics

procedure has been used to calculate the maximum electrical power developed, and the power factor and efficiency at the rated developed power. The optimisation procedure assumes a terminal voltage $V = 220$ V per phase, so a performance comparison can be done with the previously designed PM synchronous motors, shown in Chapter 2. The terminal voltage would, however, be slightly less when using a PWM inverter drive (Chapter 5).

Since the electrical design is being optimised the mechanical losses P_{rot}, due to windage and bearing friction, are assumed constant. A further simplification is made in assuming the core losses produced in the stator and rotor cores to be negligible. The efficiency used as a inequality constraint in the optimisation is thus $\eta = (P_e - P_{rot})/P_{in}$, excluding the core losses.

The thermal analysis is important to preserve the insulation on the stator windings and the detrimental effect of temperature on the permanent magnets [13]. For F class winding insulation of PM synchronous motors which are fan-cooled externally and with power ratings below 3 kW, the stator winding current density limit is between $8 - 11$ A/mm^2. This value also depends on the rated speed and number of poles. For a reasonable winding design the maximum current density is set at 10.5 A/mm^2. Any current density above this maximum is considered infeasible.

The objective function attempts to minimise the volume of permanent magnet material. The axial length of the magnets is assumed to be constant and equal to the stator stack

length. The volume of the magnet on the pole face of a surface PM rotor is $V_m = 1/4 \times \beta(D_{2out}^2 - D_{2in}^2) \times l$, where l is the rotor axial length, D_{2out} and D_{2in} are the outer and inner diameters of the permanent magnet, respectively. The volume of magnet per pole in a buried PM rotor is $V_{pm} = 2h_m w_m l$.

6.6 Using PBIL for PM synchronous motor optimisation

The optimisation problem can be expressed as: *minimise* $V_m(\vec{x})$ subject to the constraints

$$P_e(\vec{x}) \geq P_{e(d)} \qquad J_1(\vec{x}) \leq J_{1th}$$

$$pf(\vec{x}) \geq pf_d \qquad \eta(\vec{x}) \geq \eta_d \qquad g \geq g_{min}$$

$$h_m,\ w_m \geq h_{min} \qquad h_s \geq p_{min} \qquad D_{2out} < D_{2max} \tag{6.11}$$

where V_m is the magnet volume per pole, $P_{e(d)}$ is the desired electromagnetic power, J_{1th} is the current density thermal limit at $P_{e(d)}$, pf_d is the minimum desired power factor at rated P_e, η_d is the desired electrical efficiency at $P_{e(d)}$, g_{min}, p_{min} and h_{min} are the mechanical minimum sizes for the airgap, pole shoe and PM respectively, and D_{2max} is the maximum diameter the outer edge of the PMs.

The PBIL optimisation procedure is shown in Fig 6.1. The output characteristics are evaluated for each sample vector. If the output characteristics of a particular sample vector do not fall within the feasible region its solution is given an extremely large magnet volume.

The PBIL uses a total of 18 sample bits, 6 bits per independent variable. The step size for the variables are 0.00005 m for the airgap g, 0.00068 m for the PM width h_w, and 0.0005 m for the PM height h_m in the buried PM rotor optimisation. The number of bits and step size per variable were chosen to ensure the largest feasible range and the smallest step size reasonable for the mechanical design. A similar set of step intervals have been defined for the surface PM rotor and the surface PM rotor with pole shoes.

6.7 PM synchronous motor optimisation using PBIL with RSM

The objective function, minimisation of the magnetic volume, is not easily expressed in terms of the independent variables. RSM is thus not used for modelling the objective function directly, but rather for modelling the performance characteristics of the PM synchronous motor, used in the constraints, in terms of the independent variables.

The characteristics for a number of combinations of the independent variables (factors)

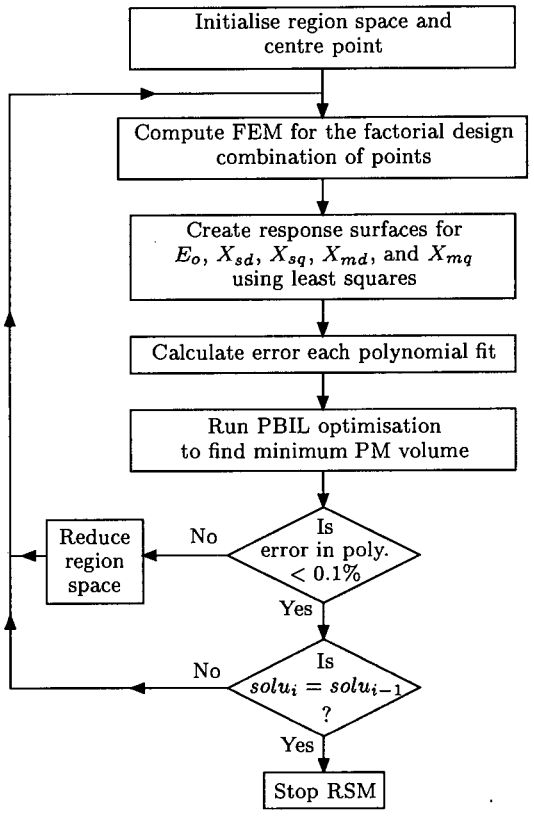

Figure 6.4: Flow chart of RSM optimisation routine

are calculated using the FEM. The factors range over the whole problem space and their combinations are determined by the Box-Behnken three level design method, i.e. with 3 factors and 3 levels the design of experiments needs 15 FE solutions. Response surfaces are created for the output characteristics E_o, X_{sd}, X_{sq}, X_{md} and X_{mq}. A 2nd order polynomial is fitted to each of the five characteristics using the least squares method. Response surfaces were created for these characteristics since they are obtained directly from the FEM and are continuous over the investigated space.

These five polynomials equations are then used to calculate the electromagnetic power, efficiency and stator current in the optimisation procedure. The PBIL optimisation routine (Fig 6.1) is used for the minimisation of the PM volume with the constraints stated in eqn (6.11).

The bias errors in the five response surfaces, as shown in eqn (6.10) are used as a measure of confidence in the optimisation result. If any error $\overline{\delta b} > 0.1\%$ then the process is repeated using the present optimum result as the centre point, but with a smaller search region. This is continued until the errors are small enough and the solution from two consecutive results are approximately equal. Fig 6.4 shows a flow chart sequence of the RSM routine.

6.8 Synchronous PM rotor optimisation results

The aim of this optimisation is to use an existing wound stator of an 1.5 kW induction motor (Table 2.1) and to design a high performance PM rotor with the minimum of PM material.

The initial designs of surface and inset type PM rotors had poor efficiency and performance, as shown in Chapter 2. The advantage of surface PM rotor is that they have a simple design which is easy and cheap to build. The buried PM rotor, shown in Chapter 2, had good efficiency and high performance. Buried PM rotors are more expensive to manufacture than surface PM rotors due to higher machining costs, but their higher saliency makes them the preferred design for synchronous motor drives [51]. The surface PM rotors use radial NdFeB PMs and a solid mild steel rotor yoke, while the buried PM rotor uses rectangular tangentially magnetised NdFeB PMs, a brass sleeve and mild steel rotor poles (Fig 6.2).

The optimisation is done using the straight PBIL and the RSM included in the PBIL. A comparison between the two methods is done to determine the effectiveness of the RSM optimisation procedure in locating the global optima. Table 6.1 shows the optimisation results for a surface PM rotor, a surface PM rotor with pole shoes and a buried PM rotor design with rated electromagnetic power $P_e = 2000$ W and efficiency $\eta_d = 90\%$. The power factor pf has not been used as a constraint in this analysis. Table 6.1 shows that the RSM method optimises to a similar result as the straight PBIL but at a fraction of the time. The straight PBIL used 20 sample vectors and updated the sample vector 100 times, which relates to 2000 solutions of the FEM. The RSM using the PBIL used 100 sample vectors and updated these

Table 6.1: Comparison between PBIL optimisation and RSM using PBIL optimisation for three PM rotor designs, with $P_e = 2$ kW and $\eta_d = 90\%$

Surface PM rotor	g mm	β deg	h_m mm		J A/mm^2	Time taken h	PM volume mm^3 per pole
PBIL	0.3	72.5^o	1.5		9.804	≈ 100	7633
RSM	0.3	72.0^o	1.15		9.818	≈ 3	5857
Surface PM rotor (pole shoes)	g mm	β deg	h_m mm	h_s mm	J A/mm^2	Time taken h	PM volume mm^3 per pole
PBIL	0.3	74.5^o	1.5	0.2	9.906	≈ 100	7805
RSM	0.3	74.65^o	1.018	0.21	9.953	≈ 5.5	5339
Buried PM rotor	g mm	w_m mm	h_m mm		J A/mm^2	Time taken h	PM volume mm^3 per pole
PBIL	0.3	16.80	1.5		10.720	≈ 100	5040
RSM	0.3	16.90	1.349		10.532	≈ 3	4561

vectors 500 times, it cycled through the optimisation procedure 4 times. At each stage in the RSM 15 FEM solutions where needed in the surface PM and buried PM models, using three independent variables, while 27 FEM solutions where needed in the surface PM model with pole shoes, using four independent variables. A total of 60 FEM have been used in the RSM optimisation of the surface PM and buried PM motors, and 104 FEM in the surface PM motor with pole shoes.

The RSM optimisation results found a better solution in all the motor designs. This is due to the higher number of iterations of the PBIL used in the RSM routine and the higher resolution of the independent variables in the RSM optimisation. Further investigation of the optimisation of the surface PM rotors and buried PM motor will be done using the PBIL with the RSM routine described above.

6.8.1 Surface PM rotor results

Table 6.2 shows the optimum results for different constraints in electromagnetic output power, efficiency and power factor for the surface PM rotor. The results show that for low power ratings (1.5 kW) the design needs a substantial increase in PM material if the power factor is

Table 6.2: Optimisation of surface PM rotor using RSM

$P_{e(d)}$ kW	η_d %	pf_d	g mm	β deg	h_m mm	pf	J A/mm^2	PM volume mm^3 per pole
1.5	90	–	0.3	76.85^o	0.77	0.754	8.575	4191
2.0	90	–	0.3	72.00^o	1.15	0.871	9.818	5857
2.5	90	–	0.3	73.80^o	1.75	0.974	10.993	9056
1.5	90	0.90	0.3	74.78^o	1.46	0.900	7.039	7669
2.0	90	0.90	0.3	70.23^o	1.38	0.900	9.718	6793
2.5	90	0.90	0.3	73.80^o	1.75	0.974	10.993	9056
Final result								
2.2	90	0.90	0.3	71.40^o	1.36	0.913	10.315	6838

constrained to a minimum of 0.9. At the high power rating of $P_e = 2.5$ kW the power factor well exceeds the design constraint.

The most feasible power rating for this motor should ensure that the stator winding current density remains below the specifications limits, but also maximise the power output. A power rating of approximately 2.2 kW is thus considered appropriate due to the maximum use of the stator windings.

The stator used in this motor is from a 1.5 kW induction motor. The increase in power rating to 2.2 kW, when operating as a synchronous motor, is due to the higher stator winding current density possible in PM synchronous machines, and the improved efficiency and power factor. The stator winding current density has increased from 9.93 A/mm^2, for the induction motor, to below 10.4 A/mm^2 for the PM synchronous motors. The increased current density is possible due to the reduced rotor losses in the PM synchronous motor as compared with the induction motor.

Higher time and space harmonics as well as the effects of *cogging torque* have been neglected throughout this optimisation procedure. Although the cogging torque cannot be eliminated completely, it can be drastically reduced using an appropriate PM overlap angle [62]. Skewing of the stator teeth is not possible as an existing stator is being used. Using a PM overlap angle of [62]

$$\beta = (K + 0.14)\alpha_{sl} \tag{6.12}$$

where K is an integer and α_{sl} is the slot pitch, ensure that the minimum cogging torque can be achieved. The overlap angle is thus decreased from $\beta = 73.8^o$ to $\beta = 71.4^o$. The airgap

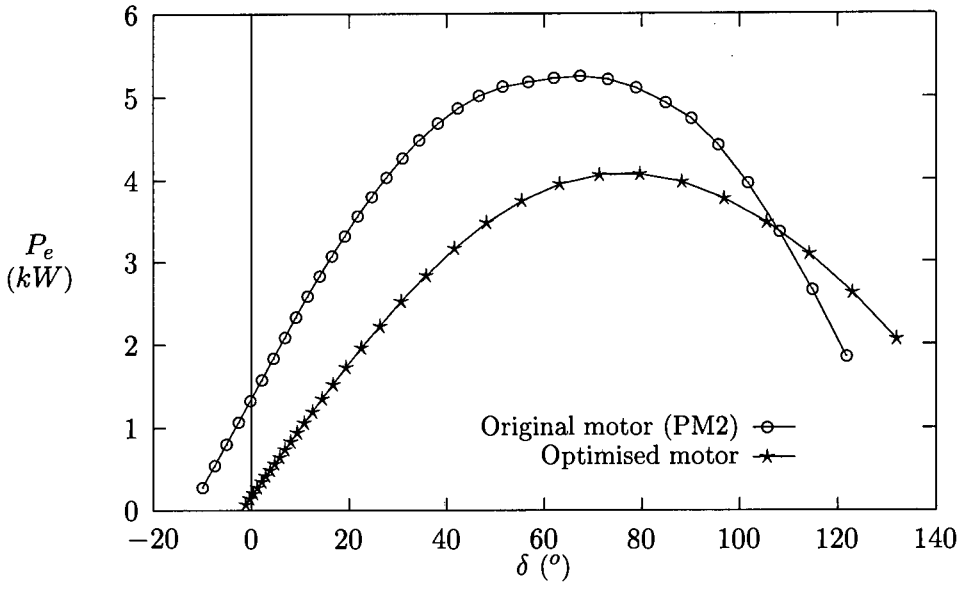

Figure 6.5: Electromagnetic power versus load angle for surface PM motor

and magnet thickness are again optimised for this fixed overlap angle. Table 6.2 shows the final optimise rotor details. Fig 6.9(a) shows a two dimensional cross section of a quarter of the optimised motor.

The performance of this optimised motor is compared with the surface PM rotor (PM2), described in Chapter 2. Fig 6.5 compares the electromagnetic power and Fig 6.6 compares the efficiency for the two motors. The optimised surface PM synchronous motor has superior efficiency at the desired rated power with a reduction in the PM volume from 12000 mm^3 per pole, for the PM2 motor, to 6838 mm^3 per pole, for the optimised motor.

6.8.2 Surface PM rotor with mild steel pole shoes results

Table 6.3 shows the optimum results for different constraints in electromagnetic output power, efficiency and power factor for the surface PM rotor with mild steel pole shoes. The most feasible power rating is again chosen to be 2.2 kW.

The effects of *cogging torque* have again been taken into account in the final design by changing the PM overlap angle, specified by eqn (6.12). Fig 6.9(b) shows a two dimensional cross section of a quarter the optimised motor.

The performance of this optimised motor is compared with the surface PM motor with mild steel pole shoes (PM3), described in Chapter 2. Fig 6.7 and Fig 6.8 compare the electromagnetic power and efficiency for the two motors, respectively. The optimised surface PM motor used 6392 mm^3 of PM material per pole, while the PM3 motor used 12000 mm^3.

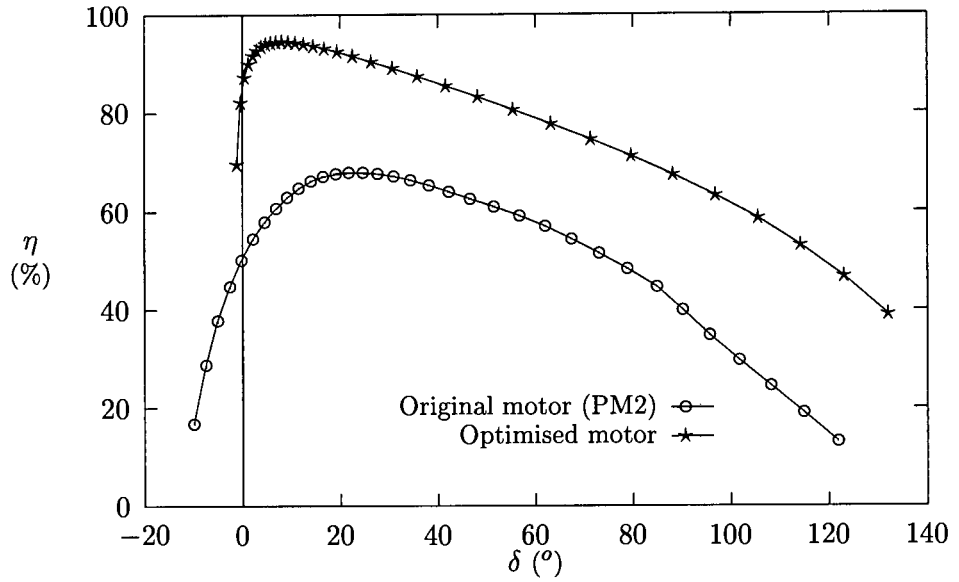

Figure 6.6: Efficiency versus load angle for surface PM motor

Table 6.3: Optimisation of surface PM rotor, with mild steel pole shoes, using RSM

$P_{e(d)}$ kW	η_d %	pf_d	g mm	β deg	h_m mm	h_s mm	pf	J A/mm^2	V_m mm^3 per pole
1.5	90	–	0.3	75.52^o	0.72	0.27	0.773	8.337	3841
2.0	90	–	0.3	74.65^o	1.02	0.21	0.878	9.953	5339
2.5	90	–	0.3	75.31^o	1.64	0.20	0.975	10.936	8629
1.5	90	0.90	0.3	77.13^o	1.32	0.23	0.901	6.901	7109
2.0	90	0.90	0.3	74.32^o	1.18	0.17	0.909	9.403	6171
2.5	90	0.90	0.3	75.31^o	1.64	0.20	0.975	10.928	8628
Final result									
2.2	90	0.90	0.3	71.40^o	1.23	0.20	0.912	10.374	6392

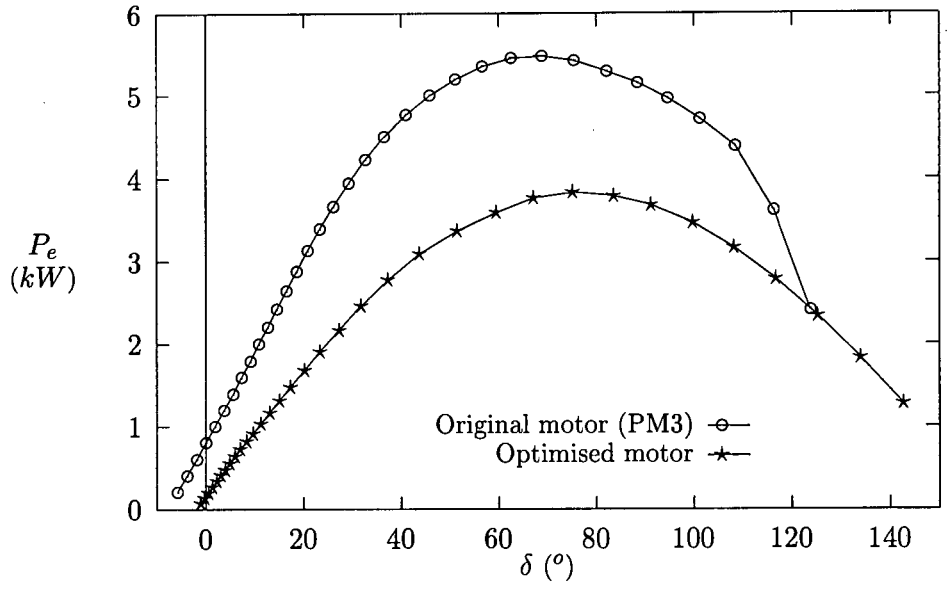

Figure 6.7: Electromagnetic power versus load angle for surface PM motor with mild steel pole shoes

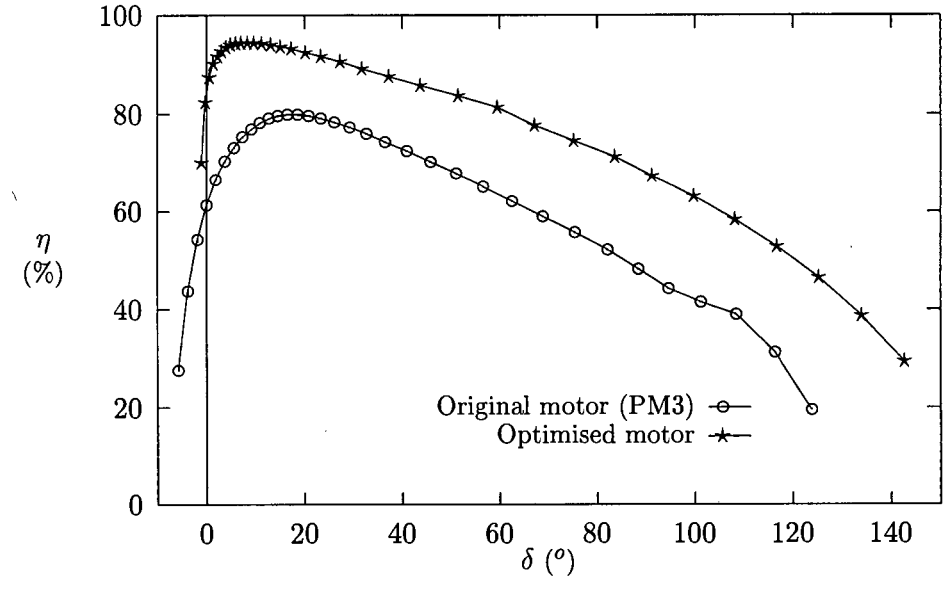

Figure 6.8: Efficiency versus load angle for surface PM motor with mild steel pole shoes

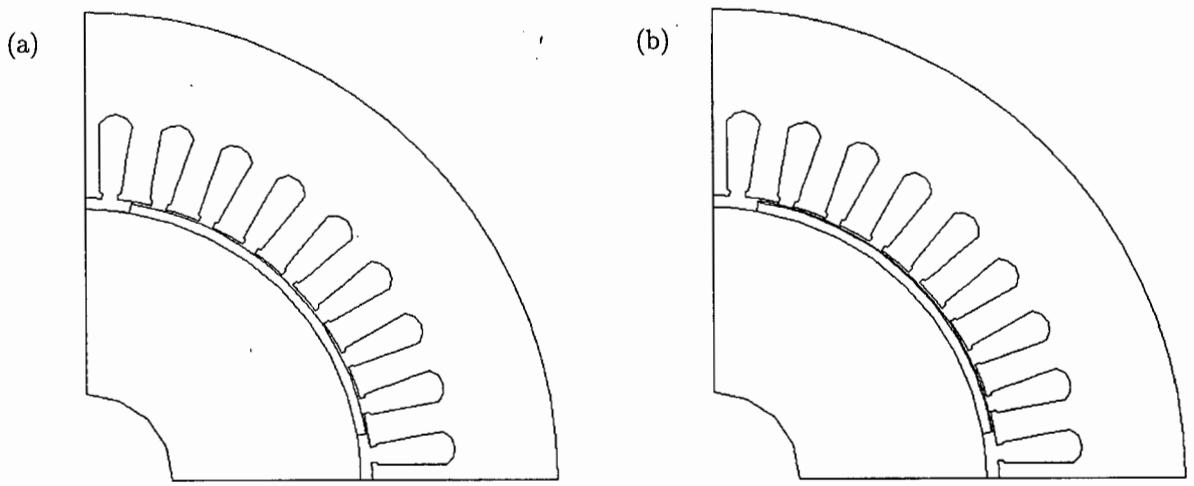

Figure 6.9: Geometric layout of optimum PM rotors designs (a) surface PM rotor and (b) surface PM rotor with mild steel pole shoes

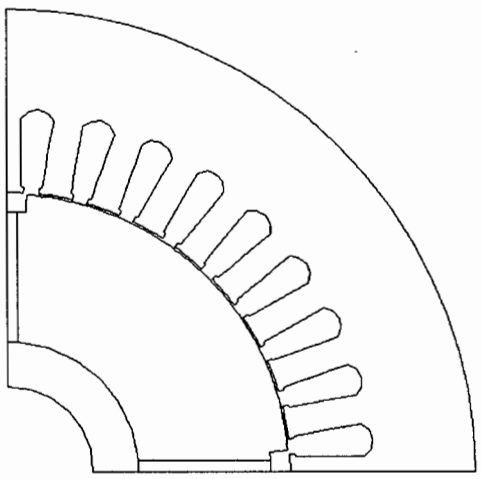

Figure 6.10: Geometric layout of optimum PM rotors designs buried PM rotor

Table 6.4: Optimisation of buried PM rotor using RSM

$P_{e(d)}$ kW	η_d %	pf_d	g mm	w_m mm	h_m mm	pf	J A/mm^2	PM volume mm^3 per pole
1.5	90	–	0.3	15.21	1.21	0.717	8.913	3672
2.0	90	–	0.3	16.90	1.35	0.817	10.532	4561
2.5	90	–	0.3	20.18	1.62	0.913	11.861	6535
1.5	90	0.90	0.3	21.54	2.01	0.910	6.753	8673
2.0	90	0.90	0.3	20.87	1.52	0.900	9.322	6329
2.5	90	0.90	0.3	19.32	1.72	0.910	11.856	6627
Final result								
2.2	90	0.90	0.3	19.28	1.55	0.909	10.388	5977

6.8.3 Buried PM rotor results

Table 6.4 shows the optimum results for different constraints in electromagnetic output power, efficiency and power factor for the buried PM rotor. The most feasible power rating is again chosen to be 2.2 kW.

The effects of *cogging torque* can be taken into account in the final design by changing the size of the mild steel pole face. This has no effect on the optimisation point since it does not change any of the optimisation parameters. The pole face is reduced to an angle specified by eqn (6.12). Fig 6.10 shows a two dimensional cross section of a quarter the optimised motor and illustrates the trimmed pole face.

The performance of this optimised motor is compared with the buried PM motor (PM4), described in Chapter 2. Fig 6.11 and Fig 6.12 compare the electromagnetic power and efficiency for the two motors, respectively. The maximum power output has been reduced in the optimised design to match the power capability of the stator more closely. The optimised buried PM motor used 5977 mm^3 of PM material per pole, while the PM4 motor used 16000 mm^3.

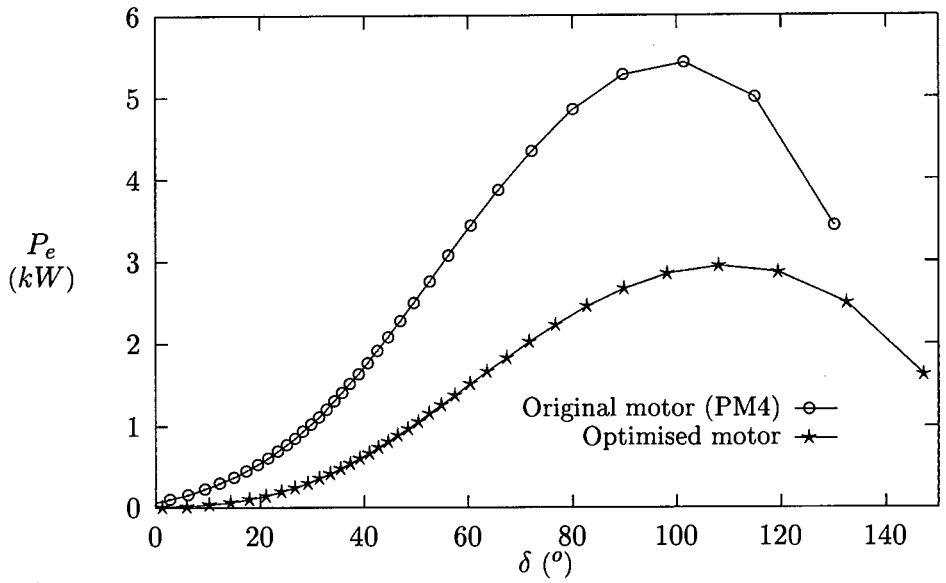

Figure 6.11: Electromagnetic power versus load angle for buried PM motor

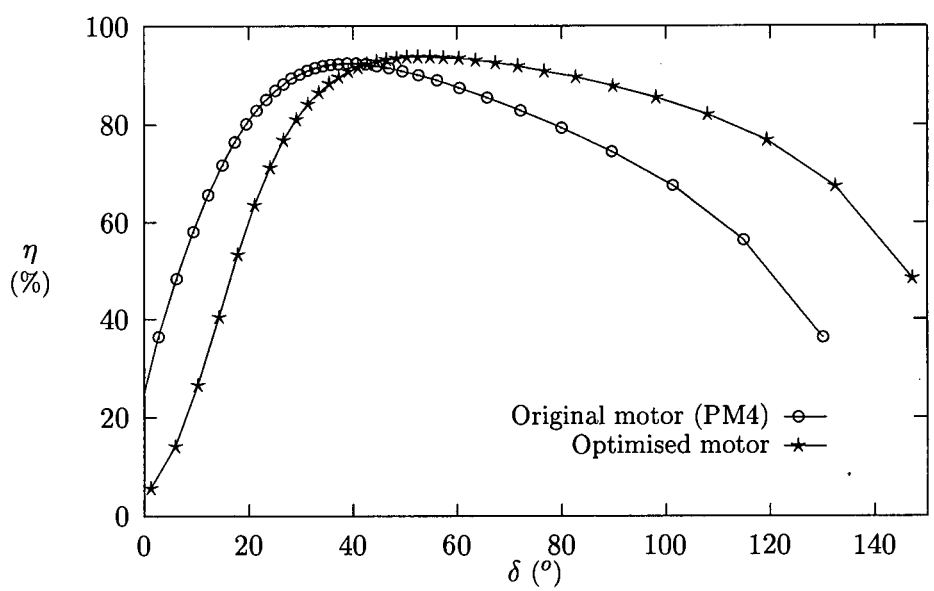

Figure 6.12: Efficiency versus load angle for buried PM motor

Chapter 7

Conclusions

This thesis describes the analysis, design, construction and optimisation of a PM brushless universal motor. Part of the investigation resulted in solving new problems and, in other instances, the investigation resulted in improving more commonly used techniques in this field. This Chapter is divided in terms of original work which has been performed and in terms of general insights gained from this research. From the insight gained in this research future work is also proposed.

7.1 Original work

In this thesis the following new work has been presented:

- A broad comparative analysis of calculating the synchronous reactances of different PM synchronous motors using circuit theory, FEM flux linkage and FEM energy perturbation method has been done. All results have been compared with experimental test results. No publication to-date deals with this problem.
- The sensitivity in the FEM flux linkage calculation of the induced EMF and synchronous reactance, due to small armature current components in I_d and I_q, has been improved. This was accomplished using a constant magnitude disturbance in both I_d and I_q in the calculation.
- A new very efficient universal integrated brushless PM motor drive with synchronous and shunt characteristics has been designed, manufactured and investigated. This motor drive can operate both as a synchronous and DC motor. From a South African economic development point of view, such a motor can operate from a simple single-phase reticulation system using a single-phase-to-three-phase converter or from a three-phase supply.

- A new PM rotor with surface magnets and mild steel pole shoes, for synchronous and brushless DC motor operation has been designed. The mild steel pole shoes help reduce the amount of PM material used compared to normal surface magnet designs. They are also necessary for self-starting and damping oscillations, and protect the PMs against the demagnetising action of the armature flux.

- A population based algorithm has been applied to optimise PM brushless motors. The use of RSM to model the motors' parameters for use in the PBIL has also been successfully implemented, drastically reducing the computational time.

7.2 Insights into universal motor design

- The analytical method of calculating the synchronous reactances and EMF is a very fast process once the correct form of the generalised machine theory is used. The problem with the analytical method is that it is difficult to develop a generalised program that would be able to calculate the synchronous reactances regardless of the motors shape. This is illustrated in the results in Chapter 4.

  The analytical results for simple rotor configurations are more accurate than those for motors with more complicated rotor shapes. In the case of the surface PM rotor with mild steel pole shoes, the analytical method underestimated the q-axis synchronous reactance. This is due to the fact that a large portion of the q-axis flux passing through the pole shoe is not compensated for in the one dimensional analytical method. The measurement and FEM showed that $X_{sq} > X_{sd}$, while the analytical results showed the opposite.

  The circuit theory showed the greatest error in the calculation of the d-axis synchronous reactance for the buried PM motor (PM4). The overestimation of X_{sd} is due to the form factors not compensating for the d-axis flux flowing through the PMs.

  The FEM is much more time consuming to implement than analytical methods but the results are more reliable and independent on the configuration of the rotor. The results show that for all the rotor shapes the finite element results, both flux linkage and energy perturbation, were more accurate than their analytical equivalents.

- From the tests done in Chapter 4 it is possible to state that the energy perturbation method underestimated the synchronous reactances in all the motors tested. This is confirmed by the results shown in [81] in which the energy perturbation method results were less than those obtained by experimental measurements. Although the end leakage was not included in the results in paper [81], it can be assumed that the end leakage reactance would only have contributed to a small improvement in these results, and are thus consistent with the findings in this thesis.

It should also be noted that the flux linkage method is a more computationally efficient method than the energy perturbation method. Assuming that the self inductances and the mutual inductances of the different phases are not equal, the energy perturbation method will require 19 FEMs to calculate the synchronous reactance of one particular operating point while the flux linkage method will only require 2 FEMs.

The FE flux linkage method combined with the loading method is thus seen as the most appropriate method for accurately and efficiently calculating the steady state synchronous reactances and induced EMF for PM synchronous motors.

- The non-linear characteristics of the stator and rotor ferromagnetic materials have been included in the FEM calculations of EMF and synchronous reactance. The change in E_o and the synchronous reactances due to changes in load, and the interaction between the d-axis and q-axis current components have also been successfully included.

- The experimental tests of induced EMF and synchronous reactances using the curve fit scheme proved to be accurate and easy to implement. This method is useful in small to medium size motors where the armature winding resistance is of the same magnitude as the synchronous reactances and performance tests can easily be done.

- The universal motor has been built and tested. It has shown to be a robust and reliable drive in both DC and synchronous modes. The drive is capable of line starting at full load in DC mode and switches automatically to synchronous mode at the correct rotor speed. The drive is also competitively priced against the variable speed induction motor drives presently used in South Africa.

- The PBIL optimisation algorithm has been applied to the optimisation of electrical motors for the first time. This algorithm with the use of RSM has shown to be an excellent tool for the optimisation of PM synchronous motors. Using RSM to model the motors induced EMF and synchronous reactances instead of modelling the optimisation functions directly, ensured that the global optimum is successfully obtained in both the surface PM and buried PM motor designs.

- The performance analysis of the PM synchronous motors done in Chapter 2 highlighted the importance of correctly designing electrical motors. The performance characteristics of these PM synchronous motors showed that the PM rotors were not correctly designed to match the existing stator.

  The optimisation of the surface and buried PM synchronous motors showed improved efficiency at the desired rated power, over the previous designs. The optimised designs also used less PM material. The surface PM rotor designs used thinner magnets than the original designs to increase the synchronous reactance and thus reduce the stator

winding current. The buried PM rotor design is considered a better design than the surface PM rotor, for synchronous operation, due to its high q-axis reactance and high saliency ratio. The optimised surface and buried PM synchronous motors showed that it is possible to design a highly efficient PM synchronous motor using an existing induction motor stator.

7.3 Recommendations for future research

A lot of research into brushless PM motors has been done over the past decade. This thesis considers the design of a new brushless universal motor. Some of the directions in which future research into PM universal motors can proceed are described below.

- The calculation of core losses have been neglected in this thesis. Core loss calculations on motors with solid steel pole shoes require a three-dimensional FE package, because eddy currents in the rotor pole shoes do not flow only in the axial direction, and thus a two-dimensional model would oversimplify the calculation.

  The methods of calculating core losses due to non-sinusoidal field has been described in Appendix A. This description shows that the most recent methods of calculating core losses require a large amount of information about the material properties. There is still a lot of research required into obtaining these material properties accurately, before the accuracy of these methods can justify the high computational effort.

- The FEM results of leakage reactance in the d-axis and q-axis showed different variations with increase in load current. Further research into this problem is needed, with possible changes being made to the analytical theory to include different saturation factors for the d and q axes.

- The heating effects in the motor were not analysed in this thesis. Instead a fairly conservative current density was used in the optimised designs. The irreversible demagnetisation effects of high temperature on NdFeB magnets is an important design constraint. Analysing the temperature of the rotor and stator could possibly lead to an increase in the maximum current density and thus to a higher power per mass ratio.

- The motors designed in the research did not have any noticeable torque ripple problems. The analysis of torque ripple and the effects on synchronous stability is important in the design of synchronous machines. The effect of including a mild steel pole shoe on the magnets of a surface PM rotor should also be investigated. These sub-transients should also be considered for different loads which can introduce added torque ripple.

- The universal motor designed in this thesis has no problems with start-up since it uses the DC brushless mode. As an economical alternative to the universal motor, a self-

starting synchronous motor would have many applications in South Africa. A cheap self-starting rotor should be researched using either surface PMs with pole shoes or a buried PM rotor design. The inclusion of rotor bars should also be considered in this transient analysis.

- The universal motor control and mode switching electronics has been shown to be a successful design. This control is at present fairly bulky and there is a need for a more compact design. The use of a micro-processor to generate the PWM and square-wave would help reduce the size, and thus be beneficial in the design of the integrated PM universal motor.

  The elimination of the position sensors in the control of the universal motor would also help make the motor more compact. It would also improve the robustness of the design making it more reliable.

- The optimisation of the rotor of PM synchronous motors using the PBIL was very successful. The inclusion of RSM into the PBIL optimiser increased the speed of optimisation drastically. The optimisation of the full motor was not done since a stator of an induction motor was used in this design. The full motor optimisation, including stator slot dimensions, number of armature windings etc; would be useful in reducing the size and mass of the motor.

  Since the RSM successfully modelled the machines characteristics, this method can be used with other optimisation algorithms, such as gradient search optimisation methods.

References

[1] M. Akbaba and S. Q. Fakhro. "An improved computational technique of the inductance parameters of reluctance augmented shaded-pole motors using the finite element method,". *IEEE Transactions on Energy Conversion*, 7(2):308–314, 1992.

[2] P. L. Alger. "The calculation of the armature reactance of synchronous machines,". *AIEE Transactions*, 47(Pt III):493–512, 1928.

[3] C. N. Ashtiani and D. A. Lowther. "Simulation of the steady-state reactances of a large water-wheel generator by finite elements,". *IEEE Transactions on Power Apparatus and Systems*, 103(7):1781–1787, 1984.

[4] K. Atallah, Z. Q. Zhu, and D. Howe. "The prediction of iron losses in brushless permanent magnet dc motors,". *International Conference on Electrical Machines*, 2:814–818, 1992.

[5] J. C. Balda, M. F. Hadingham, R. E. Fairbairn, R. G. Harley, and E. Eitelberg. ""Measurement of Synchronous machine parameters by a modified Frequency Response method - Part I and II",". *IEEE Transactions on Energy Conversion*, 2(4):646–657, 1987.

[6] S. Baluja. "Population-based incremental learning: A method for integrating genetic search based function optimization and competitive learning,". Technical report, Carnegie Mellon University, Pittsburgh (USA), 1994.

[7] S. Baluja. "An empirical comparison of seven iterative and evolutionary function optimization heuristics,". Technical report, Carnegie Mellon University, Pittsburgh (USA), 1995.

[8] S. Baluja and R. Caruana. "Removing the genetics from the standard genetic algorithm,". In A. Prieditis and S. Russel, editors, *The International Conference on Machine Learning*, pages 38–46, California, 1995.

[9] F. Bellina, P. Campostrini, G. Chitarin, A. Stella, and F. Trevisan. "Automated optimal design techniques for inverse electromagnetic problems,". *IEEE Transactions on Magnetics*, 28(2):1549–1552, Mar. 1992.

[10] G. Bertotti. "Physical interpretation of eddy current losses in ferromagnetic materials. i. theoretical considerations,". *Journal of Applied Physics*, 57(6):2110–2117, Mar. 1985.

[11] G. Bertotti. "General properties of power losses in soft ferromagnetic materials,". *IEEE Transactions on Magnetics*, 24(1):621–630, Jan. 1988.

[12] G. Bertotti, A. Boglietti, M. Chiampi, D. Chiarabaglio, F. Fiorillo, and M. Lazzari. "An improved estimation of iron losses in rotating electrical machines,". *IEEE Transactions on Magnetics*, 27(6):5007–5009, Nov. 1991.

[13] N. Bianchi and S. Bolognani. "A procedure for electromagnetic and thermal intergrated design of pm brushless motors,". In *Symposium on Power Electronics, Electrical Drives, Advanced Electrical Motors*, volume 1, pages 13–18, Taormina (Italy), June 1994.

[14] K. J. Binns. "A review of developments in permanent magnet machines and their relation with magnet characteristics,". In *Symposium on Power Electronics, Electrical Drives, Advanced Electrical Motors*, pages 1 – 9, Positano (Italy), May 1992.

[15] A. Boglietti, M. Pastorelli, and F. Profumo. "High speed brushless motors for spindle drives applications,". In *International conference on .. Synchronous Machines*, pages 817–822, Zurich (Switzerland), 1991.

[16] S. R. Bowes and P. R. Clark. "Simple microprocessor implementation of new regular-sampled harmonic elimination pwm techniques,". *IEEE Transactions on Industry Applications*, 28(1):89–95, Jan. 1992.

[17] S. R. Bowes and P. R. Clark. "Transputer-based harmonic-elimination pwm control of inverter drives,". *IEEE Transactions on Industry Applications*, 28(1):72–80, Jan. 1992.

[18] G. E. P. Box and D. W. Behnken. "Some new three level designs for the study of quantitative variables,". *Technometrics*, 2(4):455–475, Nov. 1960.

[19] G. E. P. Box and N. R. Draper. *Evolutionary Operation.* John Wiley and Sons, United States of America, 1969.

[20] G. E. P. Box and N. R. Draper. *Empirical Model-Building and Response Surfaces.* John Wiley and Sons, United States of America, 1987.

[21] M. J. Box, D. Davies, and W. H. Swann. *Non-linear Optimization Techniques.* Oliver and Boyd, Great Britain, 1 edition, 1969.

[22] K. Brandisky, R. Belmans, and U. Pahner. "Optimization of a segmental pm dc motor using fea, statistical experiment design method and evolution strategy,". In *Symposium on Power Electronics, Electrical Drives, Advanced Electrical Motors*, pages 7–12, Taormina (Italy), June 1994.

[23] B. Carnahan, H. A. Luther, and J. O. Wilkes. *Applied Numerical Methods.* John Wiley and sons, U.S.A., 1969.

[24] L. Chang. "Comparison of ac drives for electric vehicles - a report on experts' opinion survey,". *IEEE Aerospace and Electronic Systems Magazine*, 9:7–11, Aug. 1994.

[25] L. Chang, T. R. Eastham, and G. E. Dawson. "Permanent magnet synchronous motor modelling: Finite element and analytical approaches,". In *International Conference on the Evolution and Modern Aspects of Synchronous Machines*, volume 3, pages 1157–1162, 1991.

[26] M. V. K. Chari, Z. J. Csendes, S. H. Minnich, S. C. Tandon, and J. Berkery. "Load characteristics of synchronous generators by the finite element method,". *IEEE Transactions on Power Apparatus and Systems*, 100(1):1–13, 1981.

[27] M. V. K. Chari and P. Silvester. "Analysis of turboalternator magnetic fields by finite elements,". *IEEE Transactions on Power Apparatus and Systems*, 90:454–464, 1971.

[28] J. L. Cohon. *Multiobjective Programming and Planning*, volume 140. Academic Press, New York (USA), 1978.

[29] M. E. Coultes and W. Watson. "Synchronous machine models by standstill frequency response tests,". *IEEE Transactions on Power Apparatus and Systems*, 100(4):1480–1489, 1981.

[30] A. Demenko. "Time-stepping fe analysis of electric motor drives with semiconductor converters,". *IEEE Transactions on Magnetics*, 30(5):3264–3267, Sept. 1994.

[31] A. Demenko. "Movement simulation in finite element analysis of electric machine dynamics,". In *10th Conference on the Computation of Electromagnetic fields*, pages 130–131, Berlin (Germany), July 1995.

[32] N. A. Demerdash and H. B. Hamilton. "A simplified approach to determination of saturated synchronous reactances of large turbogenerators under load,". *IEEE Transactions on Power Apparatus and Systems*, 95(2):560–569, 1976.

[33] N. A. Demerdash, T. M. Hijazi, and A. A. Arkadan. "Computation of winding inductances of permanent magnet brushless dc motors with damper windings by energy perturbation,". *IEEE Transactions on Energy Conversion*, 3(3):705–713, 1988.

[34] R. E. Doherty and C. A. Nickle. "Synchronous machines, part i and ii, an extension of blondel's two-reaction theory,". *AIEE transactions*, 44:403–418, 1925.

[35] J. D. Edwards and E. M. Freeman. *MagNet 5.1 User Guide - Using the MagNet Version 5.1 Package from Infolytica.* Infolytica, London and Montreal, 1995.

[36] M. Enokizono and Y. Akinari. "Estimation of current distribution by a hybrid of genetic algorithm and sampled pattern matching method,". *IEEE Transactions on Magnetics*, 31(3):2012–2015, May 1995.

[37] S. Eriksson. "Drive systems with permanent magnet synchronous motors,". *Automotive Engineering*, pages 75 – 81, Feb. 1995.

[38] R. D. Findlay, N. Stranges, and D. K. MacKay. "Losses due to rotational flux in three phase induction motors,". *IEEE Transactions on Energy Conversion*, 9(3):543–549, Sept. 1994.

[39] F. Fiorillo and A. Novikov. "An improved approach to power losses in magnetic laminations under nonsinusoidal induction waveform,". *IEEE Transactions on Magnetics*, 26(5):2904–2910, Nov. 1990.

[40] R. Fletcher. *Practical Methods of Optimization.* John Wiley and Sons, Great Britain, 2nd edition, 1987.

[41] J. C. Flores, G. W. Buckley, and G. McPherson. "The effects of saturation on the armature leakage reactance of large synchronous machines,". *IEEE Transactions on Power Apparatus and Systems*, 103:593–600, 1984.

[42] R. L. Fox. *Optimization methods for engineering design.* Addison-Wesley publishing company, United States of America, 1971.

[43] E. F. Fuchs and E. A. Erdélyi. "Determination of waterwheel alternator steady-state reactances from flux plots,". *IEEE Transactions on Power Apparatus and Systems*, 91:2510–2527, 1972.

[44] E. F. Fuchs and E. A. Erdélyi. "Nonlinear theory of turboalternators, part i and ii,". *IEEE Transactions on Power Apparatus and Systems*, 92:583–599, 1973.

[45] J. F. Gieras. "Analytical method of calculating the electromagnetic field and power losses in ferromagnetic half-space, taking into account saturation and hysteresis,". *Proceedings of IEE*, 124(11):1098–1104, 1977.

[46] J. F. Gieras. "Performance calculation for small dc motors with segmental permanent magnets,". *Transactions of the SA IEE*, 82(1):14–21, 1991.

[47] A. Gottvald. "Global optimization methods for computational electromagnetics,". *IEEE Transactions on Magnetics*, 28(2):1537–1540, Mar. 1992.

[48] B. Heller and V. Hamata. *Harmonic field effects in induction machines.* Academia Publishing House, Czechoslovakia, 1977.

[49] G. Henneberger, S. Domack, and J. Berndt. "Comparison of the utilization of brushless dc servomotors with different rotor length by 3d - finite element analysis,". *IEEE Transactions on Magnetics*, 30(5):3675–3678, 1994.

[50] J. H. Holland. *Adaption in Natural and Artificial systems.* Bradford Books, United States of America, 3 edition, 1994.

[51] T. M. Jahns. "Motion control with permanent-magnet d.c. machines,". *Proceedings of the IEEE*, 82(8):1241–1252, 1994.

[52] M. K. Jamil and N. A. Demerdash. "Harmonic and core losses of permanent magnet dc motors controlloed by chopper circuits,". *IEEE Transactions on Energy Conversion*, 5(2):408–414, June 1990.

[53] M. Jufer. "Electric drives - towards the integration,". In *International conference on .. Synchronous Machines*, pages 1135–1143, Zurich (Switzerland), 1991.

[54] T. Kailath, editor. *Linear Least-squares Estimation.* Dowden, Hutchinson and Ross, Inc, Pennsylvania (U.S.A.), 1977.

[55] M. Kasper. "Shape optimization by evolution strategy,". *IEEE Transactions on Magnetics*, 28(2):1556–1560, Mar. 1992.

[56] L. A. Kilgore. "Calculation of synchronous machine constants - reactances and time constant affecting transient,". *AIEE Transactions*, 50(III):1201–1213, 1931.

[57] E. I. King. "Equivalent circuits for two-dimensional magnetic fields: I - the static field,". *IEEE Transactions on Power Apparatus and Systems*, 85(9), 1966.

[58] M. Kostenko and L. Piotrovsky. *Electrical Machines*, volume 2. Mir Publishers, Moscow, 1974.

[59] G. Kron. *The Application of Tensors to the Analysis of Rotating Electrical Machinery.* General Electric Review, New York, 1942.

[60] K. Kurihara, G. Wakui, and T. Kubota. "Steady-state performance analysis of permanent magnet synchronous motors including space harmonics,". *IEEE Transactions on Magnetics*, 30(3):1306–1315, May 1994.

[61] J. D. Lavers and P. P. Biringer. "Prediction of core losses for high flux densities and distorted flux waveforms,". *IEEE Transactions on Magnetics*, 12(6):1053–1055, Nov. 1976.

[62] T. Li and G. Slemon. "Reduction of cogging torque in permanent magnet motors,". *IEEE Transactions on Magnetics*, 24(6):2901–2903, Nov. 1988.

[63] T. A. Lipo. "Synchronous reluctance machines - a viable alternative,". In *International conference on .. Synchronous Machines SM100*, number 2 in 1, pages 475–479, Zurich (Switzerland), 1991.

[64] X. Liu and G. R. Slemon. "An improved method of optimization for electrical machines,". *IEEE Transactions on Energy Conversion*, 6(3):492–496, Sept. 1991.

[65] M. Liwschitz-Garik and C. C. Whipple. *Electric Machinery.* D van Nostrand company Inc, United States of America, 3 edition, 1947.

[66] T. S. Low and B. Chao. "The use of finite elements and neural networks for the solution of inverse electromagnetic problems,". *IEEE Transactions on Magnetics*, 28(5):2811–2813, Sept. 1992.

[67] D. C. Macdonald, A. B. J. Reece, and P. J. Turner. "Turbine-generator steady-state reactances,". *Proceedings of IEE Part C*, 132(3):101–108, 1985.

[68] I. D. Mayergoyz. "Mathematical models of hysteresis,". *IEEE Transactions on Magnetics*, 22(5):603–608, Sept. 1986.

[69] B. Mellara and E. Santini. "F.e.m. computation and optimization of l_d and l_q in disc pm machines,". In *International Workshop on Electric and Magnetic Fields*, number 89 in 1, Leuven, 1994.

[70] P. H. Mellor, F. B. Chaaban, and K. J. Binns. "Estimation of parameters and performance of rare-earth permanent-magnet motors avoiding measurement of load angle,". *Proceedings of IEE Part B*, 138(6):322–330, 1991.

[71] L. M. C. Mhango. "Advantages of brushless dc motors, high-speed aerospace drives,". In *International conference on .. Synchronous Machines*, pages 829–833, Zurich (Switzerland), 1991.

[72] I. Miller and J. E. Freund. *Probabilty and Statistics for Engineers.* Prentice-Hall inc, New Jersey (USA), 3rd edition, 1977.

[73] T. J. E. Miller. "Methods for testing permanent magnet polyphase ac motors,". In *IEEE Industrial Applications and Systems Society Meeting*, pages 494–499, New York, 1981.

[74] T. J. E. Miller. *Brushless Permanent-Magnet and Reluctance Motor Drives.* Oxford Science Publications, New York, 1 edition, 1989.

[75] T. J. E. Miller and R. Rabinovici. "Back-emf waveforms and core losses in brushless dc motors,". *IEE Proceedings B - Electrical Power Applications*, 141(3):144–154, May 1994.

[76] O. A. Mohammed, D. C. Park, F. G. Uler, and C. Ziqiang. "Design optimization of electromagnetic devices using artifical neural networks,". *IEEE Transactions on Magnetics*, 28(5):2805–2807, Sept. 1992.

[77] N. Mohan, T. M. Undeland, and W. P. Robbins. *Power Electronics: Converters, Applications and Design.* John Wiley and Sons, Singapore, 1989.

[78] D. C. Montgomery. *Design and Analysis of Experiments.* John Wiley and Sons, United States of America, 2nd edition, 1984.

[79] S. R. Naidu. "Simulation of the hysteresis phemenon using preisach's theory,". *IEE Proceedings A*, 137(2):73–79, Mar. 1990.

[80] S. A. Nasar, I. Boldea, and L. E. Unnewehr. *Permanent magnet, reluctance, and self-synchronous motors.* CRC Press, Boca Raton-Ann (Arbor), 1st ed edition, 1993.

[81] T. W. Nehl, F. A. Fouad, and N. A. Demerdash. "Determination of saturated values of rotating machinery incremental and apparent inductances by energy perturbation method,". *IEEE Transactions on Power Apparatus and Systems*, 101(12):4441–4451, 1982.

[82] R. A. Newbury. "Prediction of loss in silicon steel from distorted waveforms,". *IEEE Transactions on Magnetics*, 14(4):263–268, July 1978.

[83] H. M. Norman. "Induction motor locked saturation curves,". *Electrical Engineering*, pages 536–541, 1934.

[84] D. O'Kelly and S. Simmons. *Generalised Electrical Machine Theory.* McGraw-Hill, London, 1968.

[85] I. L. Osin, V. P. Kolesnikov, and F. M. Yuferov. *Permanent magnet synchronous micromotors (in Russian).* Energia, Moscow, 1976.

[86] B. Palit, K. Reichert, and T. Taerhuvud. "From asynchronous to synchronous reluctance motors,". In *International conference on .. Synchronous Machines SM100*, number 2 in 1, pages 480–487, Zurich (Switzerland), 1991.

[87] R. J. Parker. *Advances in permanent magnetism.* J. Wiley and Sons, 1990.

[88] D. Pavlik, V. K. Garg, J. R. Repp, and J. Weiss. "A finite element technique for calculating the magnet sizes and inductances of permanent magnet machines,". *IEEE Transactions on Energy Conversion*, 3(1):116–122, 1988.

[89] R. H. Pry and C. P. Bean. "Calculation of the energy loss in magnetic sheet materials using a domain model,". *Journal of Applied Physics*, 29(3):532–533, Mar. 1958.

[90] R. Rabinovici. "Eddy current losses of permanent magnet motors,". *IEE Proceedings B - Electrical Power Applications*, 141(1):7–11, Jan. 1994.

[91] M. A. Rahman and A. M. Osheiba. "Performance of large line-start permanent magnet synchronous motors,". *IEEE Transactions on Energy Conversion*, 5(1):211–217, 1990.

[92] M. A. Rahman and P. Zhou. "Determination of saturation parameters of pm motors using loading magnetic fields,". *IEEE Transactions on Magnetics*, 27(5):3947–3950, 1991.

[93] M. A. Rahman and P. Zhou. "Field-based analysis for permanent magnet motors,". *IEEE Transactions on Magnetics*, 30(5):3664–3667, 1994.

[94] S. Ratnajeevan, H. Hoole, and M. K. Haldar. "Optimization of electromagnetic devices: Circuit models, neural networks and gradient methods in concert,". *IEEE Transactions on Magnetics*, 31(3):2016–2019, May 1995.

[95] T. Renyuan, L. Ge, and S. Changzhi. "The application of the finite element method to the design of repm synchronous generators,". *IEEE Transactions on Magnetics*, 21(6):2472–2475, 1985.

[96] T. Renyuan and Y. Shiyou. "Combined strategy of improved simulated annealing and genetic algorithm for inverse problem,". In *10th Conference on the Computation of Electromagnetic fields*, pages 196–197, Berlin (Germany), July 1995.

[97] H. C. Roters. *Electromagnetic Devices.* John Wiley and Sons, Inc., New York, 1941.

[98] S. Russenschuck. "Mathematical optimization techniques for the design of permanent magnet synchronous machines based on numerical field calculation,". *IEEE Transactions on Magnetics*, 26(2):638–641, Mar. 1990.

[99] S. Russenschuck and E. C. Andresen. "The influence of rotor design and inverter type on the magnet volume of synchronous machines investigated by numerical field calculation and vector-optimization methods,". *Archiv für Electrotechnik*, 75:61–69, 1991.

[100] E. Santini. "F.e.m. analysis of innovative permanent magnets in synchronous machines,". In *International Conference on the Evolution and Modern Aspects of Synchronous Machines*, volume 3, pages 1175–1180, 1991.

[101] M. G. Say. *The Performance and Design of Alternating Current Machines.* Sir Isaac Pitman and Sons, Ltd, London (Great Britain), 1949.

[102] R. Schiferl and T. A. Lipo. "Core losses in buried magnet permanent magnet synchronous motors,". *IEEE Transactions on Energy Conversion*, 4(2):279–284, June 1989.

[103] R. F. Schiferl, R. S. Colby, and D. W. Novotny. "Efficiency considerations in permanent magnet synchronous motor drives,". In *Electric Energy Conference*, pages 286–291, Adelaide (Australia), 1987.

[104] T. Sebastian. "Temperature effects on torque production and efficiency of pm motors using ndfeb magnets,". *IEEE Transactions on Industry Applications*, 31(2):353–357, Mar. 1995.

[105] P. P. Silvester and M. V. Chari. "Finite element solution of saturable magnetic field problems,". *IEEE Transactions on Power Apparatus and Systems*, 89(7):1642–1651, 1970.

[106] P. P. Silvester and R. L. Ferrari. *Finite Elements for Electrical Engineers.* Cambridge University Press, Cambridge (U.K.), 1983.

[107] J. Simkin and C. W. Trowbridge. "Optimizing electromagnetic devices combining direct search methods with simulated annealing,". *IEEE Transactions on Magnetics*, 28(2):1545–1548, Mar. 1992.

[108] G. R. Slemon and L. Xian. "Core losses in permanent magnet motors,". *IEEE Transactions on Magnetics*, 26(5):1653–1655, Sept. 1990.

[109] W. L. Soong and T. J. E. Miller. "Theoretical limitations to the field-weakening performance of the five classes of brushless synchronous ac motor drive,". In *Sixth International conference on Electrical Machines and Drives*, volume 1, pages 127 – 132, Oxford (England), 1993.

[110] W. Szeląg. "Numerical method for determining parameters of permanent magnet synchronous motor,". In *XII Symposium on Electromagnetic Phenomena in Nonlinear Circuits*, volume 1, pages 331–335, Poznań (Poland), 1991.

[111] I. Tsukerman. "Accurate computation of ripple solutions on moving finite element meshes,". *IEEE Transactions on Magnetics*, 31(3):1472–1475, May 1995.

[112] P. J. Turner, A. B. J. Reece, and D. C. Macdonald. "The d.c. decay test for determining synchronous machine parameters: measurement and sinulation,". *IEEE Transactions on Energy Conversion*, 4(4):616–623, 1989.

[113] G. F. Uler, O. A. Mohammed, D. C. Park, and C.-S. Koh. "Design optimization of electrical machines using genetic algorithms,". *IEEE Transactions on Magnetics*, 31(3):2008–2011, May 1995.

[114] J. Wang, N. Bennett, K. J. Binns, and D. W. Shimmin. "Computational and experimental determination of static and dymanic parameters for modelling permanent magnet synchronous machines,". In *Sixth International conference on Electrical Machines and Drives*, volume 1, pages 289–294, Oxford (England), 1993.

[115] R. Yokoyama and K. Ito. "Multi-objective optimization in unit sizing of a gas turbine cogeneration plant,". *Journal of Engineering for Gas Turbines and Power*, 117:53–59, Jan. 1995.

[116] J. G. Zhu, S. Y. R. Hui, and V. S. Ramsden. "Discrete modelling of magnetic cores including hysteresis eddy current and anomalous losses,". *IEE Proceedings A*, 140(4):317–322, July 1993.

[117] J. G. Zhu, V. S. Ramsden, and P. A. Watterson. "Finite element calculation of core losses in motors with non-sinusoidal fields,". *ICEM92*, 3:1182–1186, 1992.

Appendix A

Losses under non-sinusoidal fields

The heat produce within a machine can have a drastic effect on the performance of the motor. The heating also effects the operating point of the magnets on the rotor. Since NdFeB magnets are substantially cheaper than SmCo magnets it is inevitable that most motor designs will use the cheaper NdFeB magnets. NdFeB magnets have a much higher temperature coefficient than SmCo magnets and thus the machine losses become that much more important to the motors performance, due to the reduction of the residual flux density and intrinsic coercivity as the temperature increases [104]. The possibility of irreversible demagnetization of NdFeB magnets at higher temperatures should also be considered in the design.

The losses within the motor are classified as:

(a) *Armature winding losses* are the main source of losses, I^2R_1.

(b) *Core losses* are the second largest component of power loss in brushless PM motors, and depend drastically on the machine design and input current wave forms. Core losses P_t are due to the changing magnetic fields within the motor core, which cause hysteresis P_h and eddy current P_e losses. The components that make up the core losses are the stator iron losses and rotor iron losses.

(c) *Surface losses* are due to the deformed distribution of the magnetic field intensity caused by the stator slots. Eddy currents arise in the rotor surface due to this field intensity cause additional losses. Similar losses will accure on the surface of the stator teeth.

(d) *Pulsation losses* are due to the periodic changing magnetic flux density in the stator slots from the rotating magnetic field on the rotor. The mutual position between the individual stator slots and rotor cause this magnetic induction. A similar effect is caused on the rotor. Pulsation losses will be considered part of the total core losses in the further analysis.

(e) *Rotational losses* due to friction in the bearings, windage and ventilation. These losses are proportional to the rotational speed.

The armature winding, surface and rotational losses are described and discussed in many publications and texts [48]. The armature winding and rotational losses are calculated as for an inverter fed induction motor. The surface losses are extremely difficult to assess and are considered negligible due to the airgap being larger than that of an equivalent induction machine. The core losses are dependent on the input current wave form and the shape of the airgap flux produced by the PM field. The core losses are thus directly influenced by the machine design and can be reduced at the geometry design stage of the motor. The core losses in the stator and rotor are considered separately below including the pulsating losses due to the rotational effects of the rotor.

A.1 Stator Core Losses

The *stator iron losses* are due to the alternating currents which circulate through it as well as the changing magnetic flux due to the rotor field. The stator is laminated to reduce these losses. According to Steinmetz the losses for sinusoidal excitation can be calculated from $P_h = k_h f B_m^{\alpha}$ and $P_e = k_e f^2 B_m^2$ where k_h, α and k_e are constants depending on the characteristics of the material from the standard Epstein test, f is the frequency, and B_m is the peak flux density.

Brushless PM machines produce a non-sinusoidal airgap flux, unlike induction motors and salient pole slip-ring synchronous motors. The harmonic content of the flux in the stator, due to the magnetised rotor structure due to this non-sinusoidal flux, is thus larger. Brushless PM machines are also fed from switched DC sources with pulse-width modulation or square wave control. The applied voltage thus contains many harmonics with are seen in the stator flux. Many authors have shown the poor correlation between measured core losses and those calculated using classical methods. Bertotti [12] notes errors between 25 % and 75 %.

Over the past 6 years two distinct methods have been developed for calculating the stator core losses in PM motors. The one method uses the individual harmonics of the flux density in its calculation, and the other models the waveform of the magnetic flux density and uses modified Steinmetz equations.

A.1.1 Harmonic Method

The total stator core loss is calculated from the sum of the individual harmonic core losses [61, 82]. The magnetic flux density waveforms are obtained in different sectors of the motor core using either frequency domain [38, 52, 102] or time domain methods [4, 12, 117]. Rotational losses have been included in the time domain method [12].

The stator core loss under a non-sinusoidal flux density waveform can be defined as [39, 117]:

$$P_t = P_h + P_e = \frac{1}{T}\int_0^T [P_h(t) + P_e(t)]dt \tag{A.1}$$

where the periodic flux density is written as a Fourier expansion:

$$B(t) = \sum_{n=0}^{\infty} B_n sin(2\pi nft + \theta_n) \qquad (n = odd;\ \theta_n = 0) \tag{A.2}$$

The hysteresis losses are caused by localised irreversible changes during the magnetisation process. The hysteresis, including a empirical correction factor for minor hysteresis loops, is given as [61]:

$$P_h = k_h f B_m^{\alpha} K(B_m) \tag{A.3}$$

where the minor loop correction factor is:

$$K(B_m) = 1 + \frac{0.65}{B_m}\sum_{i=1}^{\infty}\Delta B_i \tag{A.4}$$

and where ΔB_i is the change in the flux density during the minor loop.

The eddy current or dymanic loss is expressed as [10, 11, 39, 89]:

$$P_e = P_c + P_a \tag{A.5}$$

where P_c is the classical eddy current loss and P_a is the anomalous loss generally considered caused by the motion of the domain walls. The classical eddy current loss is calculated on the assumption of a homogeneous flux density distribution over the thickness of the lamination as [39]:

$$P_c = \frac{\sigma\pi^2 f^2 d^2}{6\delta}\sum_{n=0}^{\infty} n^2 B_n^2 \qquad (n = odd) \tag{A.6}$$

where σ is the electrical conductivity, d is the lamination thickness and δ is the material mass density.

The anomalous losses are shown according to statistical theory is [39]:

$$P_a = \sqrt{\sigma G C_o S}\frac{1}{T}\int_0^T |\sum_{n=0}^{\infty} 2\pi nfB_n \times \cos(2\pi nft + \theta_n)|^{3/2}dt \tag{A.7}$$

where G is a dimensionless coefficient, C_o characterises the statistical distribution of the local coercive fields depending on the grain of the material and S is the lamination cross-sectional area. The anomalous losses are usually obtained from experimental data. It has been shown in [11] that laminated silicon steel (3% N.O. 0.5 mm), and materials in the same class and thickness show approximately equal values of P_c and P_a at 50 Hz, so due to the complexity

of eqn (A.7) this assumption is used.

A.1.2 Waveform Method

This method models the waveform of the magnetic flux to obtain the losses. This method uses a modified Steinmetz equation based on a change of flux density (dB/dt) instead of the frequency to accommodate non-sinusoidal flux waveforms [108]. This method assumes that the eddy current losses in permanent magnet motors are proportional to the square of the time change rate of the magnetic flux. The flux densities are obtained from classical theory and to simplify the model the stator is divided up into the stator yoke and stator teeth regions.

The use of the back EMF per tooth waveform has also recently been used in place of the magnetic flux distribution in calculating the core losses [90, 75].

The total stator core loss is given for example in [108]:

$$P_t = k_h f B_m^{\alpha} + \frac{k_e}{2\pi^2}\left(\frac{dB}{dt}\right)^2 \tag{A.8}$$

where dB/dt is the RMS value over one cycle. The flux density waveform for the stator teeth (B_t) and stator yoke (B_y), in terms of the EMF, are [75]:

$$\frac{dB_t}{dt} = -\frac{e_t(\xi)}{A_t} \qquad \frac{dB_y}{dt} = -\frac{e_y(\xi)}{A_y} \tag{A.9}$$

where e_t and e_y are the teeth and yoke EMF waveforms respectively, A_t and A_y are the cross-section areas of the tooth and yoke respectively and ξ is the rotor position.

The hysteresis losses in eqn (A.8) assumes that hysteresis is only dependent on the maximum flux density and the effect of minor hysteresis loops is ignored.

A.2 Rotor Iron Losses

The *rotor iron losses* are due to the pulsating flux produced by the rapid changes in airgap reluctance as the rotor passes the stator teeth. These losses are negligible in surface mounted PM motors, due to there large effective airgaps. In buried PM motors and surface PM motors with mild steel pole shoes these rotor losses should be considered.

The rotor losses have a higher frequency than the fundamental frequency and are flux density fluctuations on the constant flux density. The losses can thus be obtained using the *harmonic method* described above. The eddy current losses can be calculated using eqn (A.6), using the same assumptions. The hysteresis losses are due to the minor hysteresis loops which are more complicated to calculate that eqn (A.3). Preisach's theory has recently been used to calculate minor loop losses [68, 79, 116]. Since this method requires detailed information about the material being analysed, the hysteresis losses in the rotor will be neglected. The

hysteresis losses become negligible as the airgap increases and the airgap will be considered to be large enough to neglect these losses.

A.3 Core Loss Finite Element Model

The core losses within the stator and rotor are calculated using a set of finite element models, assuming constant rotor speed and balanced three-phase armature currents. The dynamic losses, within the cores, in the two-dimensional distorted flux waveforms, from eqn (A.6) is:

$$P_c = \frac{\sigma \pi^2 f^2 d^2}{6\delta} \sum_{n=0}^{\infty} n^2 [B_{nx}^2 + B_{ny}^2] \qquad (n = odd) \tag{A.10}$$

The field distribution at several time intervals in the fundamental current cycle is needed to create the magnetic flux density waveforms. This is obtained by rotation of the rotor grid and phase advancement of the stator currents. From a field solution, for a particular rotor position, the magnetic flux density at each element centroid is calculated. The flux density values can be used to obtain three flux density components in an element from a single FEM solution.

Appendix B

Manufacturing costs of PM Universal Motor

The cost of building a prototype 2.2 kW PM universal motor is compared against buying a 2.2 kW induction motor and variable speed drive. Table B.1 shows a detailed listing of the cost of producing one PM universal motor and Table B.2 shows the cost of purchasing a variable speed induction motor drive.

Table B.1: Cost of universal motor drive

ITEM	**Cost**	
Materials	**SA Rands**	**US $**
70% of the price of 1.5 kW 4-pole induction motor GEC motor using frame D90L	487	135.28
Solid mild steel and brass for rotor	168	46.67
4 × NdFeB magnets (N27SH) from Better Elect Company @ R 75.00	300	83.33
3 × IGBT switches (Toshiba MG25Q2YS91) @ R 151.00 each	453	125.83
3 × Semikon drives (SKHI 21) @ R 255.00 each	765	212.50
Motorola MC33035 and MC33039 ICs	18	5.00
Other electronic components and cables	85	23.61
Printed circuit board	340	94.44
Box for power electronics	150	41.67
Labour		
Machining of rotor	300	83.33
Labour for assembling electronics	400	111.11
TOTAL COST OF COMPLETE UNIVERSAL DRIVE	**3466**	**962.78**

Table B.2: Cost of Induction motor drive

ITEM	Cost	
Materials	**SA Rands**	**US $**
2.2 kW 4-pole induction motor from GEC, frame DX100L	834	231.67
Siemens Micro-master drive for 2.2 kW induction motor	4487	1246.39
TOTAL COST OF COMPLETE INDUCTION DRIVE	**5321**	**1478.06**

It should be noted that the price of the universal motor does not include any mark up on the product. It also does not take into account that most of the prices listed in Table B.1 will be reduced if large quantites were purchased. Any production model would also replace the Semikron drives with less expensive voltage isolation units, saving approximately R 700.00 off the total price.

The cost of the two systems should be seen as being similarly priced since the capital investment needed to start a new company has not been factored into the price of the universal motor.

Appendix C

Selected Electronic Schematics

C.1 Sinewave PWM generator

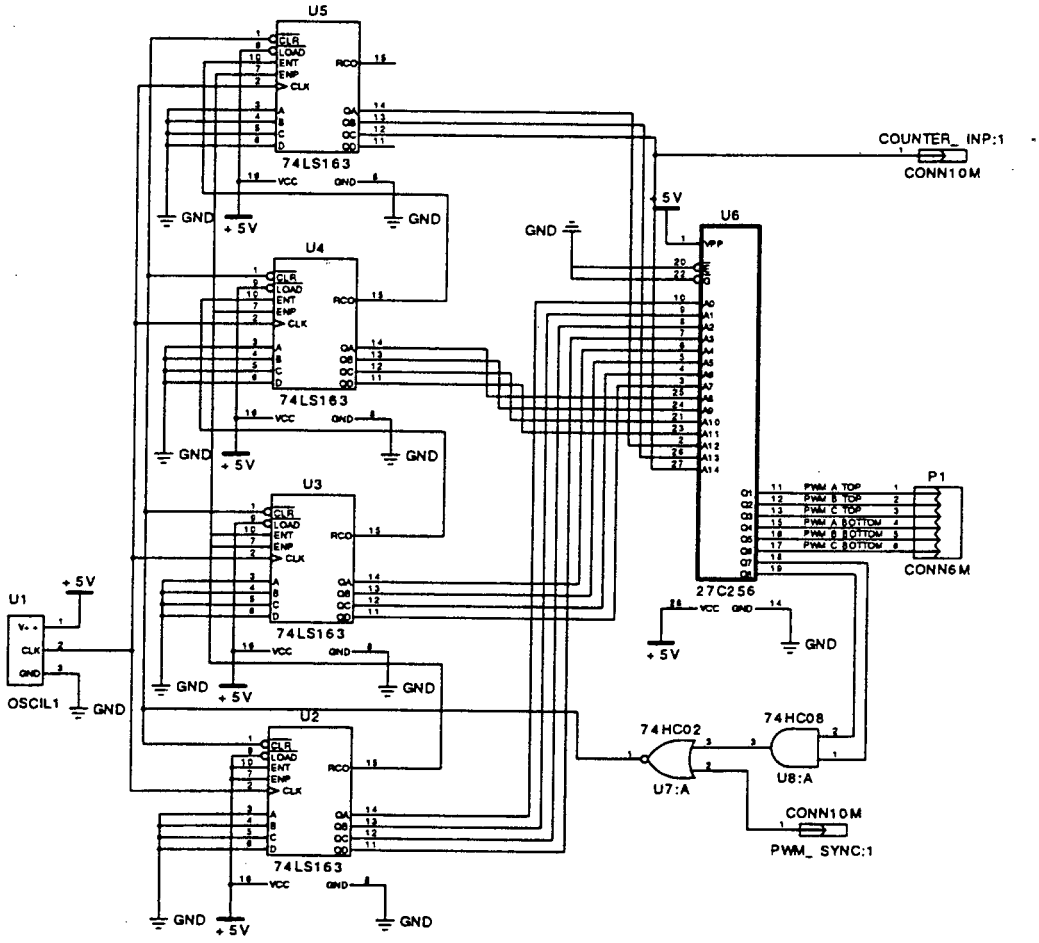

Figure C.1: The PWM generation uses an EPROM and binary counters. Six data bits in the EPROM are programmed to represent the switching sequences of each of the six IGBT switches.

C.2 Mode Switching Control

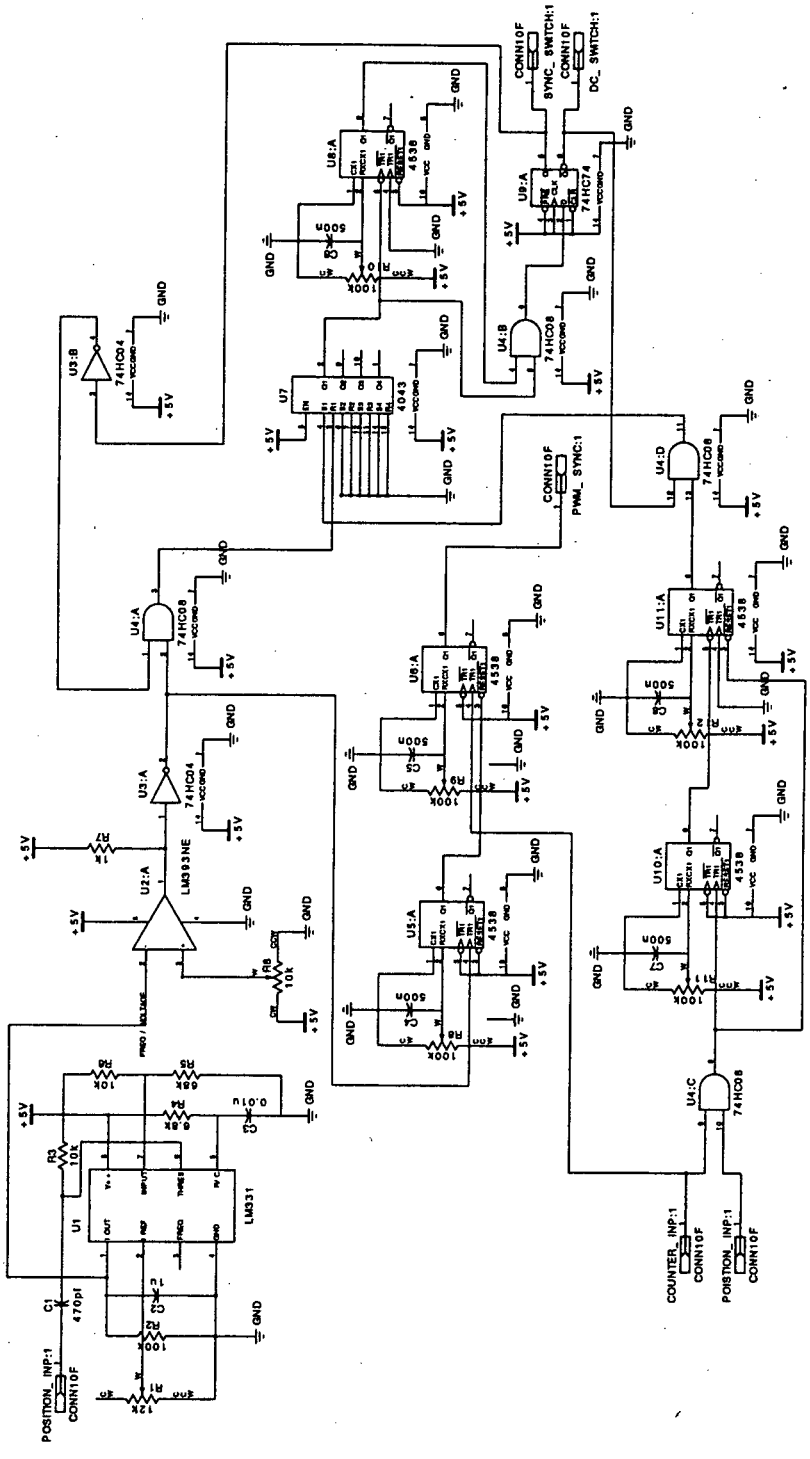

Figure C.2: The mode switching control monitors the rotor speed and load angle, and determines the appropriate operating mode. The load angle is monitored during synchronous operation, while the speed is monitored during DC operation

C.3 Mode Switching Logic

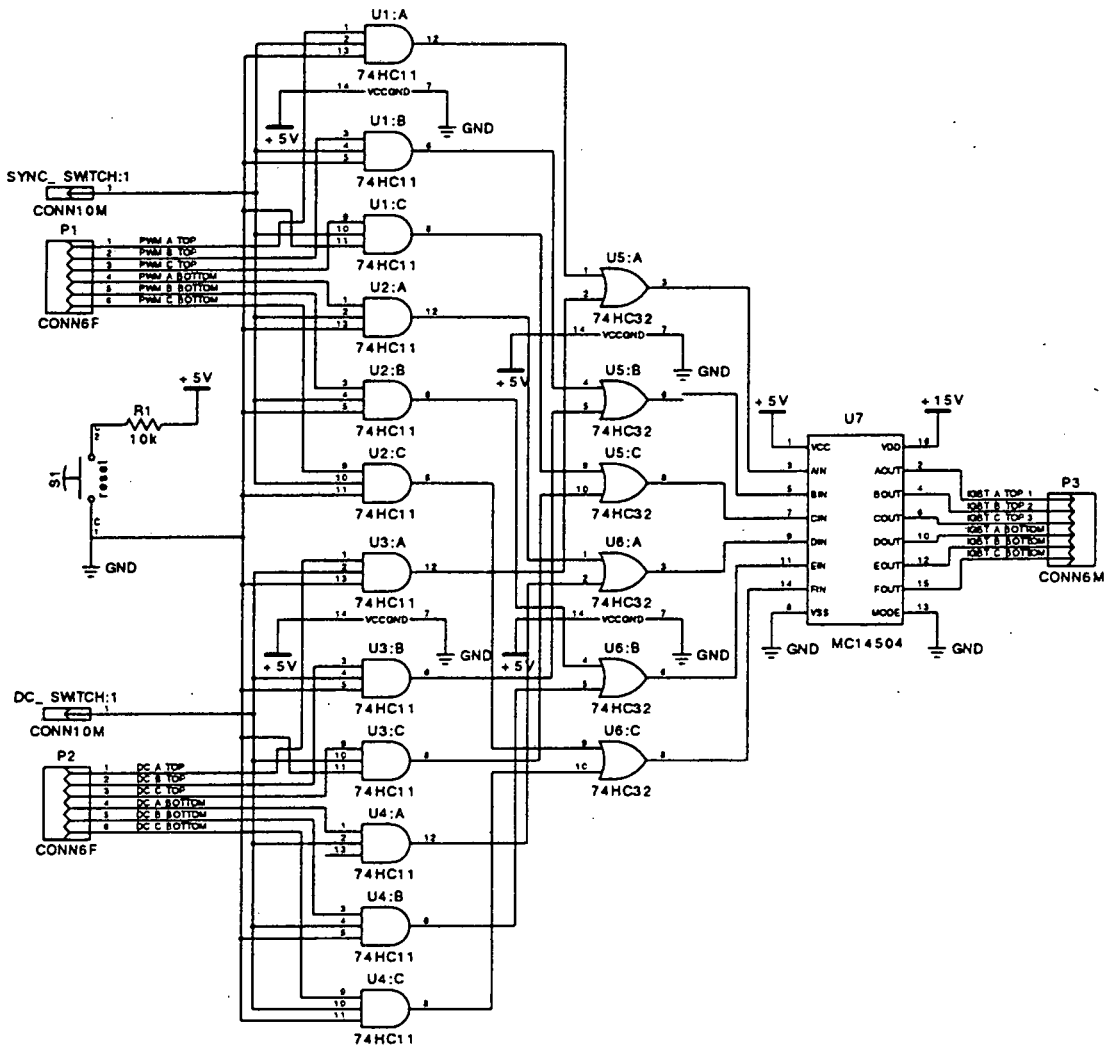

Figure C.3: The mode switching logic is used for resetting the Semikron drives and for switching the drive signals from synchronous to DC, and visa versa. The mode switching signals come from the mode switching control circuit.